A CHAPMAN-ENSKOG-LIKE (CEL) CONTINUUM KINETIC CLOSURE APPROACH IN NIMROD

by

Joseph R. Jepson

A dissertation submitted in partial fulfillment of
the requirements for the degree of

Doctor of Philosophy

(Physics)

at the

UNIVERSITY OF WISCONSIN–MADISON

2024

Date of final oral examination: 03/25/24

The dissertation is approved by the following members of the Final Oral Committee:

Chris C. Hegna, Professor, Nuclear Engineering and Engineering Physics
Carl R. Sovinec, Professor, Nuclear Engineering and Engineering Physics
Paul W. Terry, Professor, Physics
John S. Sarff, Professor, Physics

Dedicated to my wife who has supported and encouraged me in finishing this work.

ACKNOWLEDGMENTS

There are many people who have helped me arrive at this point. Both my undergraduate and graduate advisors, Eric Held and Chris Hegna, have provided innumerous hours of help, advice, and direction throughout this process. I would not be here without their patient and consistent help. I also want to acknowledge Carl Sovinec, who has provided significant help and direction at crucial points in my research. Of course credit is due to many of the good professors I have had in various classes, both for explaining concepts clearly and thoroughly, as well as for being willing to challenge me to achieve higher than I would have otherwise.

Gratitude is also due to many others have positively contributed along my journey. My first office mate here, Jeff Kollasch, was kind and helpful and showed me the ropes when I first arrived at UW-Madison. Hung Tran, a professor in MATH 819, was very kind and provided me significant help to pass his class at a difficult time. I also acknowledge gratefully many positive and fruitful discussions with members of the NIMROD team, which discussions have aided in accomplishing the research aims herein.

I especially want to thank my wife for her support, encouragement, and prayers as I have worked to arrive at this point. And finally, I thank God for all the inspiration and strength He has given me during my time here.

CONTENTS

ABSTRACT

Herein, a numerical method for solving a Chapman-Enskog-like (CEL) continuum kinetic model for plasmas is formulated, analyzed, and applied in the plasma fluid code NIMROD. The CEL approach is a δf drift kinetic approach that allows rigorous closure of the plasma fluid equations in all collisionality regimes. Importantly, in this approach, the zeroth order in δ_i ($\delta_i \equiv \rho_i/L$, with ρ_i the ion gyroradius and L a macroscopic length scale) distribution function is a time-evolving Maxwellian. This difference leads to an $O(\delta_i)$ kinetic equation that analytically enforces that the first order kinetic distortion f_1 have no number density (n), flow ($\mathbf{u}$), and temperature (T) moments. The fluid variables in this method are allowed to deviate far from an initial equilibrium. The fluid equations are closed by incorporating appropriate velocity space moments of the first order kinetic distortion.

An axisymmetric poloidal flow damping calculation is performed to benchmark the implementation. It is first shown that the kinetic aspects of the implementation give results for the steady-state poloidal flow that agree both with other codes, analytics, and a fixed-background (i.e. f_0 a stationary Maxwellian) δf implementation in NIMROD. It is then shown that the flow dynamics in the full CEL approach agree well both with analytics and with results from the fixed-background δf implementation.

A von Neumann linear stability analysis of the full fluid-kinetic system is also performed to help elucidate methods to make the time advance of the full system numerically stable. It is shown that numerical stability is impossible to achieve without explicitly enforcing key tenets of the CEL closure approach, in particular, that the n, $\mathbf{u}$, and T moments of the kinetic distortion remain small in time. In addition, it is shown that centering the heat flux at the beginning of the time step and the ion temperature at the end of the time step in the kinetic equation allows for a numerically-stable time advance of the coupled fluid-kinetic system. Furthermore, these linear stability results are seen to remain applicable when running NIMROD fully nonlinearly.

The methodology for applying the CEL approach to general non-axisymmetric problems of interest is also discussed. Future work will include applying this closure approach to the problem of forced magnetic reconnection in toroidal geometry, as well as to accurate simulation of neoclassical tearing modes (NTMs) in tokamaks.

1 INTRODUCTION

1.1 Fusion as an alternative energy source

The energy needs of the human race are substantial. In the last 57, years the energy consumption of the world has more than tripled, currently sitting at a whopping 604.04 EJ (see Fig. 1.1). Most of the world's rising energy needs have been supplied in the form of fossil fuels, with fossil fuels currently accounting for ~ 82% of the world's energy consumption. Renewables are making up an increasing fraction of the world's energy market though, accounting for ~ 7% of the energy consumption as of 2022 (see Fig. 1.2). Most of the recent increases in renewables are due to wind and solar, with solar undergoing significant gains in power capacity in recent years (see Figs. 1.3-1.4). Wind and solar energy will likely make up an increasingly significant portion of the world's energy budget in the next few decades. These energy sources, however, suffer from a few notable downsides, including

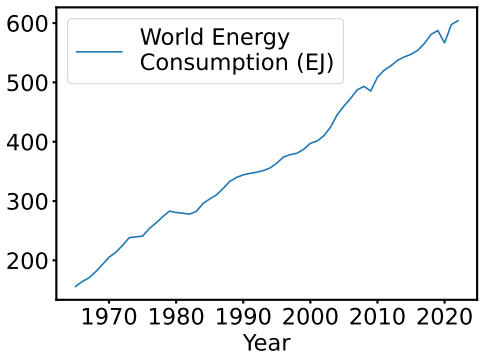

Figure 1.1: Total world energy consumption vs. year [1].

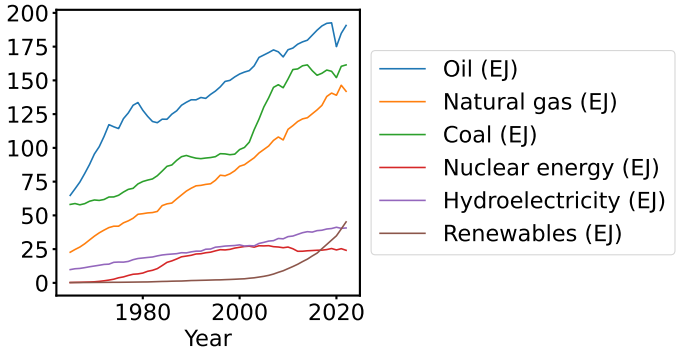

Figure 1.2: World yearly energy breakdown by type [1].

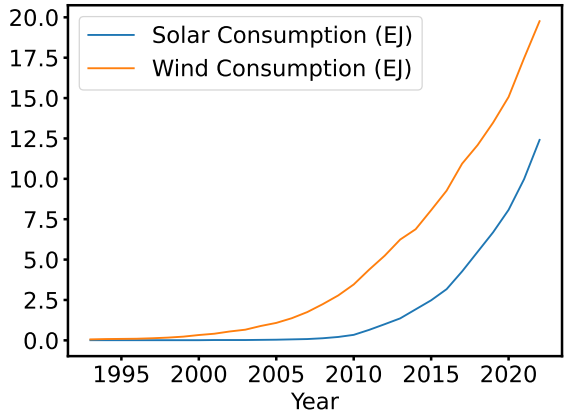

Figure 1.3: Solar and wind energy consumption vs. year [1].

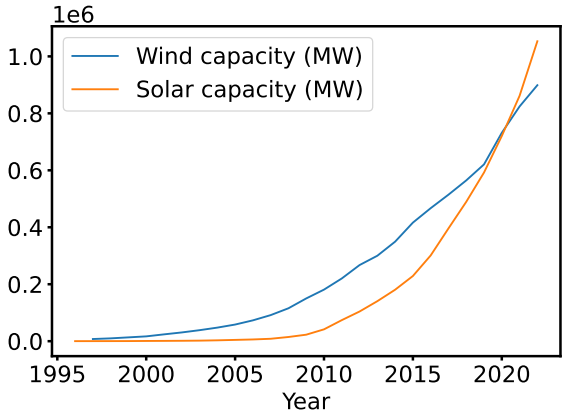

Figure 1.4: Solar and wind power capacity vs. year [1].

the need of large energy storage systems, intermittency, and being distributed over a relatively large land area.

Nuclear fusion, as a possible alternative energy source, would provide a clean, continuous, and compact source of energy for the energy needs of the world, with fuel sources that are readily abundant. Nuclear fusion is the process by which lighter elements combine to form heavier elements, releasing large quantities of energy. Most envisioned nuclear fusion reactors utilize the following reaction involving the fusion of Deuterium (^{2}H) with Tritium (^{3}H):

$$^2\mathrm{H} + {}^3\mathrm{H} \longrightarrow {}^4\mathrm{He} + \mathrm{n} + 17.6\ \mathrm{MeV}\ , \tag{1.1}$$

where a neutron (n) is produced, as well as 17.6 MeV of energy (with 80% of this energy in the neutron). Tritium is not naturally occurring at the levels needed for widespread use in nuclear fusion, but can be produced in a reactor setting from enriched Lithium. Although the efficient and environmentally friendly production of enriched Lithium is still an active area of research, the Deuterium-Tritium reaction is often chosen because it produces a significant quantity of energy at lower temperatures than certain other fusion reactions (e.g. a Deuterium-Deuterium reaction) [2].

High temperatures (of the order of 10 keV, or 10 times hotter than the core of the sun) are required in nuclear fusion reactions to overcome the Coulomb repulsive barrier between the positively charged nuclei in the fuel. At these high temperatures, electrons and the positively charged nuclei separate from each other forming a plasma, or a quasi-neutral gas of charged particles dominated by collective behavior. Because fusion plasmas are significantly hotter than the melting point of any known material [3], a method to keep the hot plasma away from material surfaces is required.

1.2 Magnetic confinement fusion (MCF)

A hot plasma experiences a large pressure gradient force (∇p) tending to expand the plasma outwards. In magnetic confinement fusion (MCF), a confining force is provided by a strong magnetic field everywhere in the plasma. The magnetic field confines the plasma by means of the $\mathbf{J} \times \mathbf{B}$ force, with $\mathbf{J}$ the current density in the plasma, and $\mathbf{B}$ the magnetic field in the plasma. This equilibrium condition is written as

$$\mathbf{J} \times \mathbf{B} = \nabla p\ . \tag{1.2}$$

It turns out that the only smooth closed surface which allows for an everywhere non-zero and continuous magnetic field is a torus [4] (see also Ch. 3 of Ref. [5]). Confinement of the hot plasma

in MCF therefore requires a toroidal configuration. This is achieved by confining the plasma on an uncountably infinite set of nested toroidal magnetic surfaces (i.e., a surface with the magnetic field on the surface everywhere parallel to the surface). The innermost magnetic surface, which is just a circular line, is termed the magnetic axis. See Fig. 1.5 for an example toroidal equilibrium, with a few representative magnetic surfaces shown.

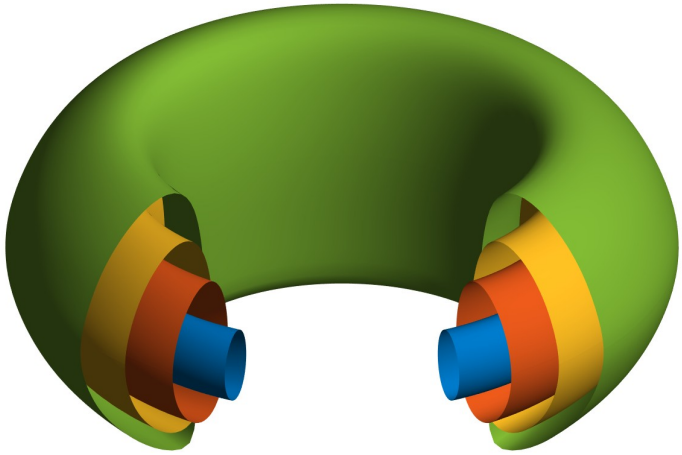

Figure 1.5: An example toroidal equilibrium, with a few representative magnetic surfaces shown.

1.2.1 Particle dynamics in strong magnetic fields

The motion of a particle in a strong magnetic field can be analyzed asymptotically. In a strong magnetic field, $\delta \equiv \rho_L/L$ is small, where $\rho_L = v_\perp/|\Omega|$ is the gyro-radius (also called the Larmor radius), $v_\perp$ is the particle velocity perpendicular to the magnetic field, $\Omega = qB/m$ is the gyro-frequency, B is the magnitude of the magnetic field, q is the particle charge, m is the particle mass, and L is a typical macroscopic length scale. To lowest order in δ, the particle will simply gyrate along the magnetic field (see Fig. 1.6). To next order in δ, if the magnetic field is curved or non-uniform, the guiding center of gyration will drift perpendicularly off of magnetic field lines [5]. From hereon, the words "parallel" and "perpendicular" without additional clarification will refer to directions relative to the local magnetic field. The $O(\delta)$ perpendicular guiding center drift is given by:

$$\mathbf{v}_D = \frac{\mathbf{E}\times\mathbf{B}}{B^2} + \frac{1}{\Omega}\mathbf{b}\times\left(\frac{\mu}{m}\nabla B + v_\parallel^2\boldsymbol{\kappa}\right), \tag{1.3}$$

where $\mathbf{E}$ is the electric field, $\mathbf{b} = \mathbf{B}/B$, $\mu = mv_\perp^2/2B$ is the magnetic moment, $v_\parallel$ is the parallel particle velocity, and $\boldsymbol{\kappa} = \mathbf{b} \cdot \nabla \mathbf{b}$ is the magnetic curvature. The three components of the perpendicular guiding center drift appearing in Eq. (1.3) are the $\mathbf{E} \times \mathbf{B}$ drift, the ∇B drift, and the curvature drift.

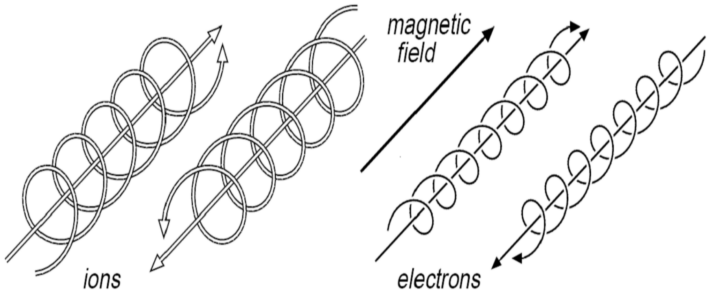

Figure 1.6: Gyration of electron and ions along a magnetic field [6].

As the guiding center of gyration streams along the magnetic field, its parallel motion will be affected both by any parallel component of the electric field, as well as by what is termed the "mirror force." The mirror force, which can be derived from the aforementioned asymptotic analysis of the particle's motion in a strong magnetic field, is given as

$$F_m = -\mu \mathbf{b} \cdot \nabla B \, . \tag{1.4}$$

It is a force, parallel to the magnetic field, that opposes the particle traveling into a region of stronger magnetic field.

For δ small, it can also be shown that that both the magnetic moment μ and total energy $mv^2/2 + q\phi$ are approximate constants of the particle's motion [5]. Here $v = \sqrt{v_\perp^2 + v_\parallel^2}$, and ϕ is the electrostatic potential.

1.2.2 The need for a "twist" in the magnetic field

The perpendicular particle drifts in a strong magnetic field lead to an important result, namely, that a purely toroidal magnetic field cannot confine a plasma in equilibrium. A quasi-neutral plasma must satisfy $\nabla \cdot \mathbf{J} = 0$. However, the perpendicular particle drifts lead to a non-zero divergence of the perpendicular current $(\nabla \cdot \mathbf{J}_\perp)$[1]. This then necessitates a non-zero divergence of the parallel current

[1]The lowest order perpendicular current, the diamagnetic current, can be found immediately from Eq. (1.2). It takes the form $\mathbf{B} \times \nabla p/B^2$. That the divergence of the diamagnetic current is equal to the divergence of the lowest order current due to the guiding center drifts is shown in Sec. 4.5 of Ref. [5]. The crux of the argument therein is that, in the fluid picture, an additional current appears due to the curl of the plasma magnetization. When this additional current is added to the current due to the guiding center drifts, the diamagnetic current is obtained. Because the divergence of a

($\nabla \cdot \mathbf{J}_{\|}$) and hence a non-zero $\mathbf{J}_{\|}$. However, a non-zero $\mathbf{J}_{\|}$ is inconsistent with a purely toroidal field. A "twist" in the magnetic field is therefore required (see Fig. 1.7 below for an illustration of the helically twisting path of a magnetic field line on a magnetic surface). How the twist is accomplished separates different fusion concepts in MCF.

1.2.3 Tokamaks

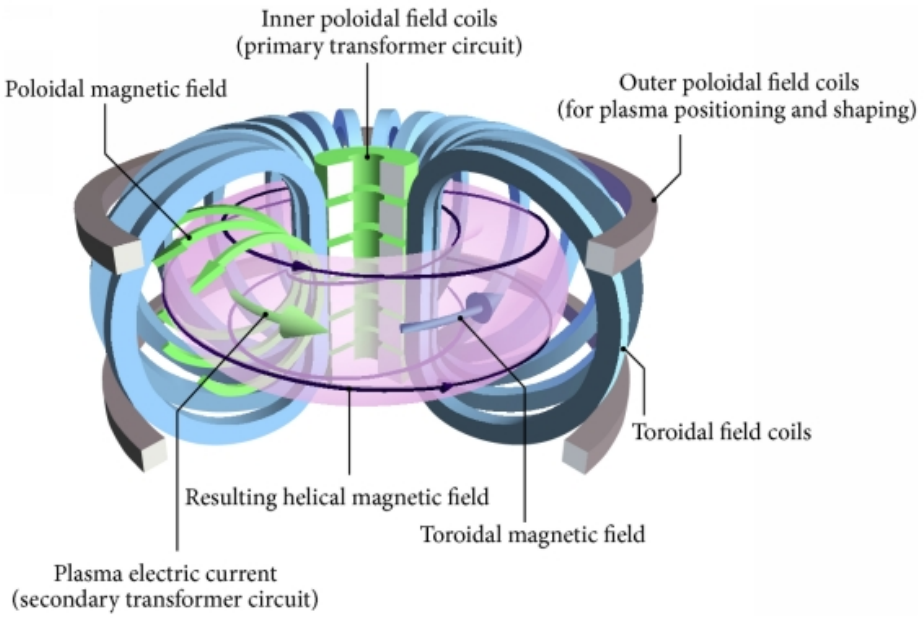

Figure 1.7: A sample schematic of a tokamak [7].

Tokamaks are a type of MCF device that achieve the needed **B** field through a toroidal plasma current. In tokamaks, the toroidal field is generated by magnets wrapped around the outside of the torus, and the "twist" in the field (the poloidal component of the field) is generated by the toroidal plasma current. In Fig. 1.7, a sample schematic of a tokamak is shown. Modern-day tokamaks have many current drive methods, including induced current from a large central transformer, as well as RF wave and neutral beam induced plasma current [8].

1.2.4 Some additional preliminary definitions

A common scheme used to label magnetic surfaces in MCF is the poloidal flux, which is the amount of magnetic flux ($\int \mathbf{dS} \cdot \mathbf{B}$) through a ribbon-like surface that extends outward from the magnetic axis (the center of the nested tori) to the magnetic surface in question, (see Fig. 1.8 for an illustration

curl is zero, taking the divergence of the diamagnetic current recovers the divergence of the current due to the guiding center drifts.

of the ribbon-like surface used). Because the magnetic surfaces are labeled using the magnetic flux, they are also called "flux surfaces". ψ from this point forward will represent the poloidal flux divided by 2π. It is often convenient to normalize ψ, so that it goes from 0 at the magnetic axis to 1 at the last closed flux surface. $\tilde{\psi}$ will represent normalized ψ.

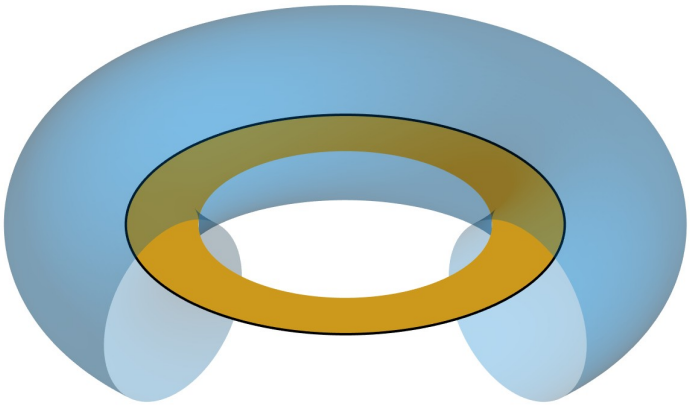

Figure 1.8: A sample toroidal magnetic surface (blue), with the magnetic axis (black), and the ribbon used to calculate the poloidal flux for this surface (gold).

If the toroidal configuration is assumed to be azimuthally symmetric, the magnetic field can be represented as

$$\mathbf{B} = I\nabla\phi + \nabla\phi \times \nabla\psi \ , \tag{1.5}$$

where $I = RB_\phi$, and B_ϕ is the ϕ-component of $\mathbf{B}$. Here, ϕ is the toroidal angle, defined opposite the conventional azimuthal angle in a cylindrical coordinate system so that ($R = \sqrt{X^2 + Y^2}$,Z,ϕ) (with (X, Y, Z) Cartesian coordinates) is right-handed. It can also be shown for the equilibrium magnetic field that I is a flux function (constant on flux surfaces).

One can average a quantity over an infinitesimal volume centered around a flux surface. This is called the flux surface average, and can be represented in axisymmetric geometry as

$$\langle f(\psi,\theta)\rangle = \int_0^{2\pi} \frac{f(\psi,\theta)\mathrm{d}\theta}{\mathbf{B}\cdot\nabla\theta} \Big/ \int_0^{2\pi} \frac{\mathrm{d}\theta}{\mathbf{B}\cdot\nabla\theta} \, . \tag{1.6}$$

Here, the poloidal angle θ measures the angular position on a flux surface. The definition of θ is allowed to be arbitrary as long as it only varies in the poloidal plane.

1.2.5 Collisional effects in tokamaks

In plasmas, collisions between individual particles are mediated by the long-range Coulomb force. Because of this, a particle's motion in a plasma is deflected more due to the cumulative effect of many small-angle Coulomb collision events than due to the effect of one large-angle scattering event. In addition, as the plasma becomes hotter, the average kinetic energy of its constituent particles increases. The relative velocity between any two particles in the plasma will, on average, be of the same order as the average speed of its particles. Particles with a larger relative velocity between them will spend less time interacting with each other via the Coloumb force. The effect of discrete Coloumb collision events on a typical particle's motion in a hotter plasma is therefore less than in a colder plasma (i.e., the particle can move a longer distance before its motion is deflected by collisions).

In sufficiently hot MCF plasmas, particles move "relatively far" (which will be quantified shortly) along the magnetic field before being deflected by collisions. This allows the particles to sample large regions of the magnetic geometry. The nature of particle dynamics in strong magnetic fields (see Sec. 1.2.1) then leads to particles in different parts of velocity space executing fundamentally different types of orbits.

In a tokamak, the magnitude of the magnetic field can be shown to be roughly proportional to $1/R$, where R is the radial coordinate in a cylindrical coordinate system. Therefore, on the inboard side of the tokamak the magnetic field is stronger than on the outboard side. As particles move along the magnetic field, because of the "twist" inherent in the field in MCF, the particles will sample regions of both higher and weaker magnetic field. As particles travel from a region of weaker magnetic field to a region of stronger magnetic field, their motion will be opposed by the mirror force (see Eq. (1.4)). Here is noted the velocity space coordinate $\xi = v_{\|}/v = \cos(\theta_{\text{pitch}})$, where (θ_{pitch}) is the pitch angle of the particle's velocity relative to the local magnetic field. Particles with sufficiently large (θ_{pitch}) will eventually have their motion parallel to the magnetic field stopped by the mirror force and they will begin moving in the reverse direction. These particles are called "trapped" – they are not able to complete their orbit around the magnetic surface. Particles with sufficiently small (θ_{pitch}) are not completely stopped in their parallel motion by the mirror force, and they are able to complete their orbit around the magnetic surface. These particles are called "passing".

In addition, particles will drift off a magnetic surface due to the ∇B and curvature drifts. The combined effects of the perpendicular drifts and the mirror force cause the trapped particle orbits to look banana shaped, when projected onto the poloidal plane. These orbits are therefore called

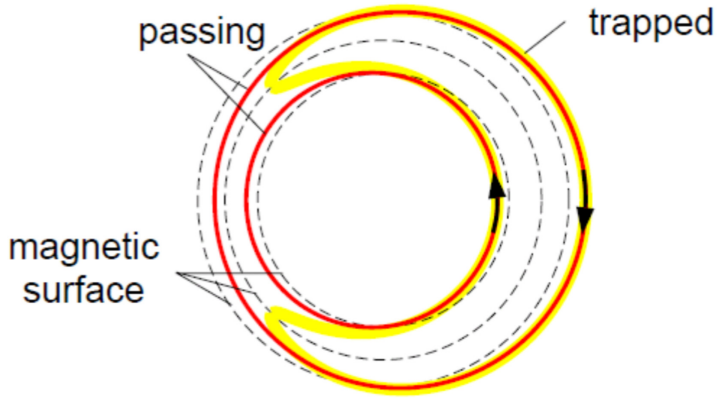

Figure 1.9: Projection of typical trapped and passing particle guiding center orbits in the poloidal plane. Here, the perpendicular particle drifts are in the vertical direction. [9]

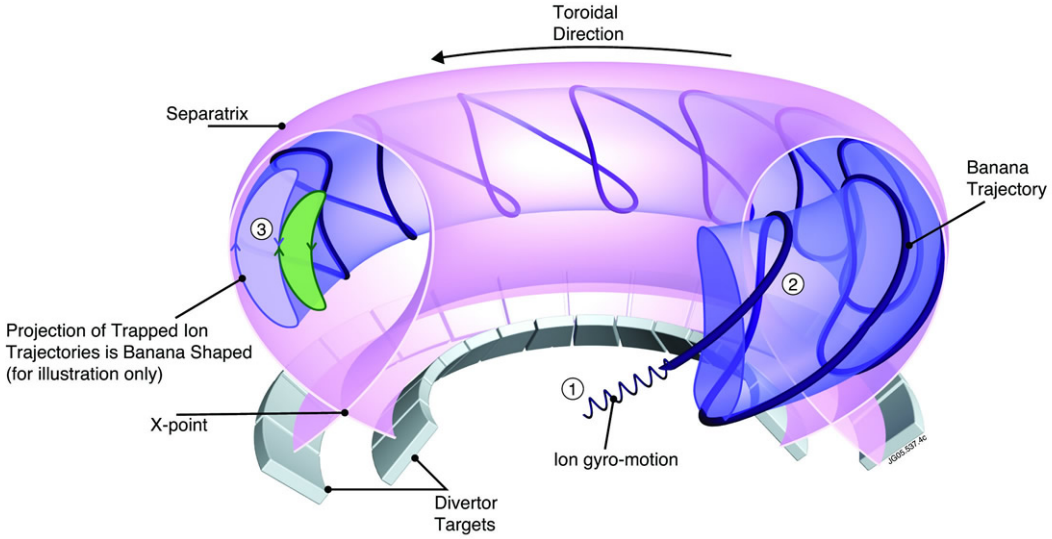

Figure 1.10: A typical trapped particle orbit in a tokamak with the toroidal component of the motion included. [10]

banana orbits. See Fig. 1.9 for an illustration of the shape of typical trapped and passing particle orbits in a tokamak, projected onto the poloidal plane. See also Fig. 1.10 for an illustration of a typical trapped particle orbit in a tokamak with the toroidal component of the motion included. Transport that includes the effects of trapped and passing particle motion in a toroidal configuration is called neoclassical transport. The regime where trapped particles are able to complete many banana orbits before being deflected by collisions is called the "banana regime".

The ratio of the effective collision frequency required to scatter a trapped particle out of its magnetic well to the bounce frequency of its banana orbit can be made explicit for a high aspect ratio

equilibrium (where the aspect ratio is defined as R_0/r, with r the distance from the magnetic axis, and R_0 the R coordinate of the magnetic axis in a cylindrical coordinate system). This parameter, termed the collisionality, is given for the ions by the relation:

$$\nu^\star = \frac{\nu_{ii}}{\epsilon^{3/2}} \cdot \left(\frac{qR}{v_{Ti}} \right) \equiv \frac{\hat{\nu}}{\epsilon^{3/2}} \,. \tag{1.7}$$

Here, $\epsilon = r/R_0$ is the inverse aspect ratio, q is the safety factor ($q = \langle \mathbf{B} \cdot \nabla\phi \rangle / \langle \mathbf{B} \cdot \nabla\theta \rangle$), $v_{Ti} = \sqrt{2T_i/m_i}$ is the ion thermal speed (with T_i the ion temperature and m_i the ion mass),

$$\nu_{ii} = \frac{n_i Z_{\text{eff}}^4 e^4 \ln(\Lambda_{ii})}{4\pi\epsilon_0^2 m_i^2 v_{Ti}^3} \,, \tag{1.8}$$

is the ion-ion collision frequency, ϵ_0 is the permittivity of free space, n_i is the ion number density, Z_{eff} is the effective atomic number of the ions, $e \approx 1.6 \cdot 10^{-19}$ C is the elementary charge unit,

$$\ln(\Lambda_{ii}) = 23 - \ln \left[\frac{Z_{\text{eff}}^2}{T_i} \left(\frac{2 \times 10^{-6} n_i Z_{\text{eff}}^2}{T_i} \right)^{1/2} \right] \,, \tag{1.9}$$

is the ion-ion Coulomb logarithm [11]. In Eq. (1.9), T_i is measured in eV without an implied Boltzmann factor multiplication, and n_i is measured in m^{-3}. For low aspect ratio equilibria, $\hat{\nu}$ is a sufficient parameter to determine the collisionality regime (with the collisionless regime defined by $\hat{\nu} \ll 1$ in this case). $\hat{\nu}$ is simply the ratio of the approximate connection length on the flux surface (i.e., the approximate parallel distance an ion must travel on the flux surface to orbit the torus once poloidally) to the mean free path in the plasma (v_{Ti}/ν_{ii}). This then provides a precise definition of a particle moving "relatively far" along the magnetic field before being deflected by collisions. It is also noted that for similar temperatures and low enough Z_{eff}, the mean free path for the electrons is of the same order as that for the ions (thereby making both $\hat{\nu}$ and $\nu^\star$ for the electrons roughly equivalent to that for the ions).

1.3 Closure problem in fluid theory

A set of fluid equations can be obtained by taking velocity-space integrals (termed "moments") of an appropriately specified kinetic equation (see Ch. 2). A standard set of fluid equations for species j are:

$$\frac{\partial n_j}{\partial t} + \nabla \cdot (n_j \mathbf{u}_j) = 0, \tag{1.10}$$

$$m_j n_j \left(\frac{\partial \mathbf{u}_j}{\partial t} + \mathbf{u}_j \cdot \nabla \mathbf{u}_j \right) = q_j n_j (\mathbf{E} + \mathbf{u}_j \times \mathbf{B}) - \nabla p_j - \nabla \cdot \mathbf{\Pi}_j + \mathbf{R}_j \ , \tag{1.11}$$

$$\frac{3}{2} n_j \left(\frac{\partial T_j}{\partial t} + \mathbf{u}_j \cdot \nabla T_j \right) = -n_j T_j (\nabla \cdot \mathbf{u}_j) - \nabla \cdot \mathbf{q}_j - \mathbf{\Pi}_j : \nabla \mathbf{u}_j + G_j \ , \tag{1.12}$$

where $p_j = n_j T_j$ is the pressure, n_j is the number density, T_j is the temperature, $\mathbf{u}_j$ is the flow, m_j is the mass, q_j is the charge, $\mathbf{\Pi}_j$ is the viscous stress tensor, $\mathbf{R}_j$ is the collisional friction force, $\mathbf{q}_j$ is the heat flux, and G_j is the collisional heat friction.

Additional moments of the kinetic equation can be taken to specify the time evolution of unknown quantities that appear in Eqs. (1.10)-(1.12) such as $\mathbf{q}_j$ and $\mathbf{\Pi}_j$. However, more unspecified quantities appear in doing so. Fluid theory has a closure problem – certain quantities in the fluid equations must be specified in terms of the remaining fluid variables, and no rigorous way exists to do this that is valid in all regimes. Closure methods exist for some regimes where local analytic approximations are valid (such as high collisionality regimes where $\nu^\star \gg 1$ [12, 13, 14, 15, 16]), but in other regimes many physical processes become intrinsically kinetic (such as low collisionality regimes where $\nu^\star \ll 1$ [17, 18, 19, 20]). The cores of modern-day and future tokamak devices often fall into the low collisionality regime where local analytic closures do not exist. In this work, numerical methods for solving a Chapman-Enskog-like (CEL) δf drift kinetic closure scheme [21, 22, 23] (also see Sec. 2.2) are analyzed and applied to accurately and efficiently model plasma dynamics across all regimes in a fluid-based formalism[2].

1.4 Extended magnetohydrodynamics (MHD) fluid model

In magnetohydrodynamics (MHD), the total flow is defined as a mass-density weighted average of the electron and ion flows, namely $\mathbf{u} = (1/\rho) \sum_{j=i,e} m_j n_j \mathbf{u}_j$. Here, $\rho = \sum_{j=i,e} m_j n_j$ is the total mass density. In the ordering scheme used herein, $\rho \approx n_i m_i$ and $\mathbf{u}_i \approx \mathbf{u}$ because of the smallness

[2] It is noted that a full-f drift kinetic approach could be equivalently used instead of a kinetic closure of a fluid-based formalism; however, this comes with its own challenges, such as dealing with numerical noise in advancing the full kinetic distribution function. This work will focus instead on utilizing a δf drift kinetic approach to self-consistently close a set of fluid equations.

of m_e/m_i. The momentum equation for the total flow is found by adding together the momentum equations for the ion and electron flow. Under the assumption of quasineutrality ($Z_{\text{eff}} n_i = n_e$), the electric field vanishes from the momentum equation for the total flow. Momentum conservation also dictates that the collisional friction forces from the different species exactly cancel (which can also be seen from the form of the operator representing the effects of discrete Coulomb collision events between ions and electrons [19]). In the extended MHD framework, Ohm's law is derived by solving for the electric field in the electron momentum equation, and substituting in the total flow in place of the electron flow. With these manipulations, the momentum equation for the total flow and the Ohm's law for the electric field are:

$$\rho\left(\frac{\partial \mathbf{u}}{\partial t} + \mathbf{u}\cdot\nabla\mathbf{u}\right) + \nabla\cdot\left(m_i n_i\left(\frac{m_e Z_{\text{eff}}}{m_i}\mathbf{u}_i(\mathbf{u}-\mathbf{u_e}) + \mathbf{u}_e(\mathbf{u}-\mathbf{u}_i)\right)\right) = \mathbf{J}\times\mathbf{B} - \nabla p - \sum_{j=i,e}\nabla\cdot\mathbf{\Pi}_j\ , \tag{1.13}$$

where $p = p_e + p_i$ is the total pressure, and

$$\begin{aligned}\mathbf{E} = &-\mathbf{u}\times\mathbf{B} + \frac{1}{n_e e}\mathbf{R}_e + \frac{1}{n_e e}\left[\left(\frac{1}{1+\frac{m_e Z_{\text{eff}}}{m_i}}\right)\mathbf{J}\times\mathbf{B} - \nabla p_e\right] - \frac{1}{n_e e}\nabla\cdot\mathbf{\Pi}_e \\ &- \frac{m_e}{e}\frac{\partial}{\partial t}\left(\mathbf{u} - \left(\frac{1}{1+\frac{m_e Z_{\text{eff}}}{m_i}}\right)\frac{\mathbf{J}}{n_e e}\right)\ .\end{aligned} \tag{1.14}$$

Because m_e/m_i is small, an ordering scheme can be imposed on these two equations. Here we follow the ordering scheme in Ref. [23] which orders $\sqrt{m_e/m_i} \sim O(\delta_i)$, where δ_i is the ratio of the ion gyro-radius to macroscopic length scale. The electron gyro-radius is smaller than the ion one by $O(\sqrt{m_e/m_i})$ (assuming similar temperatures) so that $\delta_e \sim O(\sqrt{m_e/m_i}\delta_i)$. The flows are also assumed small so that $\mathbf{u}_e \sim \mathbf{u}_i \sim O(\delta_i v_{Ti})$. Keeping terms up to $O(\delta_i n_i m_i v_{Ti}^2/L)$ in Eq. (1.13) and up to $O(\delta_e m_e v_{Te}^2/(eL))$ in Eq. (1.14) (where $v_{Te} = \sqrt{2T_e/m_e}$ is the electron thermal speed), the following equations are obtained:

$$\rho\left(\frac{\partial \mathbf{u}}{\partial t} + \mathbf{u}\cdot\nabla\mathbf{u}\right) = \mathbf{J}\times\mathbf{B} - \nabla p - \nabla\cdot\mathbf{\Pi}_i\ , \tag{1.15}$$

$$\mathbf{E} = -\mathbf{u}\times\mathbf{B} + \frac{1}{n_e e}\mathbf{R}_e + \frac{1}{n_e e}\left[\left(\frac{1}{1+\frac{m_e Z_{\text{eff}}}{m_i}}\right)\mathbf{J}\times\mathbf{B} - \nabla p_e\right] - \frac{1}{n_e e}\nabla\cdot\mathbf{\Pi}_e\ . \tag{1.16}$$

The advective term ($\mathbf{u}\cdot\nabla\mathbf{u}$) in the total momentum equation has been left in, although it is small in this ordering scheme. The electron viscous stress tensor in the total momentum equation has been omitted, as it is smaller than the ion one by $O(\sqrt{m_e/m_i})$. This is because the deviation from local thermal equilibrium is smaller for the electrons than for the ions by an amount of $O(\sqrt{m_e/m_i})$ in a magnetized plasma. The time derivative term in Ohm's law has also been omitted, which is valid if the change in the current averaged over any timescales faster than the MHD timescale (L/v_{Ti}) is zero.

1.4.1 The resistive Ohm's law

If the electrons and ions are sufficiently cold, further terms in Ohm's law can be neglected. It is noted that $\mathbf{J}\times\mathbf{B} - \nabla p_e = \nabla p_i$ to lowest order. It is also assumed that the collisional friction force between the electrons and the ions takes the form $\mathbf{R}_e = n_e m_e \nu_{ei}(\mathbf{u}_i - \mathbf{u}_e)$, where

$$\nu_{ei} = \frac{4}{3\sqrt{\pi}}\frac{n_i Z_{\text{eff}}^2 e^4 \ln(\Lambda_{ei})}{4\pi\epsilon_0^2 m_e^2 v_{Te}^3}\,, \tag{1.17}$$

is the electron-ion collision frequency and

$$\ln(\Lambda_{ei}) = \begin{cases} 23 - \ln\left(\dfrac{n_e^{1/2} Z_{\text{eff}}}{T_e^{3/2}}\right) & T_i\dfrac{m_e}{m_i} < T_e < 10 Z_{\text{eff}}^2\ \text{eV} \\ 24 - \ln\left(\dfrac{n_e^{1/2}}{T_e}\right) & T_i\dfrac{m_e}{m_i} < 10 Z_{\text{eff}}^2\ \text{eV} < T_e \end{cases}\,, \tag{1.18}$$

is the electron-ion Coulomb logarithm [11]. In Eq. (1.18), T_e and T_i are measured in eV without an implied Boltzmann factor multiplication, and n_e is measured in m^{-3}. With these assumptions, Ohm's law for a sufficiently cold plasma becomes:

$$\mathbf{E} = -\mathbf{u}\times\mathbf{B} + \eta\mathbf{J}\,, \tag{1.19}$$

where $\eta = \nu_{ei} m_e/(n_e e^2)$ is the resistivity. In reality, the resistivity will be anisotropic, with the parallel resistivity differing from the given η by an $O(1)$, Z_{eff}-dependent constant.

Eq. (1.19) is often used in MHD simulations, even though most fusion plasmas of interest are not cold enough to justify dropping the additional terms in Eq. (1.16). However, Eq. (1.19) does include the reconnection physics relevant to MCF plasmas of interest.

1.5 Fundamentally kinetic phenomena in low collisionality MCF plasmas

Many physical processes depend sensitively on quantities in the fluid equations that require kinetic closure when not in the high collisionality regime. A few physical processes are summarized below. It is noted that kinetic contributions to these physical processes remain important even in moderately collisional regimes (i.e., when not in the asymptotic high collisionality regime).

1.5.1 Poloidal flow damping

The poloidal flow in a tokamak damps due to particle collisions on the ion-ion collision time scale $(1/\nu_{ii})$ [24, 25]. The flow is indirectly affected by the ion-ion collision operator through the ion viscous stress tensor in the momentum equation for the total flow. It can be shown in the banana regime that the steady state poloidal flow is carried completely by the passing particle population [18, 19]. The steady state is reached when passing particles reach a collisional equilibrium among themselves and with the trapped particle population.

Due to the speed dependence of the collision operator (see Sec. 2.4), poloidal ion flow and poloidal heat flow processes are also intrinsically coupled. This coupling to heat flow processes results in a steady-state poloidal flow proportional to the cross-field ion temperature.

1.5.2 Edge-localized mode (ELM) suppression with resonant magnetic perturbations (RMPs)

Under the right conditions in a tokamak, a bifurcation to a state of low transport is observed [26, 27]. This high confinement state (also called H-mode for high confinement mode) is an attractive mode of operation for future power plants. It is a state characterized by sharp density, temperature, and pressure gradients at the edge of the plasma, just inside the last closed magnetic surface. However, H-mode suffers from some notable downsides. The increase in the pressure gradient at the edge leads to a destabilization of MHD modes which leads to periodic bursts of particles and energy being expelled to the walls of the device [28]. These edge-localized modes (ELMs) must be prevented or mitigated in future plasma devices to prevent erosion of wall materials [29].

Application of what are called resonant magnetic perturbations (RMPs) has been found to suppress ELMs in H-mode discharges [30]. RMPs are applied perturbations to the equilibrium magnetic field that have the same helicity as the magnetic field just inside the sharp gradient edge

region. It has been postulated (and simplified simulation models seem to corroborate) that these RMPs suppress ELMs by forcing magnetic reconnection just inside the sharp gradient edge region, thereby resulting in the creation of a magnetic island chain [30, 31, 32]. This island chain then results in increased transport, limiting the gradients, and thereby keeping the edge region below the MHD stability boundary.

High fidelity simulation of ELM suppression by RMPs in tokamaks requires appropriate consideration of all the physical processes that can influence forced magnetic reconnection (FMR) just inside the sharp gradient region. Among all these, the flow physics plays an important role. A finite flow can screen reconnection through $-\mathbf{u} \times \mathbf{B}$ balancing $\eta\mathbf{J}$ in Eq. (1.19). In addition, the poloidal flow, as previously stated, is strongly affected by the ion viscous stress tensor which requires a kinetic closure when not in the asymptotic collisional regime. Kinetics, therefore, plays an important role in FMR dynamics, especially when not in the asymptotic collisional regime.

1.5.3 Neoclassical Tearing Modes (NTMs)

In the banana regime, a spontaneous current (the so-called "bootstrap" current) arises in response to gradients of n and T perpendicular to the magnetic field. This current arises from a complex interaction between both trapped and passing particles in the plasma [19]. A small seed island on a magnetic surface can flatten the pressure across the island, which causes a helical perturbation of the bootstrap current on that surface. This perturbation can reinforce the initial island size which leads to further island growth. This is what is called the "neoclassical tearing mode" (NTM) [33]. Certain stabilizing effects require the seed island to be a critical size before growth occurs, which shows that an NTM is linearly stable but can become non-linearly unstable.

Because of induced eddy currents in the wall, the induced large island can "lock" to the wall, stopping the plasma rotation, and resulting in a loss of plasma confinement (i.e., a plasma disruption). A survey of JET[3] tokamak disruptions [34] found NTMs to be the leading cause of all disruptions. Wall locking is not required for an NTM however, and most NTMs in current tokamaks don't lock. Locking is anticipated to be more of a problem in larger, lower rotating tokamaks such as ITER[4].

High fidelity modeling of NTM dynamics requires modifying the standard resistive Ohm's law (Eq. (1.19)). Specifically, $\eta\mathbf{J}$ is replaced by a kinetic closure for the collisional friction force $\mathbf{R}_e$, and the electron viscous stress tensor $\mathbf{\Pi}_e$ is included in Ohm's law. Both $\mathbf{R}_e$ and $\mathbf{\Pi}_e$ contribute to bootstrap current effects, which can be seen from manipulation of the results in Ch. 12 of Ref. [19]. The flow dynamics also remain important for the reconnection processes involved. In other words, NTM modeling requires a kinetic closure for both relevant ion quantities as well as relevant electron quantities in the fluid equations.

[3] Joint European Torus, located in Oxfordshire, UK.

[4] ITER is an experimental tokamak being built near the Cadarache facility in southern France [35].

1.5.4 Previous work using heuristic closure schemes in NIMROD

The plasma fluid code NIMROD [36] is most often used to solve the fluid equations for a plasma in toroidal or slab geometry, but has many other capabilities, including kinetic modeling [37, 38, 39, 40, 41, 42, 43, 44, 45, 46, 47]. Previous work in NIMROD has investigated both the problem of forced magnetic reconnection as well as that of NTMs. Both problems were addressed in NIMROD using simplified models.

In Ref. [48], the problem of forced magnetic reconnection was addressed by applying a time-dependant magnetic boundary condition to a sheared slab magnetic configuration in NIMROD, utilizing a heuristic closure for the ion viscous stress tensor. It was found that above a critical strength of the imposed magnetic perturbation, the equilibrium field underwent a bifurcation from a high-slip, flow-screened state without reconnection to a low-slip, field-penetrated state with reconnection. This work could be extended to toroidal geometry, using a more rigorous (kinetic) closure scheme for the ion viscous stress tensor.

In Ref. [49], NTM dynamics were modeled in NIMROD by applying a rotating, time-evolving RMP to an equilibrium based on a kinetic reconstruction of DIII-D ITER Baseline Scenario (IBS) discharge 174446 at 3390 ms. Heuristic closures for both the electron and ion viscous stress tensors and the electron collisional friction force were also used. It was found that the RMP destabilized a sequence of core modes, which grew in amplitude and deposited energy into a slowly growing $2/1$ mode. After the $2/1$ mode reached a critical amplitude, it transitioned into a robustly growing phase governed by the modified Rutherford equation [33]. The NTM dynamics were found to be sensitive to the damping parameter used in the heuristic closures for the ion and electron viscous stress tensors. For small electron damping, the RMP was insufficient to excite an NTM. For large electron damping, the robustly growing $2/1$ growth phase was reached before an excitation of core modes. Interesting insights would likely be gained by extending this work to include more rigorous (kinetic) closures for the electron and ion viscous stress tensors and the electron collisional friction force.

1.6 Thesis

In this work, a numerical method for solving a Chapman-Enskog-like (CEL) [21, 22, 23] continuum kinetic model for plasmas is formulated, analyzed, and applied in the plasma fluid code NIMROD. The CEL approach is a kinetic approach that allows rigorous closure of the plasma fluid equations in all collisionality regimes. It is an approach that resembles the one performed in Ref. [50] where the zeroth order in δ kinetic distribution function (f_0) is a time-evolving, flow-shifted Maxwellian, evaluated with the full number density, flow, and temperature. This definition for f_0 leads to an $O(\delta)$ kinetic equation that analytically enforces that the first order kinetic distortion f_1 have no number

density, flow, and temperature moments. The fluid variables in this method are allowed to deviate far from an initial zeroth order MHD equilibrium. The fluid equations are closed by incorporating appropriate velocity space moments of the first order kinetic distortion. Although the ion physics is focused on in this work, CEL closure of electron quantities of interest is also implemented.

It is noted that a kinetic closure for energetic particles is implemented in both M3D-C1-K [51] (an extension of the plasma fluid code M3D-C1 [52]) and NIMROD [42]. These implementations, however, differ from the self-consistent CEL closure of the bulk electron and ion species discussed herein. It is also noted that previous work has implemented the CEL approach for simplified scenarios (assuming all of: restricting to one spatial and velocity space dimension, not including a magnetic field, and simplified representations of collisional processes) [53, 54, 55]. In contrast, the CEL implementation discussed herein assumes none of these restrictions.

In Chapter 2, the kinetic theory applicable to the CEL closure scheme utilized herein is outlined. In Chapter 3, the equation model used and its numerical implementation in NIMROD is outlined . In Chapter 4, kinetic aspects of the CEL implementation in NIMROD are compared to a previously benchmarked, fixed-background δf implementation in NIMROD [44], to analytics, and to another drift kinetic code DK4D [56] which implements a similar CEL drift kinetic equation as the one in NIMROD. Good agreement is found for the poloidal flow coefficient compared between NIMROD continuum kinetic formulations, analytics, and DK4D. In Chapter 5, a stability analysis of the linearized fluid-kinetic system is performed to help elucidate methods to make the time advance of the full system numerically stable. It is found that centering the heat flux at the beginning of the time step and the ion temperature at the end of the time step in the kinetic equation allows for a numerically stable time advance of the coupled fluid-kinetic system. In addition, it is shown that numerical stability is impossible to achieve without explicitly enforcing key tenets of the CEL closure approach, in particular, that the number density (n), flow ($\mathbf{u}$), and temperature (T) moments of the kinetic distortion remain small in time. It is shown that with a method to constrain these moments, it is possible to remove both the numerical growth and numerical damping from the linear modes. In Chapter 6, an axisymmetric benchmark of the full CEL approach in NIMROD is performed. The results from the linear stability analysis are applied to allow for a numerically stable, fully nonlinear, axisymmetric evolution of profiles in NIMROD, wherein is observed the asymptotic evolution of the flow in a DIII-D tokamak equilibrium (based on DIII-D ITER Baseline Scenario (IBS) discharge 174446 at 3390 ms [57, 49]). The self-consistently computed results are compared to analytics and to results from the aforementioned, previously benchmarked, fixed-background δf implementation in NIMROD. Agreement with prediction is found for both the dynamics and asymptotics of the flow. In Chapter 7, the methodology for applying the CEL implementation to general non-axisymmetric problems of interest is discussed. And in Chapter 8, both a summary of results and an outlook for future applications of the CEL implementation in NIMROD to MCF

problems of interest is provided.

2 KINETIC THEORY

In kinetic theory, macroscopic plasma properties are modeled by taking into account the microscopic motions and interactions of its individual particles [58]. Continuum kinetics is the framework used herein, but other paradigms exist, such as the particle-in-cell (PIC) method [59].

In continuum kinetics, a kinetic distribution function f (which represents the density of particles in phase space – physical space + velocity space) is evolved in time for each species. The exact distribution function, f_{exact}, is given as:

$$f_{\text{exact}}(\mathbf{x}, \mathbf{v}, t) = \sum_{i=1}^{N} \delta(\mathbf{x} - \mathbf{x}_i(t))\delta(\mathbf{v} - \mathbf{v}_i(t)) \,, \tag{2.1}$$

where N is the number of particles, and $\mathbf{x}_i(t)$ and $\mathbf{v}_i(t)$ represent the exact (deterministic) trajectories of the particles in phase space. f_{exact} can be shown to satisfy the following kinetic equation [60]:

$$\frac{\partial f_{\text{exact}}}{\partial t} + \mathbf{v} \cdot \nabla f_{\text{exact}} + \frac{q}{m}(\mathbf{E}_{\text{micro}} + \mathbf{v} \times \mathbf{B}_{\text{micro}}) \cdot \nabla_{\mathbf{v}} f_{\text{exact}} = 0 \,, \tag{2.2}$$

where $\mathbf{E}_{\text{micro}}$ and $\mathbf{B}_{\text{micro}}$ are the exact microscopic electric and magnetic fields in the plasma, respectively. Solving the exact kinetic equation is equivalent to solving for the positions and velocities of every particle in the plasma, which is computationally intractable. An ensemble-averaged kinetic equation can be solved instead. The ensemble-averaged kinetic equation, which governs the time evolution of the ensemble-averaged f, takes the form [60]:

$$\frac{\partial f}{\partial t} + \mathbf{v} \cdot \nabla + \frac{q}{m}(\mathbf{E} + \mathbf{v} \times \mathbf{B}) \cdot \nabla_{\mathbf{v}} f = C(f) \,, \tag{2.3}$$

where f represents the ensemble-averaged distribution function, the electric and magnetic fields are also ensemble averaged, and $C(f)$ represents a Coulomb collision operator which closes the system by taking into account the effect of discrete binary particle collision events.

2.1 Drift kinetics

In magnetized fusion plasmas, as previously stated, the ratio of gyro-radius to macroscopic length scales (δ) is a small parameter for all charged species. Therefore, the kinetic equation and kinetic distribution function can be expanded asymptotically in δ. It turns out that, to lowest order in δ, the

distribution function is independent of the gyro-angle in velocity space [5]. This means that, for strongly magnetized plasmas, only the evolution of the gyro-averaged distribution function needs to be tracked. f will represent the gyro-averaged distribution function from this point forward. Expanding the gyro-averaged kinetic equation accurately to $O(\delta)$, and using the magnetic moment μ and kinetic energy $w = mv^2/2$ as velocity space coordinates gives [61, 5]:

$$\frac{\partial f}{\partial t} + (\mathbf{v}_\parallel + \mathbf{v}_D + \mathbf{v}_{\parallel D}) \cdot \nabla f + \left[\mu \frac{\partial B}{\partial t} + q(\mathbf{v}_\parallel + \mathbf{v}_D + \mathbf{v}_{\parallel D}) \cdot \mathbf{E} \right] \frac{\partial f}{\partial w} + \mu \left[\frac{\mu_0 J_\parallel}{B^2} \mathbf{b} \cdot \mathbf{E} + v_\parallel \mathbf{b} \cdot \nabla \left(v_\parallel \frac{\mu_0 J_\parallel}{B\Omega} \right) \right] \frac{\partial f}{\partial \mu} = C(f) \,, \tag{2.4}$$

where $\mu_0 = 4\pi \cdot 10^{-7}$ H/m is the permeability of free space, $\mathbf{J}_\parallel = \mathbf{b} \cdot (\nabla \times \mathbf{B})/\mu_0$, $J_\parallel = |\mathbf{J}_\parallel|$, $\mathbf{v}_\parallel = v_\parallel \mathbf{b}$, and

$$\mathbf{v}_{\parallel D} = \frac{\mu}{m\Omega} \mu_0 \mathbf{J}_\parallel \tag{2.5}$$

is a parallel guiding center drift, which is needed to make the guiding center flow along the magnetic field accurate to $O(\delta)$ given the particle velocity.

The gyro-averaged distribution function for a plasma in a closed confinement system (i.e., for a plasma confined on closed magnetic surfaces) can be shown to be a local Maxwellian with no zeroth order flow, to zeroth order in δ [5]. Therefore f can also be expanded as $f = f_M + f_1$, where $f_M = \frac{n}{\pi^{3/2} v_T^3} e^{-w/T}$ is a local Maxwellian (with $v_T = \sqrt{2T/m}$ the thermal speed, T the temperature, and n the number density), and f_1 is an $O(\delta)$ perturbation. Then, considering only $O(\delta)$ terms in the kinetic equation, the following is obtained:

$$\frac{\partial f_1}{\partial t} + \mathbf{v}_\parallel \cdot \nabla f_1 = C(f_1) - \frac{\partial f_M}{\partial t} - (\mathbf{v}_\parallel + \mathbf{v}_D + \mathbf{v}_{\parallel D}) \cdot \nabla f_M - \left[\mu \frac{\partial B}{\partial t} + q(\mathbf{v}_\parallel + \mathbf{v}_D + \mathbf{v}_{\parallel D}) \cdot \mathbf{E}) \right] \frac{\partial f_M}{\partial w} \,. \tag{2.6}$$

There is ambiguity here in the definition of the number density and temperature of the Maxwellian. If the Maxwellian is defined with the full n and T, then this equation analytically enforces that the number density and temperature moments of f_1 are zero for all time if they start at zero (which can

be shown rigorously). If instead the Maxwellian is defined only with the zeroth order, equilibrium n and T (with the zeroth order, equilibrium n and T satisfying the zeroth order MHD equilibrium force balance $\nabla(\sum_j n_j T_j) = \mathbf{J} \times \mathbf{B}$) the time derivative of the Maxwellian will vanish, and the number density and temperature moments of f_1 will in general not be zero. Different definitions for f_M will be explored in the next two subsections.

2.2 The Chapman-Enskog-like (CEL) approach

It is convenient for f_M to contain the full $O(\delta)$ (compared to v_T) fluid flow ($\mathbf{u}$) in addition to the full n and T. The parallel flow can easily be included in the Maxwellian, but including the full $\mathbf{u}$ would make f_M gyrophase-dependent. This would contradict the assumption that f is the gyro-averaged distribution function. To do this correctly, transforming the kinetic equation to the macroscopic flow reference frame must be done first. After this, the gyro-averaging is performed and the $f = f_M + f_1$ ansatz is imposed. The steps for this derivation can be found in Refs. [23, 62]. The result for the $O(\delta_i)$ ion kinetic equation is quoted in terms of velocity space coordinates $\xi = v_\parallel / v$ and $s = v / v_{Ti}$. $O(\delta_i^2)$ terms are not presently considered in this analysis, because this work is mainly concerned with processes that evolve on the diamagnetic drift timescale or faster [23, 62]. The $O(\delta_i)$ ion kinetic equation is:

$$
\begin{aligned}
&\frac{\partial f_{i1}}{\partial t} + \xi s v_{Ti} \mathbf{b} \cdot \nabla f_{i1} - \frac{1-\xi^2}{2\xi} \left[\xi s v_{Ti} \left(\mathbf{b} \cdot \nabla \ln B - \frac{\mathbf{b} \cdot \nabla \ln n_i}{s^2} \right) \right] \frac{\partial f_{i1}}{\partial \xi} \\
&\quad + \left[\frac{\xi v_{Ti}}{2} \left(\mathbf{b} \cdot \nabla \ln n_i - s^2 \mathbf{b} \cdot \nabla \ln T_i \right) - \frac{s}{2} \frac{\partial \ln T_i}{\partial t} \right] \frac{\partial f_{i1}}{\partial s} - C_{ii}\left(f_{i1}, f_{Mi}\right) - C_{ii}\left(f_{Mi}, f_{i1}\right) = \\
&\quad \left\{ \frac{\xi s v_{Ti}}{T_i} \left(\frac{5}{2} - s^2 \right) \mathbf{b} \cdot \nabla T_i + \frac{\xi s v_{Ti}}{n_i T_i} \left[\frac{2}{3} \mathbf{b} \cdot \nabla \pi_{i\parallel} - \pi_{i\parallel} \mathbf{b} \cdot \nabla \ln B \right] \right. \\
&\quad + P_2(\xi) \frac{2}{3} s^2 \left(\nabla \cdot \mathbf{u}_i - 3 \mathbf{b} \cdot [\mathbf{b} \cdot \nabla \mathbf{u}_i] \right) \\
&\quad + \frac{2}{3 n_i T_i} \left(s^2 - \frac{3}{2} \right) \nabla \cdot \left(q_{i\parallel} \mathbf{b} \right) + \left[-\frac{2}{3} s^2 P_2(\xi) \left(\left(s^2 - \frac{5}{2} \right) (2\boldsymbol{\kappa} - \nabla \ln B) + \nabla \ln n_i \right) - \right. \\
&\quad \left. \left. \frac{4}{3} \left(\frac{1}{2} s^4 - \frac{5}{2} s^2 + \frac{15}{8} \right) (\boldsymbol{\kappa} + \nabla \ln B) \right] \cdot \left(\frac{\nabla T_i \times \mathbf{b}}{Z_{\mathrm{eff}} e B} \right) \right\} f_{Mi} + \nabla \cdot D_{f_{i1}} \nabla f_{i1} \,, \qquad (2.7)
\end{aligned}
$$

where

$$q_{i\parallel} = \int \mathrm{d}^3 v (m_i v^2/2) v_\parallel f_{i1} \,, \tag{2.8}$$

is the ion parallel heat flux,

$$\pi_{i\parallel} = m_i \int \mathrm{d}^3 v \; v^2 P_2 \left(v_\parallel / v\right) f_{i1} = \left(p_{i\parallel} - p_{i\perp}\right) \,, \tag{2.9}$$

is the ion parallel viscosity, $(p_{i\parallel} - p_{i\perp})$ is the difference between the parallel and perpendicular pressures for the ions, $P_2(\xi)$ is the second order Legendre polynomial in ξ, and C_{ii} represents the full linearized ion-ion Coulomb collision operator, split into its test and field particle components (see Sec. 2.4). A diffusive term is also included to assist in stabilizing non-linear numerical instabilities, with corresponding diffusivity $D_{f_{i1}}$. It is noted that integral forms for $q_\parallel$ [37, 38, 43] and $\pi_\parallel$ [39], which were previously implemented in NIMROD to study parallel transport in lower collisionality regimes, captured non-local effects, but failed to develop the physics of the fully time-dependent, self-consistent hybrid fluid/CEL kinetic implementation discussed herein.

Additional higher-order ($O(\delta_i^2)$) terms proportional to $\partial T_i/\partial t$, $\mathbf{b}\cdot\nabla \ln n_i$, and $\mathbf{b}\cdot\nabla \ln T_i$ also appear on the LHS of Eq. (2.7). The $\partial T_i/\partial t$ and $\mathbf{b}\cdot\nabla \ln T_i$ terms are needed for consistency with Ref. [23], and appear due to the temperature-dependent speed normalization ($s = v/v_{Ti}$). The $\mathbf{b}\cdot\nabla \ln n_i$ terms appear in Ref. [23] because $L(\mathbf{b}\cdot\nabla \ln n_i)$ is ordered as $O(1)$. Quasineutrality shows that $L(\mathbf{b}\cdot\nabla \ln n_i)$ is actually $O(\delta_i)$ [5], but these terms are included for consistency with Ref. [23].

Eq. (2.7) requires a coupling to evolution equations for n_i, $\mathbf{u}_i$, T_i, and $\mathbf{B}$. This approach is termed the Chapman-Enskog-like (CEL) approach [21, 22]. It is an approach that resembles the one performed in Ref. [50] where f_{Mi} is a flow-shifted Maxwellian evaluated with the full n_i, $\mathbf{u}_i$, and T_i. The CEL approach places no additional restrictions on the deviation of the fluid variables from equilibrium – they are allowed to deviate far from an initial zeroth order MHD equilibrium.

Eq. (2.7) analytically enforces that the fluid moments (i.e., the number density, flow, and temperature moments) of f_{i1} remain at zero if they start at zero. We can show this by taking fluid moments of the kinetic equation. We take the $\int \mathrm{d}^3 v$, $\int \mathrm{d}^3 v m_i v_\parallel$, and $\int \mathrm{d}^3 v m_i v^2/2$ moments of the kinetic equation (with $D_{f_{i1}} = 0$) to obtain the following three equations:

$$\begin{aligned} \frac{\partial (f_{i1})_{(n_i)}}{\partial t} + \frac{1}{m_i}\mathbf{b}\cdot\nabla (f_{i1})_{(n_i m_i u_{i\parallel})} - \frac{1}{m_i}(f_{i1})_{(n_i m_i u_{i\parallel})}\mathbf{b}\cdot\nabla \ln B \\ - \left(C_{ii}\left(f_{i1}, f_{Mi}\right) + C_{ii}\left(f_{Mi}, f_{i1}\right)\right)_{(n_i)} = 0 \,, \end{aligned} \tag{2.10}$$

$$\frac{\partial (f_{i1})_{(n_i m_i u_{i\|})}}{\partial t} + \frac{2}{3}\mathbf{b}\cdot\nabla (f_{i1})_{((3/2)n_i T_i)} - \left(T_i (f_{i1})_{(n_i)}\right)\mathbf{b}\cdot\nabla \ln n_i \\ - \left(C_{ii}\left(f_{i1}, f_{Mi}\right) + C_{ii}\left(f_{Mi}, f_{i1}\right)\right)_{(n_i m_i u_{i\|})} = 0 \,, \tag{2.11}$$

and

$$\frac{\partial (f_{i1})_{((3/2)n_i T_i)}}{\partial t} - \frac{T_i}{m_i}(f_{i1})_{(n_i m_i u_{i\|})}\mathbf{b}\cdot\nabla \ln n_i \\ - \left(C_{ii}\left(f_{i1}, f_{Mi}\right) + C_{ii}\left(f_{Mi}, f_{i1}\right)\right)_{((3/2)n_i T_i)} = 0 \,, \tag{2.12}$$

where the subscripts indicate the moment taken of that quantity, namely:

$$(\_\_\_)_{(n_i)} = \int \mathrm{d}^3 v (\_\_\_) \,, \tag{2.13}$$

$$(\_\_\_)_{(n_i m_i u_{i\|})} = m_i \int \mathrm{d}^3 v v_{\|} (\_\_\_) \,, \tag{2.14}$$

and

$$(\_\_\_)_{((3/2)n_i T_i)} = \int \mathrm{d}^3 v m_i v^2/2 (\_\_\_) \,. \tag{2.15}$$

The fluid moments of the ion-ion part of the collision operator vanish analytically, but we leave them in the above equations (for reasons that will be seen hereafter). By noting that the rate of change of these moments depends on nonzero values of these moments, we observe from Eqs. (2.10), (2.11), and (2.12) that if the fluid moments of f_{i1} are zero at $t = 0$, they will remain zero for all time. *This fact holds analytically, but whether it holds in a numerical implementation will depend on the details of the numerical implementation.*

2.3 The fixed background approach

If, in Eq. (2.6), the Maxwellian is evaluated only with the zeroth order, equilibrium n and T (from the zeroth order MHD equilibrium force balance), the time derivative of the Maxwellian vanishes.

This approach is referred to herein as the fixed background approach. In this approach, perturbations to n, $u_\parallel$ (the parallel flow), and T are carried completely by f_1, and the only coupling needed is to an evolution equation for $\mathbf{B}$ and the perpendicular flow ($\mathbf{u}_\perp$). Because the fluid variables are derived from f_1, they are $O(\delta)$. This places a natural restriction on how far the fluid variables are allowed to deviate from an initial zeroth order MHD equilibrium, namely, not farther than $O(\delta)$.

The kinetic equation in this approach can be specified simply in the lab frame. We assume the zeroth order equilibrium number density and temperature are constant on flux surfaces ($\mathbf{b}\cdot\nabla n_{i0} = \mathbf{b}\cdot\nabla T_{i0} = 0$). In terms of velocity space variables ξ and $s = v/v_{Ti0}$ (with s normalized by the equilibrium ion thermal speed) the kinetic equation for the ions becomes:

$$\begin{aligned}
&\frac{\partial f_{i1}}{\partial t} + \xi s v_{Ti0}\mathbf{b}\cdot\nabla f_{i1} - \frac{1-\xi^2}{2\xi}\left[\xi s v_{Ti0}\mathbf{b}\cdot\nabla \ln B\right]\frac{\partial f_{i1}}{\partial \xi} - C_{ii}\left(f_{i1}, f_{Mi0}\right) - C_{ii}\left(f_{Mi0}, f_{i1}\right) \\
&\quad = -\left(\mathbf{v}_D + \mathbf{v}_{\parallel D}\right)\cdot\left\{\left(s^2 - \frac{3}{2}\right)\nabla \ln T_{i0} + \nabla \ln n_{i0} + \frac{Z_{\text{eff}} e \nabla \phi_0}{T_{i0}}\right\} f_{Mi0} \\
&\qquad + \left\{\left(1-\xi^2\right) s^2 \frac{\partial \ln B}{\partial t} + \xi s v_{Ti0}\frac{Z_{\text{eff}} e \mathbf{b}\cdot\mathbf{E}_1}{T_{i0}}\right\} f_{Mi0}\,,
\end{aligned} \tag{2.16}$$

where subscripts of 0 or 1 represent zeroth order and first order quantities, respectively, $\mathbf{E}_1 = -\nabla\phi_1 - \partial\mathbf{A}/\partial t$, ϕ_0 and ϕ_1 are the zeroth order and first order electrostatic potentials, respectively, and $\mathbf{A}$ is the vector potential ($\mathbf{B} = \nabla\times\mathbf{A}$). Here, the zeroth order electrostatic potential is constant on magnetic surfaces and is allowed to evolve in time, consistent with the ordering scheme. If the magnetic field is evolving on longer timescales than the dynamics of interest, the $\partial \ln B/\partial t$ term and $\partial\mathbf{A}/\partial t$ part of $\mathbf{E}_1$ may be neglected. It is common in the relevant literature to also neglect $\mathbf{b}\cdot\nabla\phi_1$ [18, 19]. Both the $\partial \ln B/\partial t$ and $\mathbf{b}\cdot\mathbf{E}_1$ terms will be neglected in Eq. (2.16) from this point forward.

2.4 Collision Operator

Here, the form of the full linearized ion-ion collision operator is specified. The $O(\delta_i)$ linearized ion-ion collision operator takes the same form whether it is evaluated in the lab frame or the macroscopic flow reference frame (corrections between the two representations are $O(\delta_i^2)$). It is made up of a "test particle" part, and a "field particle" part. The test particle part is given as:

$$C(f_{i1}, f_{Mi}) = \frac{\nu_{ii}}{2s^3}(\phi_{\text{err}}(s) - \chi(s))\left\{\frac{\partial}{\partial \xi}\left((1-\xi^2)\frac{\partial f_{i1}}{\partial \xi}\right)\right\} + \frac{\nu_{ii}}{s^2}\frac{\partial}{\partial s}\left\{\chi(s)\left[s\frac{\partial f_{i1}}{\partial s} + 2s^2 f_{i1}\right]\right\}, \tag{2.17}$$

where $\phi_{\text{err}}(s) \equiv (2/\sqrt{\pi})\int_0^s \mathrm{d}u e^{-u^2}$ is the error function, and $\chi(s) = (\phi_{\text{err}}(s) - s\phi'_{\text{err}}(s))/(2s^2)$ is the Chandrasekhar function. The field particle part is given as:

$$C(f_{Mi}, f_{i1}) = \frac{Z_{\text{eff}}^4 e^4 \ln(\Lambda_{ii})}{4\pi\epsilon_0^2 m_i^2}\left\{4\pi f_{i1} + \frac{2s^2}{v_{Ti}^4}\frac{\partial G_i}{\partial s^2} - \frac{2}{v_{Ti}^2}H_i\right\} f_{Mi}\,, \tag{2.18}$$

where $G_i \equiv \int \mathrm{d}^3\mathbf{v}' f_{i1}|\mathbf{v} - \mathbf{v}'|$ and $H_i \equiv \int \mathrm{d}^3\mathbf{v}' f_{i1}|\mathbf{v} - \mathbf{v}'|^{-1}$ are the Rosenbluth potentials.

3 EQUATION MODEL AND NUMERICAL IMPLEMENTATION IN NIMROD

The equations used for the fluid part of the model are stated here. In Ch. 6, this model will be used to simulate the damping of the flow in an axisymmetric tokamak configuration. In future work, this model will also be used to simulate FMR dynamics in realistic tokamak geometries. We use the extended MHD ordering scheme stated previously in Sec. 1.4. The viscous heating terms $\mathbf{\Pi}_i : \nabla \mathbf{u}_i$ and $\mathbf{\Pi}_e : \nabla \mathbf{u}_e$ in the ion and electron temperature evolution equations are also neglected, as they are $O(\delta_i^2)$ and $O(\delta_e^2)$ respectively, due to the smallness of the flows and both species being near local thermodynamic equilibrium. The ion collisional heat friction G_i is also neglected in the ion temperature equation, which can be justified if the plasma is sufficiently collisionless (which it is for the equilibrium used herein). Because the electron temperature evolution is not as important to the physics problems investigated herein, an approximate electron temperature equation is evolved. A resistive Ohm's law (Eq. (1.19)) is also assumed for $\mathbf{E}$, which is sufficient for the FMR processes of interest that this particular model will be used for in future work. The equations are:

$$m_i n_i \left(\frac{\partial \mathbf{u}}{\partial t} + \mathbf{u} \cdot \nabla \mathbf{u} \right) = \mathbf{J} \times \mathbf{B} - \nabla p - \nabla \cdot \mathbf{\Pi}_i \ , \tag{3.1}$$

$$\frac{\partial n_e}{\partial t} + \nabla \cdot (n_e \mathbf{u}) = \nabla \cdot D_n \nabla n_e \ , \tag{3.2}$$

$$\frac{3}{2} n_i \left(\frac{\partial T_i}{\partial t} + \mathbf{u} \cdot \nabla T_i \right) = -n_i T_i (\nabla \cdot \mathbf{u}) - \nabla \cdot \mathbf{q}_i \ , \tag{3.3}$$

$$\frac{3}{2} n_e \left(\frac{\partial T_e}{\partial t} + \mathbf{u} \cdot \nabla T_e \right) = -n_e T_e (\nabla \cdot \mathbf{u}) - \nabla \cdot \mathbf{q}_e \ , \tag{3.4}$$

$$\frac{\partial \mathbf{B}}{\partial t} = -\nabla \times (-\mathbf{u} \times \mathbf{B} + \eta \mathbf{J}) \ , \tag{3.5}$$

and

$$\mathbf{J} = \frac{1}{\mu_0}\nabla \times \mathbf{B} \,. \tag{3.6}$$

Here, $\mathbf{q}_i$ and $\mathbf{q}_e$ are the ion and electron heat fluxes, respectively, and D_n is a small number density diffusivity (used for numerical stability). For the resistivity η, a Spitzer resistivity of the form $\eta = \eta_0 \left(T_{e,\mathrm{ref}}/T_e\right)^{3/2}$ is used, where $T_{e,\mathrm{ref}}$ is a reference temperature for the electrons, and η_0 is the resistivity at $T_{e,\mathrm{ref}}$. A magnetic diffusivity of $\eta_0/\mu_0 = 8.99 \times 10^{-3}$ m^2/s is used herein, which is close to the on-axis value for the equilibrium used in Ch. 6 to benchmark the full CEL approach. An anisotropic diffusive heat flux for the electrons of the form $\mathbf{q}_e = -\kappa_{e,\parallel}\mathbf{bb}\cdot\nabla T_e - \kappa_{e,\perp}\left(\mathbf{I}-\mathbf{bb}\right)\cdot\nabla T_e$ is assumed, where $\kappa_{e,\parallel}$ and $\kappa_{e,\perp}$ are parallel and perpendicular conductivities, respectively, for the electron temperature, $\mathbf{I}$ is the identity tensor, and $\mathbf{b} = \mathbf{B}/B$. Herein, $\kappa_{e,\parallel} = n_{e,0}\cdot(10^8$ m^2/s), and $\kappa_{e,\perp} = n_{e,0}\cdot(1$ m^2/s), where $n_{e,0} = 9.488\times10^{19}$ m^{-3} is a reference number density for the electrons (which is close to the on-axis number density for the equilibrium used in Ch. 6).

The CEL approach is used to close the fluid system for the ion heat flux and ion viscous stress tensor. We assume that the ion viscous stress tensor is of the CGL [63] form (i.e., the traceless part of the CGL total ion pressure tensor) plus a small diffusive part, namely,

$$\mathbf{\Pi}_i = \pi_{i\parallel}\left(\mathbf{bb}-\mathbf{I}/3\right) - \left(n_{e0}/Z_{\mathrm{eff}}\right)m_i D_u\left(\nabla\mathbf{u} + (\nabla\mathbf{u})^T - \frac{2}{3}\mathbf{I}\left(\nabla\cdot\mathbf{u}\right)\right), \tag{3.7}$$

where D_u is a momentum diffusivity, and that the ion heat flux is of the form of the Braginskii diamagnetic cross heat flux [12] plus a parallel and a small diffusive part, namely,

$$\mathbf{q}_i = q_{i\parallel}\mathbf{b} + \left(\frac{5n_iT_i}{2eZ_{\mathrm{eff}}B}\mathbf{b}\times\nabla T_i\right) - \left(n_{e0}/Z_{\mathrm{eff}}\right)D_{T_i}\nabla T_i \,, \tag{3.8}$$

where D_{T_i} is an ion temperature diffusivity. The parallel viscosity $\pi_{i\parallel}$ and the parallel heat flux $q_{i\parallel}$ are both found through appropriate moments of the first order ion distribution function f_{i1}, as previously given in Eqs. (2.8) and (2.9).

3.1 Numerical implementation of the CEL closure approach in NIMROD

Here, the numerical implementation of the CEL closure approach applied to the NIMROD code is outlined. NIMROD uses a C^0 finite element expansion in the poloidal (R-Z) plane, and a Fourier

expansion in the toroidal direction to describe all fluid variables. The magnetic field **B** is used as an example of this. In NIMROD's finite element expansion, **B** at the k-th time step is expressed as:

$$\mathbf{B}^k(R,Z,\phi) = \mathbf{B}_0^k(R,Z) + \sum_{n=1}^{\infty}(\mathbf{B}_n^k(R,Z)e^{in\phi} + (\mathbf{B}_n^k(R,Z))^* e^{-in\phi}) \ , \tag{3.9}$$

where $*$ represents the complex conjugate, $\mathbf{B}_0^k(R,Z)$ is the axisymmetric component of the magnetic field, and

$$\mathbf{B}_n^k(R,Z) = \sum_p \sum_j \alpha_j(R,Z) B_{n,j,p}^k \mathbf{e}_p \ . \tag{3.10}$$

Here, $B_{n,j,p}^k$ are the coefficients of expansion, $\mathbf{e}_p$ are unit vectors in either the $\hat{\mathbf{R}}$, $\hat{\mathbf{Z}}$, or $\hat{\boldsymbol{\phi}}$ directions, and $\alpha_j(R,Z)$ is a product of 1D finite element basis functions in the poloidal plane. The Galerkin approach is used to create the matrix equation from the model.

For the kinetic first order distribution function, the same representation as above is used for physical space. For velocity space, a finite element (FE) expansion [44] is used for the pitch angle coordinate, and a collocation approach [64, 44] is used for the radial velocity space coordinate s. A Legendre polynomial expansion can also be used for the pitch angle coordinate, but for reasons that will be seen in Ch. 4, this expansion is less effective in the collisionless regime. This gives the following expansion for the velocity space part of f_{i1} at the k-th time step:

$$f_{i1,n,j}^k(\eta, s_m) = \sum_l f_{i1,n,j,l,m}^k Q_l(\eta) \ , \tag{3.11}$$

where s_m is a speed collocation point, η is a logical pitch angle coordinate, $Q_l(\eta)$ are either Legendre polynomials ($Q_l(\eta) = P_l(\xi)$) or 1D FE basis functions, and $f_{i1,n,j,l,m}^k$ are the coefficients of expansion. For the speed derivative terms of the collision operator, a further expansion of f_{i1} is performed in speed polynomials orthogonal with respect to the weight function e^{-s^2}. Choosing the speed collocation points to be the zeros of the N_s degree speed polynomial (where N_s is the number of speed collocation points) then means that the speed derivatives of $f_{i1,n,j}^k$ at a given collocation point can be expressed as a linear combination of the $f_{i1,n,j,l,m}^k$. The Galerkin approach is used for the pitch angle part of velocity space to obtain the matrix equation from the model (with an integration by parts being first performed on the Lorentz pitch-angle scattering part of the collision operator in Eq. (2.17) when 1D FE basis functions are used). The numerical evaluation of the

Rosenbluth potential integrals in Eq. (2.18) is discussed in detail in Ref. [46].

3.1.1 Further details on ξ representation

For finite elements in ξ, a logical variable η is defined such that it varies from 0 to the total number of cells as ξ varies from -1 to 1. The mapping from η to ξ allows the velocity grid to vary depending on the position in physical space, allowing the cell boundaries in ξ to vary. This allows one to have cell boundaries in ξ that follow either approximately or exactly the trapped-passing boundary (tpb), which is crucial for convergence in ξ when running in the banana collisionality regime.

m_η is defined as the total number of FE cells, $m_{\eta p}$ as the number of cells in the positive passing domain (which mirrors the number in the negative passing domain), and $m_{\eta t}$ as the number of cells in the trapped domain. Then the mapping from η to ξ is given as:

$$\xi = \begin{cases} -\cos\left(\dfrac{\theta_{tp}\eta}{m_{\eta p}}\right), & 0 \le \eta < m_{\eta p} \\ -\cos\left(\theta_{tp} + (\pi - 2\theta_{tp})\dfrac{\eta - m_{\eta p}}{m_{\eta t}}\right), & m_{\eta p} \le \eta < m_{\eta p} + m_{\eta t} \\ \cos\left(\dfrac{\theta_{tp}(\eta - m_\eta)}{m_{\eta p}}\right), & m_{\eta p} + m_{\eta t} \le \eta \le m_\eta \end{cases}, \tag{3.12}$$

where θ_{tp} defines the spacing of the vertex nodes (cell boundaries) in ξ. For uniform grid spacing in pitch angle (i.e., in $\cos^{-1}(\xi)$), $\theta_{tp} \equiv (\pi m_{\eta p})/m_\eta$. To have the grid spacing be constant on flux surfaces but to have the cell boundaries agree with the tpb on the outboard midplane, $\theta_{tp} = \cos^{-1}(\sqrt{1 - B_{\min}/B_{\max}})$, where $B_{\min}$ and $B_{\max}$ are the minimum and maximum value of $|\mathbf{B}|$ on the magnetic surface in question. This is called an approximate tpb grid. For exact tpb grids, $\theta_{tp} = \cos^{-1}(\sqrt{1 - B/B_{\max}})$, where $B(R, Z)$ is the local $|\mathbf{B}|$. To prevent a trapped domain of zero width on the inboard midplane for exact tpb grids, θ_{tp} is defined as:

$$\theta_{tp} = \begin{cases} \cos^{-1}(\sqrt{1 - B/B_{\max}}), & \sqrt{1 - B/B_{\max}} > \delta_{\min} \\ \cos^{-1}(\delta_{\min}), & \sqrt{1 - B/B_{\max}} \le \delta_{\min} \end{cases}, \tag{3.13}$$

where $\delta_{\min}$ is some small number ($\delta_{\min} \lesssim 0.01$). For an illustration of the exact tpb grid, see Fig. 3.1.

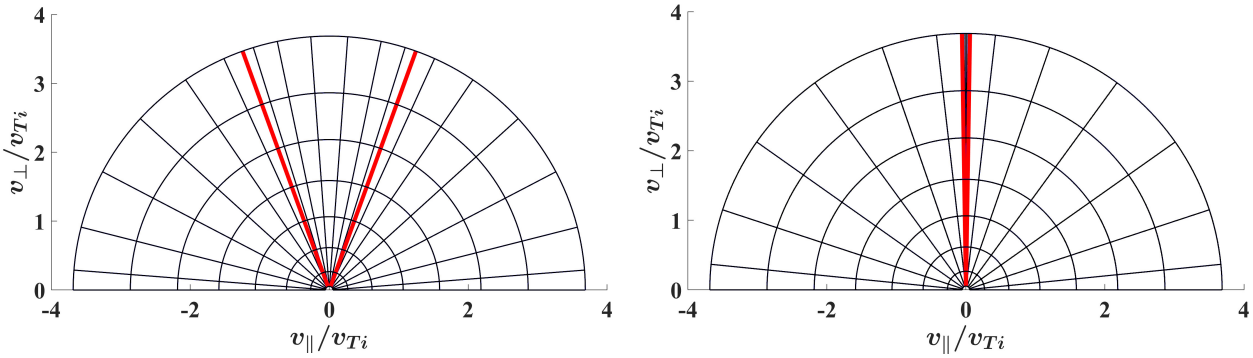

Figure 3.1: Sample exact tpb FE grids on both the outboard (left) and inboard (right) midplanes of a high aspect ratio equilibrium (see Sec. 4.4), with 3 cells in η ($m_\eta = 3$), and $m_{\eta p} = m_{\eta t} = 1$. On the left, the cell boundaries correspond to the tpb, and are highlighted in red. On the right the cell boundaries correspond only approximately to the tpb, with $\delta_{\min} \approx 0.016$. The sample grids here use 8 s points, and GLL polynomials in each cell of degree 7. Note the natural packing of the GLL nodes at the tpb.

When using 1D finite elements (in the η coordinate), either Lagrange polynomials with internal nodes uniformly spaced in η, or Gauss-Lobatto-Legendre (GLL) polynomials with internal nodes coinciding with the anti-nodes of the Legendre polynomial of the same degree as the FE polynomial basis functions (plus the end points), are used. The GLL set gives a natural packing around the tpb (see Fig. 3.1.)

The only other subtlety is that, when expanding the distribution function in η, there is an additional term that appears in the DKE. Specifically, by the chain rule:

$$\xi s v_{Ti} \mathbf{b} \cdot \nabla|_\xi f_{i1} \longrightarrow \xi s v_{Ti} \mathbf{b} \cdot \nabla|_\eta f_{i1} + \xi s v_{Ti} \frac{\partial f_{i1}}{\partial \eta} \mathbf{b} \cdot \nabla \eta \,, \tag{3.14}$$

where $\eta = \eta(\xi, R, Z, \phi)$ is the inverse of the mapping in Eq. (3.12), and where bars indicate which pitch angle variable is held fixed when taking the partial spatial derivatives. For general cases, this extra term is nonzero for velocity grids that vary on a magnetic surface.

While velocity grids that follow the exact tpb in velocity space have been used before [65, 66, 67], this is the first time they have been used with a higher order FE basis of GLL polynomials in pitch angle, in a code that can simulate the whole physical domain.

3.1.2 Time-Stepping Algorithm

All fluid and kinetic quantities are stepped in time using NIMROD's semi-implicit, leap-frog algorithm. It involves the use of a semi-implicit operator to assist in stabilizing low-frequency MHD waves, which is well documented in Refs. [36, 68]. Here, the time-stepping algorithm is outlined.

The flow is defined at integer time levels, and all other variables are defined at half-integer time levels, meaning halfway between the integer time levels. The model equations in time-discretized form are given as:

$$
\begin{aligned}
& m_i n_i^{j+1/2}\left(\frac{\Delta\mathbf{u}}{\Delta t}+\frac{1}{2}\mathbf{u}^j\cdot\nabla\Delta\mathbf{u}+\frac{1}{2}\Delta\mathbf{u}\cdot\nabla\mathbf{u}^j+\frac{1}{4}\Delta\mathbf{u}\cdot\nabla\Delta\mathbf{u}\right)-\Delta t\mathbf{L}^{j+1/2}(\Delta\mathbf{u}) \\
& \quad -\nabla\cdot\left[(n_{e0}/Z_{\text{eff}})m_iD_u\left(\nabla\Delta\mathbf{u}+(\nabla\Delta\mathbf{u})^T-\frac{2}{3}\mathbf{I}\,(\nabla\cdot\Delta\mathbf{u})\right)\right] \\
& = \mathbf{J}^{j+1/2}\times\mathbf{B}^{j+1/2}-m_in_i^{j+1/2}\mathbf{u}^j\cdot\nabla\mathbf{u}^j-\nabla(n_i^{j+1/2}T_i^{j+1/2}+n_e^{j+1/2}T_e^{j+1/2}) \\
& \quad -\nabla\cdot\left[\pi_{i\|}(f_{i1}^{j+1/2},T_i^{j+1/2})\left(\mathbf{b}^{j+1/2}\mathbf{b}^{j+1/2}-\mathbf{I}/3\right)\right] \\
& \quad +\nabla\cdot\left[(n_{e0}/Z_{\text{eff}})m_iD_u\left(\nabla\mathbf{u}^j+\left(\nabla\mathbf{u}^j\right)^T-\frac{2}{3}\mathbf{I}\left(\nabla\cdot\mathbf{u}^j\right)\right)\right]\,,
\end{aligned}
\tag{3.15}
$$

$$
\frac{\Delta n_e}{\Delta t}+\frac{1}{2}\nabla\cdot(\mathbf{u}^{j+1}\Delta n_e)-\nabla\cdot D_n\nabla\Delta n_e=-\nabla\cdot(\mathbf{u}^{j+1}n_e^{j+1/2})+\nabla\cdot D_n\nabla n_e^{j+1/2}\,,
\tag{3.16}
$$

$$
\begin{aligned}
& \frac{3\bar{n}_i}{2}\left(\frac{\Delta T_i}{\Delta t}+\frac{1}{2}\mathbf{u}^{j+1}\cdot\nabla\Delta T_i\right)+\frac{1}{2}\bar{n}_i\Delta T_i\nabla\cdot\mathbf{u}^{j+1} \\
& \quad +\nabla\cdot\left(\frac{1}{2}\left[\tilde{q}_{i\|}(f_{i1}^{j+1/2})\right]3(T_i^{j+1/2})^2\Delta T_i\mathbf{b}^{j+1/2}\right) \\
& \quad +\nabla\cdot\left(\frac{5\bar{n}_i}{2eZ_{\text{eff}}B^{j+1/2}}\left[\frac{1}{2}T_i^{j+1/2}\mathbf{b}^{j+1/2}\times\nabla\Delta T_i+\frac{1}{2}\Delta T_i\mathbf{b}^{j+1/2}\times\nabla T_i^{j+1/2}\right]\right) \\
& \quad -\nabla\cdot(n_{e0}/Z_{\text{eff}})D_{T_i}\nabla\Delta T_i \\
& = -\frac{3\bar{n}_i}{2}\mathbf{u}^{j+1}\cdot\nabla T_i^{j+1/2}-\bar{n}_iT_i^{j+1/2}\nabla\cdot\mathbf{u}^{j+1}-\nabla\cdot\left(\left[\tilde{q}_{i\|}(f_{i1}^{j+1/2})\right](T_i^{j+1/2})^3\mathbf{b}^{j+1/2}\right) \\
& \quad -\nabla\cdot\left(\frac{5\bar{n}_i}{2eZ_{\text{eff}}B^{j+1/2}}\left[T_i^{j+1/2}\mathbf{b}^{j+1/2}\times\nabla T_i^{j+1/2}\right]\right)+\nabla\cdot(n_{e0}/Z_{\text{eff}})D_{T_i}\nabla T_i^{j+1/2}\,,
\end{aligned}
\tag{3.17}
$$

$$\begin{aligned}
&\frac{3\bar{n}_e}{2}\left(\frac{\Delta T_e}{\Delta t}+\frac{1}{2}\mathbf{u}^{j+1}\cdot\nabla\Delta T_e\right)+\frac{1}{2}\bar{n}_e\Delta T_e\nabla\cdot\mathbf{u}^{j+1}\\
&\quad+\nabla\cdot\left(-\kappa_{e,\parallel}\mathbf{b}^{j+1/2}\mathbf{b}^{j+1/2}\cdot\nabla\Delta T_e-\kappa_{e,\perp}\left(\mathbf{I}-\mathbf{b}^{j+1/2}\mathbf{b}^{j+1/2}\right)\cdot\nabla\Delta T_e\right)\\
&=-\frac{3\bar{n}_e}{2}\mathbf{u}^{j+1}\cdot\nabla T_e^{j+1/2}-\bar{n}_e T_e^{j+1/2}\nabla\cdot\mathbf{u}^{j+1}\\
&\quad-\nabla\cdot\left(-\kappa_{e,\parallel}\mathbf{b}^{j+1/2}\mathbf{b}^{j+1/2}\cdot\nabla T_e^{j+1/2}-\kappa_{e,\perp}\left(\mathbf{I}-\mathbf{b}^{j+1/2}\mathbf{b}^{j+1/2}\right)\cdot\nabla T_e^{j+1/2}\right)\ ,
\end{aligned}\tag{3.18}$$

$$\frac{\Delta\mathbf{B}}{\Delta t}-\frac{1}{2}\nabla\times\left(\mathbf{u}^{j+1}\times\Delta\mathbf{B}\right)+\nabla\times\bar{\eta}\Delta\mathbf{J}=-\nabla\times\left[-\mathbf{u}^{j+1}\times\mathbf{B}^{j+1/2}+\bar{\eta}\mathbf{J}^{j+1/2}\right]\ ,\tag{3.19}$$

$$
\begin{aligned}
&\frac{\Delta f_{i1}}{\Delta t} + \xi s v_{Ti}^{j+3/2}\bar{\mathbf{b}}\cdot\nabla\Delta f_{i1} - \frac{1-\xi^2}{2\xi}\left[\xi s v_{Ti}^{j+3/2}\left(\bar{\mathbf{b}}\cdot\nabla\ln\bar{B} - \frac{\bar{\mathbf{b}}\cdot\nabla\ln\bar{n}_i}{s^2}\right)\right]\frac{\partial\Delta f_{i1}}{\partial\xi} \\
&\quad + \left[\frac{\xi v_{Ti}^{j+3/2}}{2}\left(\bar{\mathbf{b}}\cdot\nabla\ln\bar{n} - s^2\bar{\mathbf{b}}\cdot\nabla\ln T_i^{j+3/2}\right) - \frac{s}{2T_i^{j+3/2}}\frac{\Delta T_i}{\Delta t}\right]\frac{\partial\Delta f_{i1}}{\partial s} \\
&\quad - \left\{\frac{\xi s v_{Ti}^{j+3/2}}{\bar{n}_i T_i^{j+3/2}}\left[\frac{2}{3}\bar{\mathbf{b}}\cdot\nabla\left[\pi_{i\|}\left(\Delta f_{i1}, T_i^{j+3/2}\right)\right] - \left[\pi_{i\|}\left(\Delta f_{i1}, T_i^{j+3/2}\right)\right]\bar{\mathbf{b}}\cdot\nabla\ln\bar{B}\right]\right. \\
&\quad \left. + \theta_{q_{i\|}}\frac{2}{3\bar{n}_i T_i^{j+3/2}}\left(s^2 - \frac{3}{2}\right)\nabla\cdot\left(\left[q_{i\|}\left(\Delta f_{i1}, T_i^{j+3/2}\right)\right]\bar{\mathbf{b}}\right)\right\} f_{Mi}\left(\bar{n}_i, T_i^{j+3/2}\right) \\
&\quad - C_{ii}\left(\bar{n}_i, T_i^{j+3/2}, \Delta f_{i1}\right) - \nabla\cdot D_{f_{i1}}\nabla\Delta f_{i1} \\
&= -\xi s v_{Ti}^{j+3/2}\bar{\mathbf{b}}\cdot\nabla f_{i1}^{j+1/2} + \frac{1-\xi^2}{2\xi}\left[\xi s v_{Ti}^{j+3/2}\left(\bar{\mathbf{b}}\cdot\nabla\ln\bar{B} - \frac{\bar{\mathbf{b}}\cdot\nabla\ln\bar{n}_i}{s^2}\right)\right]\frac{\partial f_{i1}^{j+1/2}}{\partial\xi} \\
&\quad - \left[\frac{\xi v_{Ti}^{j+3/2}}{2}\left(\bar{\mathbf{b}}\cdot\nabla\ln\bar{n} - s^2\bar{\mathbf{b}}\cdot\nabla\ln T_i^{j+3/2}\right) - \frac{s}{2T_i^{j+3/2}}\frac{\Delta T_i}{\Delta t}\right]\frac{\partial f_{i1}^{j+1/2}}{\partial s} \\
&\quad + C_{ii}\left(\bar{n}_i, T_i^{j+3/2}, f_{i1}^{j+1/2}\right) + \left\{\frac{\xi s v_{Ti}^{j+3/2}}{T_i^{j+3/2}}\left(\frac{5}{2} - s^2\right)\bar{\mathbf{b}}\cdot\nabla T_i^{j+3/2}\right. \\
&\quad \left. + \frac{\xi s v_{Ti}^{j+3/2}}{\bar{n}_i T_i^{j+3/2}}\left[\frac{2}{3}\bar{\mathbf{b}}\cdot\nabla\left[\pi_{i\|}\left(f_{i1}^{j+1/2}, T_i^{j+3/2}\right)\right] - \left[\pi_{i\|}\left(f_{i1}^{j+1/2}, T_i^{j+3/2}\right)\right]\bar{\mathbf{b}}\cdot\nabla\ln\bar{B}\right]\right. \\
&\quad \left. + P_2(\xi)\frac{2}{3}s^2\left(\nabla\cdot\mathbf{u}^{j+1} - 3\bar{\mathbf{b}}\cdot\left[\bar{\mathbf{b}}\cdot\nabla\mathbf{u}^{j+1}\right]\right)\right. \\
&\quad \left. + \frac{2}{3\bar{n}_i T_i^{j+3/2}}\left(s^2 - \frac{3}{2}\right)\nabla\cdot\left(\left[q_{i\|}\left(f_{i1}^{j+1/2}, T_i^{j+3/2}\right)\right]\bar{\mathbf{b}}\right)\right. \\
&\quad \left. + \left[-\frac{2}{3}s^2 P_2(\xi)\left(\left(s^2 - \frac{5}{2}\right)\left(2\bar{\boldsymbol{\kappa}} - \nabla\ln\bar{B}\right) + \nabla\ln\bar{n}_i\right)\right.\right. \\
&\quad \left.\left. - \frac{4}{3}\left(\frac{1}{2}s^4 - \frac{5}{2}s^2 + \frac{15}{8}\right)\left(\bar{\boldsymbol{\kappa}} + \nabla\ln\bar{B}\right)\right]\cdot\left(\frac{\nabla T_i^{j+3/2}\times\bar{\mathbf{b}}}{Z_{\mathrm{eff}}e\bar{B}}\right)\right\} f_{Mi}\left(\bar{n}_i, T_i^{j+3/2}\right) \\
&\quad + \nabla\cdot D_{f_{i1}}\nabla f_{i1}^{j+1/2}\,, \qquad (3.20)
\end{aligned}
$$

Algorithm 1 Time advance algorithm for time step j

1. Advance $\mathbf{u}$ using Eq. (3.15) and store the value at the $j+1$ time step.
2. Advance n_e using Eq. (3.16) and store the average value over the time step.
3. Advance T_i using Eq. (3.17) and store the value at the $j+3/2$ time step (or store the predicted value for nonlinear problems).
4. Advance T_e using Eq. (3.18) and store the average value over the time step (or store the average of the initial and predicted values for nonlinear problems) for use in $\bar{\eta}$.
5. Advance $\mathbf{B}$ using Eq. (3.19) and store the average value over the time step.
6. Advance f_{i1} using Eq. (3.20) and store the value at the $j+3/2$ time step.
7. For nonlinear problems, perform a corrector step by resetting T_i and T_e to the $j+1/2$ time step, and advancing T_i and T_e again using Eqs. (3.17) and (3.18) respectively, but with the averaged magnetic field quantities ($\overline{\mathbf{B}}$, $\bar{\mathbf{b}}$, $\overline{B}$) used in place of ($\mathbf{B}^{j+1/2}$, $\mathbf{b}^{j+1/2}$, $B^{j+1/2}$) in those equations.
8. Store the values of all quantities at the end of their time steps, (i.e., at the $j+1$ time step for $\mathbf{u}$, and at the $j+3/2$ time step for all other quantities).

where Δ indicates the change over the time step[1], superscript indicates the time step, overbar indicates the average over the time step (with overbar of derived quantities being defined as calculated with the average of the fundamental quantities over the time step, i.e., $\bar{\eta} = \eta_0 \left(T_{e,\mathrm{ref}}/\overline{T}_e\right)^{3/2}$, $\overline{B} = |\overline{\mathbf{B}}|$, $\bar{\mathbf{b}} = \overline{\mathbf{B}}/\overline{B}$, $\bar{\boldsymbol{\kappa}} = \bar{\mathbf{b}} \cdot \nabla\bar{\mathbf{b}}$), tilde quantities split off the T_i dependence of the kinetic moments (i.e., $q_{i\|}\left(f_{i1}^{j+1/2}, T_i^{j+1/2}\right) = \left[\tilde{q}_{i\|}(f_{i1}^{j+1/2})\right]\left(T_i^{j+1/2}\right)^3$), $\theta_{q_{i\|}} \in [0,1]$ is a centering parameter for the heat flux drive term in the kinetic equation which for now is allowed to be arbitrary, and the semi-implicit operator is

$$\mathbf{L}(\Delta\mathbf{u}) = C_0 \left\{ \frac{1}{\mu_0}[\nabla\times\nabla\times(\Delta\mathbf{u}\times\mathbf{B})]\times\mathbf{B} + \mathbf{J}\times\nabla\times(\Delta\mathbf{u}\times\mathbf{B}) \right.$$
$$\left. +\nabla\left(\Delta\mathbf{u}\cdot\nabla(n_iT_i+n_eT_e) + \frac{5}{3}(n_iT_i+n_eT_e)\nabla\cdot\Delta\mathbf{u}\right)\right\} + C_1 p_{nl}\nabla^2\Delta\mathbf{u}\,, \tag{3.21}$$

where C_0 and C_1 are positive $O(1)$ coefficients, and p_{nl} is the nonlinear pressure as defined in Ref.

[1]For nonlinear problems the temperatures are first advanced in a predictor step, and then later in a corrector step where the average magnetic field over the time step is used. In these cases the Δ corresponds to the change in T_i or T_e over the relevant step (either predictor or corrector).

[36]. The algorithm for advancing the equations at time step j is summarized in Algorithm 1.

3.1.3 Explicit omission of some equilibrium quantities in the fluid equations and CEL kinetic equation

To prevent numerical noise from affecting the time evolution of the fluid-kinetic system, some equilibrium quantities (assumed to satisfy an initial zeroth order MHD force balance) are explicitly omitted from terms in Eqs. 3.15-3.20 at every time step. Specifically, in addition to the zeroth order MHD force balance being assumed to be identically satisfied for the equilibrium magnetic field, equilibrium ion and electron temperature, and equilibrium number density, it is assumed that $\mathbf{b}_{\mathrm{eq}} \cdot \nabla T_{i,\mathrm{eq}} = \mathbf{b}_{\mathrm{eq}} \cdot \nabla T_{e,\mathrm{eq}} = 0$. The equilibrium parallel temperature gradients are explicitly omitted from the diffusion terms in the temperature equations, and from the parallel temperature gradient drive term on the RHS of the kinetic equation. Especially for the parallel temperature gradient drive term on the RHS of the kinetic equation, this is found to be important in preventing numerical noise (due to the equilibrium temperatures not being perfectly flux functions) from washing out the simulation. In addition, the equilibrium contributions to the zeroth order MHD force balance relation are explicitly omitted from Eq. 3.15 at every time step.

4 BENCHMARKING NIMROD CONTINUUM KINETIC FORMULATIONS THROUGH THE STEADY STATE POLOIDAL FLOW

4.1 Motivation

Before benchmarking the full CEL approach (with evolving fluid variables and magnetic field evolution), it is prudent to first benchmark the kinetic aspects of the implementation. This allows subtle details of the kinetics to be evaluated, such as the feasibility of incorporating moments of the kinetic distortion in the kinetic equation in a fully time-implicit fashion, among others. Kinetic aspects of the CEL approach are compared herein to a previously benchmarked fixed-background δf implementation in NIMROD [44], to analytics, and to another drift kinetic code DK4D [56] which implements a similar CEL drift kinetic equation as the one in NIMROD. The comparison with analytics and DK4D also enables a further benchmarking of the fixed-background δf implementation in NIMROD.

For simplicity, the magnetic field, number density, and ion temperature are assumed to be stationary in this chapter. Because the CEL kinetic equation does not distinguish between zeroth and first order number density and temperature, this means that the number density and ion temperature are assumed stationary to all orders in the CEL kinetic equation (with $n_i = n_{i0}$ and $T_i = T_{i0}$, i.e., the number density and ion temperature are assumed to be exactly equal to the zeroth-order MHD equilibrium values). The (first order) flow is allowed to evolve in time. It is noted that a fixed-background δf approach differs in that only n_{i0} and T_{i0} are specified to be stationary in time. It is assumed that n_{i0}, T_{i0}, and ϕ_0 are flux functions. A simple quasineutral plasma of protons and electrons is also assumed. The geometry is assumed to be axisymmetric, and only the axisymmetric part of the kinetic distortion is evolved.

As previously stated (see Sec. 1.5.1), poloidal flow damping is a fundamentally kinetic process in lower collisionality regimes. Examining the poloidal flow profiles therefore provides a simple way to test the kinetic aspects of the implementation. Here, the value for the steady state ion poloidal flow coefficient

$$\alpha = -U_\theta \frac{e\left\langle B^2\right\rangle}{I(\mathrm{d}T_{i0}/\mathrm{d}\psi)}, \tag{4.1}$$

(where $U_\theta \equiv \mathbf{u}\cdot\nabla\theta/\mathbf{B}\cdot\nabla\theta$) is compared between NIMROD's continuum kinetic implementations, to analytics, and to numerical results from DK4D. It is noted that this form involving U_θ results from the neoclassical poloidal flow damping physics described previously.

Two methods for solving the CEL drift kinetic equation (DKE) in NIMROD are demonstrated

herein. They are referred to as the *DK4D approach* and the *collisional drive approach*. Along with the fixed-background δf approach, there are then three different ways of kinetically solving for the poloidal flow in NIMROD. Note, a time-implicit approach is used for all the solution methods herein (i.e., all terms in each kinetic equation are evaluated at the end of the time step).

4.2 Axisymmetric poloidal flow relations

It can be shown that the steady state U_θ is a flux function to lowest non-vanishing order (in δ), assuming $\nabla\cdot\mathbf{u}\approx 0$. A relation for U_θ can be obtained by assuming that the lowest order perpendicular flow is given by the sum of the diamagnetic and $\mathbf{E}\times\mathbf{B}$ flows, namely:

$$\mathbf{u} = \mathbf{u}_\parallel + \mathbf{u}_\perp = \frac{u_\parallel}{B}\mathbf{B} + \left(\frac{p'_{i0}}{en_{i0}} + \phi'_0\right)\left(\frac{\mathbf{B}\times\nabla\psi}{B^2}\right), \tag{4.2}$$

where subscripts of 0 refer to zeroth order (in δ) quantities, prime ($'$) signifies $\mathrm{d}/\mathrm{d}\psi$, and $u_\parallel$ is the parallel flow. Here, p_{i0} is stationary, but ϕ_0 is allowed to be time evolving (as previously mentioned in Sec. 2.3). From this, U_θ is easily found to be:

$$U_\theta = \frac{u_\parallel}{B} + \frac{I}{B^2}\left(\frac{p'_{i0}}{en_{i0}} + \phi'_0\right). \tag{4.3}$$

The poloidal flow constant α depends both on what is called the "trapped fraction",

$$f_t = 1 - \frac{3}{4}\left\langle B^2\right\rangle \int_0^{\frac{1}{B_{\max}}} \frac{\lambda \mathrm{d}\lambda}{\left\langle\sqrt{1-\lambda B}\right\rangle}, \tag{4.4}$$

where $B_{\max}$ is the maximum value for B on a given flux surface and $\lambda \equiv v_\perp^2/(v^2 B)$, and the collisionality. It is noted that the trapped fraction is a monotonically increasing function of $\tilde{\psi}$ for the equilibria used herein. There are two different analytic results for α that are used herein in the banana regime ($\nu^\star \ll 1$). Both results are obtained by initially letting [18, 19, 20]

$$f_{i1} = -\frac{Is\xi v_{Ti}}{\Omega}\left(\frac{n'_{i0}}{n_{i0}} + \frac{Z_{\mathrm{eff}} e\phi'_0}{T_{i0}} + (s^2 - 3/2)\frac{T'_{i0}}{T_{i0}}\right) f_{Mi} + g\ , \tag{4.5}$$

and expanding g in associated Laguerre polynomials $L_k^{(3/2)}(s^2)$ of order 3/2. Here, $\Omega = eB/m_i$ is the ion gyrofrequency. Putting this into the fixed-background δf drift kinetic equation (DKE) (Eq. (2.16)), and taking appropriate velocity moments, leads to a set of coupled equations for the expansion coefficients. The first of these two analytic results in the $\nu^\star \ll 1$ regime is given by Hirshman and Sigmar [18, 19]:

$$\alpha_{\text{H-S}} = \frac{-1.173}{1 + 0.462 f_t/(1 - f_t)}\,. \tag{4.6}$$

The second is a more refined analytic approach given by Taguchi [20], where the analytic treatment uses the exact pitch-angle-scattering part of the collision operator and expands the non-pitch-angle-scattering part of the collision operator up to $l = 3$ in Legendre polynomials. This differs from the Hirshman and Sigmar result, who also use the exact pitch-angle-scattering part of the collision operator, but use a model collision operator for the non-pitch-angle-scattering part (proportional to the first-order Legendre polynomial $P_1(\xi)$). Taguchi's formula for the poloidal flow coefficient is:

$$\alpha_{\text{Tag}} = \frac{-\sqrt{2}(\mu_{i2} + \Delta_{i2})}{(\mu_{i2} + \Delta_{i2})^2 - (\mu_{i1} - \Delta_{i1})(\mu_{i3} - \Delta_{i3} + \sqrt{2})}\,, \tag{4.7}$$

where

$$\begin{bmatrix} \mu_{i1} \\ \mu_{i2} \\ \mu_{i3} \end{bmatrix} = \frac{f_t}{1 - f_t} \begin{bmatrix} \sqrt{2} - \ln(1 + \sqrt{2}) \\ -2\sqrt{2} + \frac{5}{2}\ln(1 + \sqrt{2}) \\ \frac{39}{8}\sqrt{2} - \frac{25}{4}\ln(1 + \sqrt{2}) \end{bmatrix} \approx \frac{f_t}{1 - f_t} \begin{bmatrix} 0.533 \\ -0.625 \\ 1.386 \end{bmatrix}\,, \tag{4.8}$$

are the standard neoclassical viscosity coefficients, and the Δ_{ik} $(k = 1, 2, 3)$ are given by

$$\begin{bmatrix} \Delta_{i1} \\ \Delta_{i2} \\ \Delta_{i3} \end{bmatrix} = \frac{7}{3}\left(F_t \tilde{f}_c + \tilde{f}_t \bar{f}_t\right) \begin{bmatrix} -\frac{1087}{63}\sqrt{2} + \frac{589}{21}\ln(1 + \sqrt{2}) \\ -\frac{143}{126}\sqrt{2} + \frac{55}{21}\ln(1 + \sqrt{2}) \\ \frac{50923}{504}\sqrt{2} - \frac{13625}{84}\ln(1 + \sqrt{2}) \end{bmatrix} \approx \frac{7}{3}\left(F_t \tilde{f}_c + \tilde{f}_t \bar{f}_t\right) \begin{bmatrix} 0.320 \\ 0.703 \\ -0.072 \end{bmatrix}\,, \tag{4.9}$$

where $F_t = 1 - \langle B^3\rangle^2/(\langle B^4\rangle\langle B^2\rangle)$, $\tilde{f}_t = 1 - \tilde{f}_c$, $\overline{f}_t = \tilde{f}_t + F_t\tilde{f}_c$, and

$$\tilde{f}_c = \frac{15}{16}\frac{1}{f_c}\frac{\langle B^4\rangle\langle B^2\rangle}{\langle B^3\rangle}\int_0^{\frac{1}{B_{\max}}}\frac{\lambda^2 \mathrm{d}\lambda}{\left\langle\sqrt{1-\lambda B}\right\rangle}\,, \tag{4.10}$$

where $f_c = 1 - f_t$.

4.3 Kinetic formulations

4.3.1 Specification for ϕ_0' in the fixed-background δf approach

The fixed-background δf approach requires a specification for the zeroth-order electrostatic potential (see Eq. (2.16)). As is subsequently shown though, the choice for ϕ_0' does not affect the result for the steady-state poloidal flow. It will, however, affect the general flow dynamics, thus the need for a specification for ϕ_0'. Although it is not needed for the results herein, the specification method that would be used for general calculations in the fixed-background δf approach is briefly summarized here. For the purposes herein, an approach that doesn't require coupling to an electron evolution equation is sought.

Dotting $R\hat{\boldsymbol{\phi}}$ into Eq. (3.1), omitting the higher-order advective term, and flux-surface averaging, gives:

$$m_i n_{i0}\frac{\partial\left\langle Ru_\phi\right\rangle}{\partial t} \approx 0\,. \tag{4.11}$$

Eq. (4.11) is similar to the result used in Refs. 69 and 24, but therein the authors used simply that

$$\frac{\partial u_\phi}{\partial t} = 0\,.$$

Dotting $R\hat{\phi}$ into Eq. (4.2), and then flux-surface averaging, the following is obtained:

$$\left\langle Ru_\phi\right\rangle = I\left\langle\frac{u_\parallel}{B}\right\rangle - I^2\left\langle\frac{B_\theta^2}{B^2B_\phi^2}\right\rangle\left(\frac{p_{i0}'}{en_{i0}} + \phi_0'\right)\,, \tag{4.12}$$

where $B_\theta \equiv \mathbf{B}\cdot\nabla\theta/|\nabla\theta|$. Choosing $\left\langle Ru_\phi\right\rangle$ is equivalent to choosing the initial perpendicular flow. A simple choice is $\left\langle Ru_\phi\right\rangle = I\left\langle u_\parallel/B\right\rangle_{t=0}$, which is equivalent to specifying that the initial

perpendicular flow is zero. With this choice, the following is obtained:

$$\phi_0' = \frac{\left\langle \frac{u_\parallel}{B} \right\rangle - \left\langle \frac{u_\parallel}{B} \right\rangle_{t=0}}{I \left\langle \frac{B_\theta^2}{B^2 B_\phi^2} \right\rangle} - \frac{p_{i0}'}{e n_{i0}} \,. \tag{4.13}$$

A specification for ϕ_0' has now been obtained to use in Eq. (2.16).

4.3.2 Solution methodology for the fixed-background δf approach

To obtain the parallel ion flow from f_{i1}, the following formula is used:

$$u_\parallel = \frac{1}{n_{i0}} \int \mathrm{d}^3 v v_\parallel f_{i1} = \frac{2\pi v_{Ti0}^4}{n_{i0}} \int_0^\infty \mathrm{d}s s^3 \int_{-1}^1 \mathrm{d}\xi P_1(\xi) f_{i1} \,. \tag{4.14}$$

This equation is nothing more than the definition of the appropriate moment needed to obtain the parallel flow.

To get $U_{i\theta}$ from the ion distribution function, it is shown that the specification of ϕ_0' does not affect the result for the steady-state poloidal flow. First, Eq. (4.5) is substituted into Eq. (4.14). From Eq. (4.3), one can see that only g will contribute to the poloidal flow. Then, upon substituting the ansatz (Eq. (4.5)) into the steady-state version of Eq. (2.16), it is found that ϕ_0' cancels out of the equation. So the steady-state equation for g does not depend on ϕ_0', and therefore the steady-state poloidal flow does not depend on the specification of ϕ_0'. For convenience, $\phi_0' = -p_{i0}'/(e n_{i0})$ is used herein (i.e., having the $\mathbf{E} \times \mathbf{B}$ flow exactly cancel the diamagnetic flow). Using Eq. (4.3), this then immediately gives that $U_\theta = u_\parallel / B$, which indicates how to get U_θ from f_{i1}. Note, this formula for U_θ only applies because of the choice of ϕ_0'. Once U_θ is obtained, α is easily obtained from Eq. (4.1).

4.3.3 Simplified CEL-DKE

Assuming an axisymmetric configuration, and that n_{i0} and T_{i0} are stationary flux functions, the CEL-DKE for the ions (Eq. (2.7) with $D_{f_{i1}} = 0$) simplifies to:

$$\begin{aligned}
&\frac{\partial f_{i1}}{\partial t} + \xi s v_{Ti0}\mathbf{b}\cdot\nabla f_{i1} - \frac{1-\xi^2}{2\xi}\left[\xi s v_{Ti0}\mathbf{b}\cdot\nabla \ln B\right]\frac{\partial f_{i1}}{\partial \xi} - C\left(f_{i1}\right) \\
&= \Bigg\{ \frac{\xi s v_{Ti0}}{n_{i0}T_{i0}}\left[\frac{2}{3}\mathbf{b}\cdot\nabla\pi_{i\|} - \pi_{i\|}\mathbf{b}\cdot\nabla\ln B\right] \\
&\quad + P_2(\xi)\frac{2}{3}s^2\left(\nabla\cdot\mathbf{u}_i - 3\mathbf{b}\cdot\left[\mathbf{b}\cdot\nabla\mathbf{u}_i\right]\right) \\
&\quad + \frac{2}{3n_{i0}T_{i0}}\left(s^2 - \frac{3}{2}\right)\nabla\cdot\left(q_{i\|}\mathbf{b}\right) \\
&\quad + \frac{I}{3eB}\Bigg[\frac{1}{2}P_2\left(\xi\right)2s^2\left(2s^2-5\right) \\
&\qquad\qquad + 4s^4 - 20s^2 + 15\Bigg]\mathbf{b}\cdot\nabla\ln B\frac{dT_{i0}}{d\psi}\Bigg\} f_{Mi0}\,,
\end{aligned} \tag{4.15}$$

Further simplification occurs by assuming that the ion flow equals the neoclassical value, $\mathbf{u}_i = U_\theta\mathbf{B} - R^2\nabla\phi\left(p'_{i0}/(en_{i0}) + \phi'_0\right)$, and that the ion parallel heat flux equals the Pfirsch–Schluter-like return component, $\nabla\cdot\left(q_{i\|}\mathbf{b}\right) = -\nabla\cdot\left(\frac{5n_{i0}T_{i0}}{2eB}\mathbf{b}\times\nabla T_{i0}\right)$. The heat flux assumption is required for consistency when not evolving the temperature [56] (see Eq. (3.3) with $\nabla\cdot\mathbf{u} = 0$, $\mathbf{u}\cdot\nabla T_i = 0$, and $D_{T_i} = 0$). With these two assumptions, the CEL-DKE becomes:

$$\begin{aligned}
&\frac{\partial f_{i1}}{\partial t} + \xi s v_{Ti0}\mathbf{b}\cdot\nabla f_{i1} - \frac{1-\xi^2}{2\xi}\left[\xi s v_{Ti0}\mathbf{b}\cdot\nabla \ln B\right]\frac{\partial f_{i1}}{\partial \xi} - C\left(f_{i1}\right) \\
&= \Bigg\{ \frac{\xi s v_{Ti0}}{n_{i0}T_{i0}}\left[\frac{2}{3}\mathbf{b}\cdot\nabla\pi_{i\|} - \pi_{i\|}\mathbf{b}\cdot\nabla\ln B\right] \\
&\quad - 2P_2\left(\xi\right)s^2 U_\theta\mathbf{b}\cdot\nabla B \\
&\quad + \frac{2I}{3eB}\left[\left(P_2\left(\xi\right)+2\right)s^2\left(s^2 - \frac{5}{2}\right)\right]\mathbf{b}\cdot\nabla\ln B\frac{dT_{i0}}{d\psi}\Bigg\} f_{Mi0}\,.
\end{aligned} \tag{4.16}$$

4.3.4 Solution methodology I for CEL-DKE – the DK4D approach

For this solution approach, the method is followed that is used in the DK4D code [56]. Because Eq. (4.16) is linear, it can be solved separately for each of the two non-moment drive terms. The sum satisfies Eq. (4.16) and can be written

$$f_{i1} = f_{i1,U_\theta} + f_{i1,T'_{i0}} = g_{U_\theta} U_\theta + g_{T'_{i0}} (IT'_{i0}/e) \ , \tag{4.17}$$

where f_{i1,U_θ} is the solution with only the U_θ drive term in Eq. (4.16), and $f_{i1,T'_{i0}}$ is the solution with only the T'_{i0} drive term in Eq. (4.16). For convenience, $g_{U_\theta} \equiv f_{i1,U_\theta}/U_\theta$, and $g_{T'_{i0}} \equiv f_{i1,T'_{i0}}/(IT'_{i0}/e)$ are defined. Two versions of Eq. (4.16), one for each of the non-moment drives on the right-hand side, are evolved in time, namely:

$$\begin{aligned} \mathcal{L}\left(g_{U_\theta}\right) = & \left\{ \frac{\xi s v_{Ti0}}{n_{i0} T_{i0}} \left[\frac{2}{3} \mathbf{b} \cdot \nabla \, \pi_{i\|}\Big|_{g_{U_\theta}} - \pi_{i\|}\Big|_{g_{U_\theta}} \mathbf{b} \cdot \nabla \ln B \right] \right. \\ & \left. - 2 P_2\left(\xi\right) s^2 \mathbf{b} \cdot \nabla B \right\} f_{Mi0} \end{aligned} \tag{4.18}$$

for g_{U_θ}, where $\mathcal{L}$ represents the linear operator on the LHS of Eq. (4.16) and

$$\pi_{i\|}\Big|_{g_{U_\theta}} = 2\pi m_i v_{Ti0}^5 \int_0^\infty \mathrm{d}s s^4 \int_{-1}^1 \mathrm{d}\xi P_2(\xi) g_{U_\theta} \ , \tag{4.19}$$

and

$$\begin{aligned} \mathcal{L}\left(g_{T'_{i0}}\right) = & \left\{ \frac{\xi s v_{Ti0}}{n_{i0} T_{i0}} \left[\frac{2}{3} \mathbf{b} \cdot \nabla \pi_{i\|}\Big|_{g_{T'_{i0}}} - \pi_{i\|}\Big|_{g_{T'_{i0}}} \mathbf{b} \cdot \nabla \ln B \right] \right. \\ & \left. + \frac{2}{3B} \left[\left(P_2\left(\xi\right) + 2\right) s^2 \left(s^2 - \frac{5}{2} \right) \right] \mathbf{b} \cdot \nabla \ln B \right\} f_{Mi0} \end{aligned} \tag{4.20}$$

for $g_{T'_{i0}}$, where

$$\pi_{i\|}\Big|_{g_{T'_{i0}}} = 2\pi m_i v_{Ti0}^5 \int_0^\infty \mathrm{d}s s^4 \int_{-1}^1 \mathrm{d}\xi P_2(\xi) g_{T_{i0}\prime} \ . \tag{4.21}$$

The full solution to Eq. (4.16) is then given by Eq. (4.17). Then using the fact that $\left\langle \pi_{i\|}\mathbf{b}\cdot\nabla B\right\rangle = 0$ in the steady state, and evaluating the $\pi_{i\|}$ moment with the full f_{i1} from Eq. (4.17), the following is obtained:

$$U_\theta \left\langle \pi_{i\|}\big|_{g_{U_{i\theta}}} \mathbf{b}\cdot\nabla B\right\rangle + (IT'_{i0}/e)\left\langle \pi_{i\|}\big|_{g_{T'_{i0}}} \mathbf{b}\cdot\nabla B\right\rangle = 0\,. \tag{4.22}$$

This then gives U_θ as

$$U_\theta = \frac{-(IT'_{i0}/e)\left\langle \pi_{i\|}\big|_{g_{T'_{i0}}} \mathbf{b}\cdot\nabla B\right\rangle}{\left\langle \pi_{i\|}\big|_{g_{U_\theta}} \mathbf{b}\cdot\nabla B\right\rangle}\,, \tag{4.23}$$

and α is immediately found from Eq. (4.1). As can be seen from Eqs. (4.19), (4.21) and (4.23) this method uses a ratio of appropriate $P_2(\xi)$ velocity moments of the solution, which provides a contrast with the next approach which will ultimately use an appropriate $P_1(\xi)$ velocity moment of the solution.

4.3.5 Solution methodology II for CEL-DKE – the collisional drive approach

There is a second solution methodology that can be used to find the steady-state U_θ from the CEL-DKE. This approach involves the particular solution to the steady-state version of Eq. (4.16). When neglecting collisions, the particular solution is [23]:

$$\begin{aligned} f_{i1,p} = \Bigg[\frac{1}{n_{i0}T_{i0}}\int \mathrm{d}l_\| \left(\frac{2}{3}\mathbf{b}\cdot\nabla\pi_{i\|} - \pi_{i\|}\mathbf{b}\cdot\nabla\ln B\right) - \Bigg(\frac{m_i U_\theta B}{T_{i0}} \\ + \frac{m_i I}{eBT_{i0}}\left(s^2 - \frac{5}{2}\right)T'_{i0}\Bigg)\xi s v_{Ti0}\Bigg] f_{Mi0}\,, \end{aligned} \tag{4.24}$$

where $l_\|$ is length along the magnetic field. The full solution is then defined as $f_{i1} = f_{i1,p} + h_i$. Putting this into Eq. (4.16), an equation for h_i is obtained:

$$\xi s v_{Ti0}\mathbf{b}\cdot\nabla h_i - \frac{1-\xi^2}{2\xi}[\xi s v_{Ti0}\mathbf{b}\cdot\nabla \ln B]\frac{\partial h_i}{\partial \xi} - C\left(h_i\right)$$
$$= \left(\nu_{ii}2^{3/2}\right)\frac{2^{1/2}}{s^2 v_{Ti0}}\frac{IT'_{i0}}{eB}\xi\Bigg[\left(2s^2-5\right)\phi_{\mathrm{err}}\left(s\right) + 5s\frac{d\phi_{\mathrm{err}}\left(s\right)}{ds}\Bigg] f_{Mi0}\ . \tag{4.25}$$

Solving for h_i and using the fact that $\int \mathrm{d}^3 v \mathbf{v} f_{i1} = 0$ for the CEL approach leads to:

$$U_\theta = \frac{1}{n_{i0}B}\int \mathrm{d}^3 v \xi s v_{Ti0} h_i\ , \tag{4.26}$$

and again α is easily obtained from Eq. (4.1). An interesting observation is that the moment required to obtain $U_{i\theta}$ from the solution here is identical to the moment required in the fixed-background δf approach, although the drive terms are different.

To summarize, in the interest of vetting the kinetic aspects of the fixed-background δf and CEL implementations in NIMROD, three different methods for obtaining α have been represented. With the fixed-background δf implementation, α is obtained through the parallel flow moment of f_{i1}. With the CEL implementation, α is obtained through either the DK4D approach, or the collisional drive approach. The DK4D approach involves a ratio of quantities that depend on the $P_2(\xi)$ moments of $g_{U_{i\theta}}$ and $g_{T_i'}$, and the collisional drive approach involves a parallel flow moment of h_i. The DK4D and collisional drive approaches ultimately differ in how f_{i1} is decomposed, resulting in different kinetic equations (requiring different solution methods) for the unspecified parts of the decomposition in each approach.

4.3.6 Modified definition of the ion-ion Coulomb logarithm for comparison with DK4D

It is noted here that the exact definition of the ion-ion Coulomb logarithm does make a significant difference when running in higher collisionality regimes. To be consistent with DK4D, the same definition is used, namely,

$$\ln(\Lambda_{ii}) = \ln\left(\frac{\sqrt{\epsilon_0 T_{i0}/(n_{i0}e^2)}}{e^2/(\pi\epsilon_0 m_i v_{Ti0}^2)}\right)\ , \tag{4.27}$$

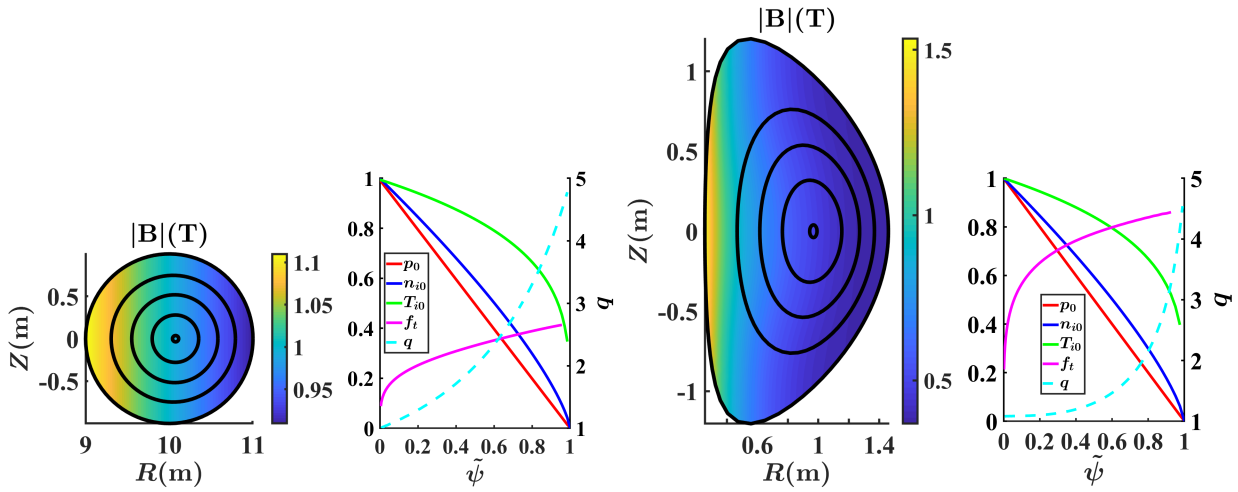

Figure 4.1: Both a high aspect ratio (a) and an NSTX (b) equilibrium are used. The on axis value for the equilibrium total pressure (p_0) is $\sim 8.0 \times 10^2$ Pa in (a) and $\sim 2.3 \times 10^4$ Pa in (b). In each subfigure, the normalized profiles, safety factor, and f_t are shown at the right, and flux surfaces and $|\mathbf{B}|$ contours are shown at the left. Note the high $|\mathbf{B}|$ variation and high f_t for the NSTX equilibrium.

which differs from that in Ref. 19 by a factor of 2 inside the logarithm. Eq. (4.27) differs from the NRL plasma formulary definition (see Eq. (1.9)) by as much as 7% for the higher collisionality ($\hat{\nu} \sim 1$) equilibria used herein. This led to $\sim 5\%$ or greater differences in the results for α. Eq. (1.9) is more typically used in NIMROD continuum kinetic calculations.

4.4 Equilibria details

For this verification exercise, the same two JSOLVER [70] Grad-Shafranov equilibria studied in Ref. 56 are used. The first is a high aspect ratio equilibrium with $\epsilon = 0.1$ (see Fig. 4.1a), and the second is an NSTX equilibrium (see Fig. 4.1b). The high aspect ratio equilibrium easily enables comparison with analytics, whereas the NSTX equilibrium is a more realistic equilibrium with high $|\mathbf{B}|$ variation and high f_t. The ion number density is specified to have the profile $n_{i0} = n_{\text{axis}}(1 - \tilde{\psi})^{0.75}$. For each equilibrium, the ion number density profile (parametrized by n_{axis}) is varied to explore different collisionality regimes, leaving p_{i0}, and hence the Grad-Shafranov force balance, fixed. Values of n_{axis} are chosen for both equilibria to enable comparison with the results in Ref. [56].

4.5 Necessity of an exact trapped-passing grid for convergence in the banana regime

Figs. 4.2, and 4.3 show that for a similar number of degrees of freedom (dof) in ξ, at $\nu^\star \sim 10^{-2}$, convergence in the result for the poloidal flow coefficient α is obtained for the exact tpb FE grid in ξ, but not when using Legendre polynomials over the entire domain of $-1 \leq \xi \leq 1$. Physically, this

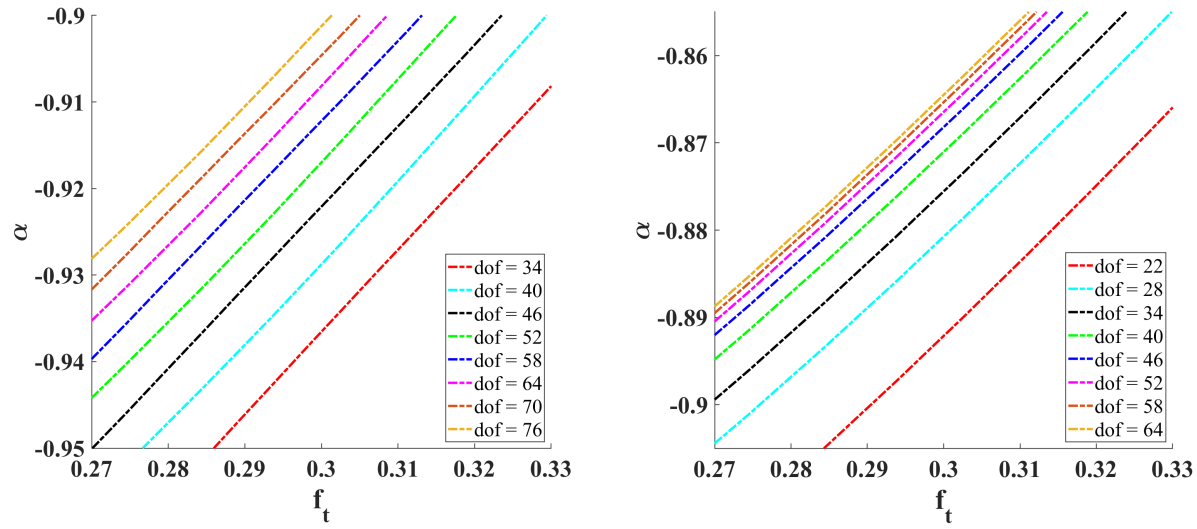

(a) Legendre polynomials in ξ.

(b) Exact tpb FE grid in ξ, GLL polynomials.

Figure 4.2: Convergence in α, for the high aspect ratio ($\epsilon = 0.1$) case with $n_{\text{axis}} = 5.0 \times 10^{17} m^{-3}$, ($\nu^\star \sim 10^{-2}$). As can be seen on the left (a), 75 degrees of freedom (dof) in ξ is still insufficient for convergence in α when using Legendre polynomials. On the right (b), it can be seen that convergence in α is essentially obtained at only 58 dof in ξ when using the exact tpb FE grid.

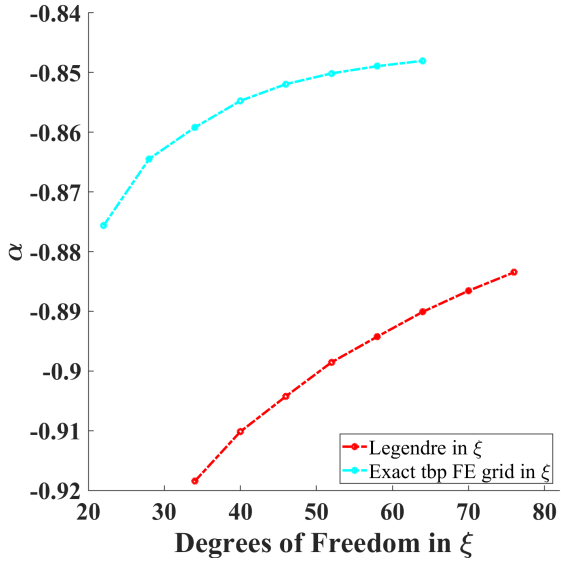

Figure 4.3: The superior convergence of the exact tpb FE grid is shown above for the high aspect ratio case ($\epsilon = 0.1$) with $\nu^\star \sim 10^{-2}$. Data taken from Fig. 4.2 at $f_t \approx 0.32$.

phenomena is due to the development of a discontinuity in the ξ derivative of f_{i1} in the steady-state banana regime solution at the tpb [18] (see Fig. 4.4). It is noted here that many drift kinetic codes, including DK4D [56], NEO [71], and CQL3D [67], use a Legendre polynomial expansion for their pitch angle variable.

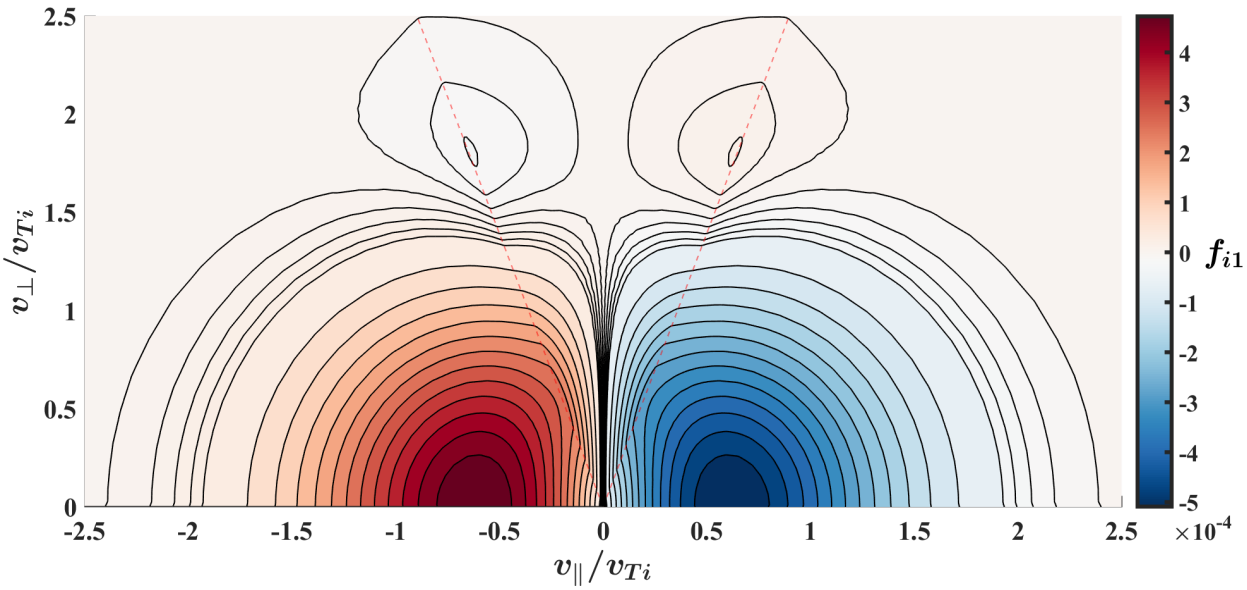

Figure 4.4: A contour plot of the steady-state f_{i1} in velocity space at $R \approx 10.67$, $Z = 0.0$ using the high aspect ratio equilibrium ($\nu^\star \sim 10^{-4}$). Sharp variation in $\partial f_{i1}/\partial \xi$ at the tpb (shown in red) is easily resolved by the exact tpb FE grid with GLL polynomials.

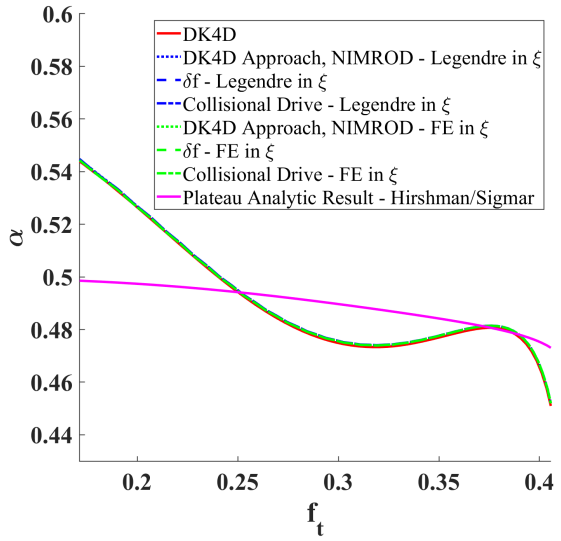

Figure 4.5: α profiles for the high aspect ratio case with $\hat{\nu} \sim 1$ show excellent agreement between all of NIMROD's numerical approaches and DK4D. The analytic result shown is the plateau regime result from Hirshman and Sigmar [18].

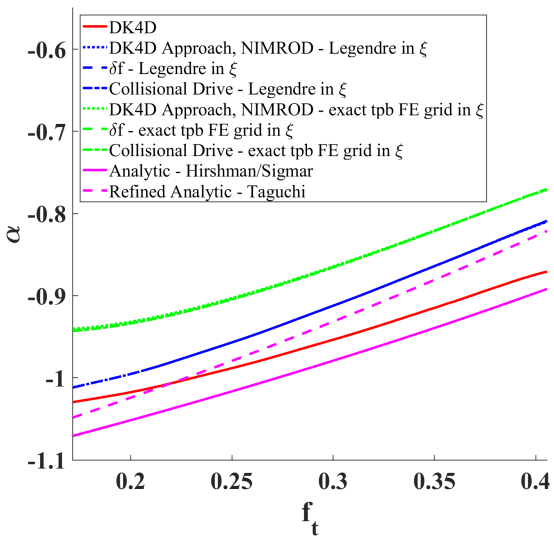

Figure 4.6: α profiles for the high aspect ratio case with $\hat{\nu} \sim 10^{-4}$. Here, Legendre polynomial cases in NIMROD use a maximum degree of 57, as in DK4D. All NIMROD exact tpb FE curves (green) agree between each other, as well as all NIMROD Legendre curves (blue). Analytic (magenta), and DK4D (red) curves are also shown.

4.6 Numerical results and discussion

Here numerical results for α are shown and compared with analytics, and to results from DK4D [56]. As a reminder, in NIMROD, α can be calculated using either the DK4D approach, the collisional drive approach, or the fixed-background δf approach. Each of these approaches can use various methods of numerical expansion for ξ, as stated in Section 3.1.1. For the results herein, two of these methods are compared: an exact tpb FE grid with GLL basis polynomials, and Legendre polynomials over $-1 \leq \xi \leq 1$. Figs. 4.5 and 4.6 show the α profiles for the high aspect ratio equilibrium at both a higher collisionality ($\hat{\nu} \sim 1$, $n_{\text{axis}} = 1.0 \times 10^{19}\ m^{-3}$), and a banana regime collisionality ($\hat{\nu} \sim 10^{-4}$, $n_{\text{axis}} = 5.0 \times 10^{17}\ m^{-3}$), respectively. Figs. 4.7 and 4.8 show the α profiles for the NSTX equilibrium at both a higher collisionality ($\hat{\nu} \sim 1$, $n_{\text{axis}} = 2.0 \times 10^{20}\ m^{-3}$), and a banana regime collisionality ($\hat{\nu} \sim 10^{-4}$, $n_{\text{axis}} = 1.0 \times 10^{19}\ m^{-3}$), respectively. α vs. f_t is plotted, where f_t is a flux label for the equilibria used herein (see Fig. 4.1).

As can be seen from Figs. 4.5 and 4.7, excellent agreement is obtained between all of NIMROD's approaches and DK4D in the regime of higher collisionality ($\hat{\nu} \sim 1$). At higher collisionality, details of the collision operator are paramount, and so the high level of agreement in this regime is a promising result. In Fig. 4.5, the plateau regime analytic result from Ref. 18 is also shown. Differences can be seen between the numerical results and the plateau analytic result. However the analytic result uses a model collision operator, as well as other approximations [18]. In addition, at a $\hat{\nu}$ of about 1, the collisionality is at the edge of the plateau regime, rather than squarely inside it. The fact then that the analytic result is as close to the numerical results as it is (within about 8%) is encouraging.

In Figs. 4.6 and 4.8, all of NIMROD's global Legendre in ξ results agree with each other, and all of NIMROD's FE in ξ results agree with each other. Some discrepancies between NIMROD's approaches, analytics, and DK4D are also seen. However, it is again noted here that the Legendre polynomial in ξ cases are not converged at this low collisionality. Obtaining convergence in the banana collisionality regime is difficult with a global Legendre in ξ basis, as was shown in Fig. 4.2a. This occurs because of the discontinuity of the ξ derivative of f_{i1} at the tpb. For these cases, the same maximum Legendre degree as DK4D was used, to enable comparison. Through looking at the simulations (see Fig. 4.3), there is reason to believe that with increasing Legendre degree, NIMROD's Legendre in ξ results will agree with the exact tpb FE results. However, at the high Legendre degree required for convergence in ξ, memory requirements impose constraints which make these runs too computationally expensive to continue further.

It is also noted that NIMROD's DK4D approach results in Figs. 4.6 and 4.8 required introducing a small amount of ad-hoc diffusion into Eqs. (4.18) and (4.20) to enable a numerically-stable evolution to steady state. Specifically, $D_{\text{ad-hoc}}\nabla^2 g_{U_\theta}$ was added to the RHS of Eq. (4.18) and

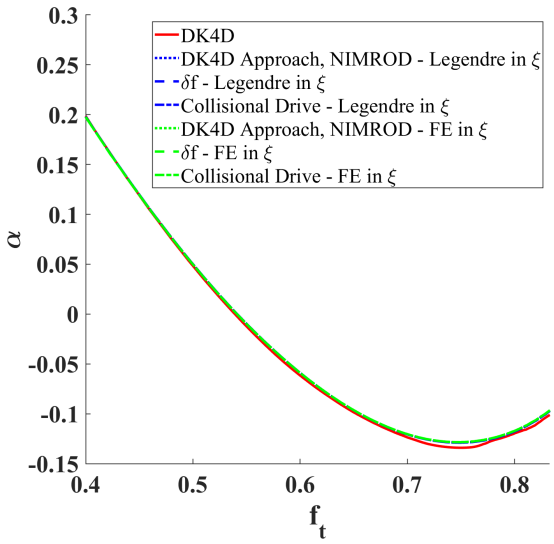

Figure 4.7: α profiles for the NSTX case with $\hat{\nu} \sim 1$ show excellent agreement between all of NIMROD's numerical approaches and DK4D.

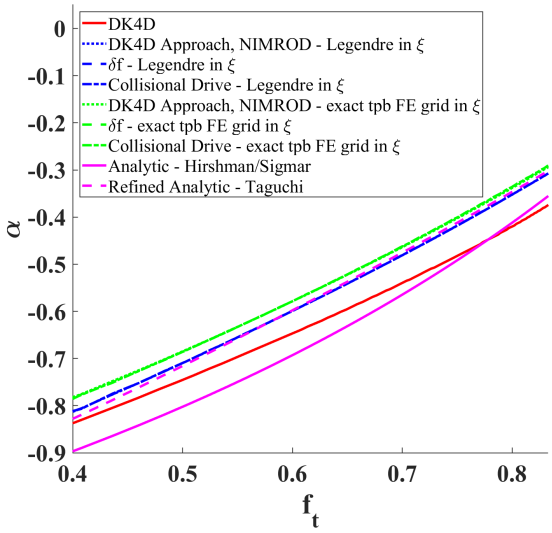

Figure 4.8: α profiles for the NSTX case with $\hat{\nu} \sim 10^{-4}$. Here, Legendre polynomial cases in NIMROD use a maximum degree of 73, as in DK4D. All NIMROD exact tpb FE curves (green) agree between each other, as well as all NIMROD Legendre curves (blue). Analytic (magenta), and DK4D (red) curves are also shown.

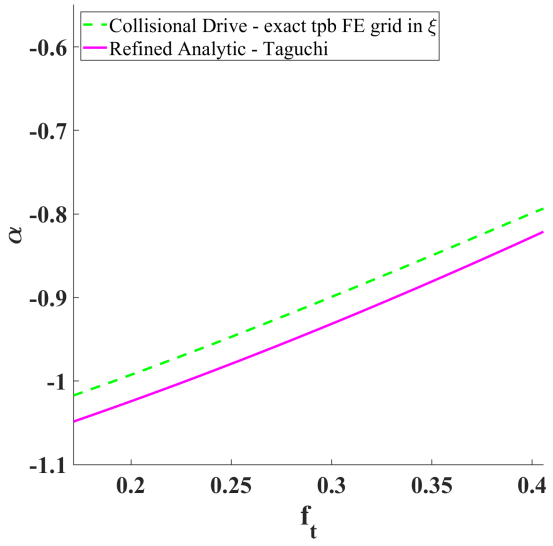

(a) High aspect ratio ($\nu^\star \sim 10^{-4}$).

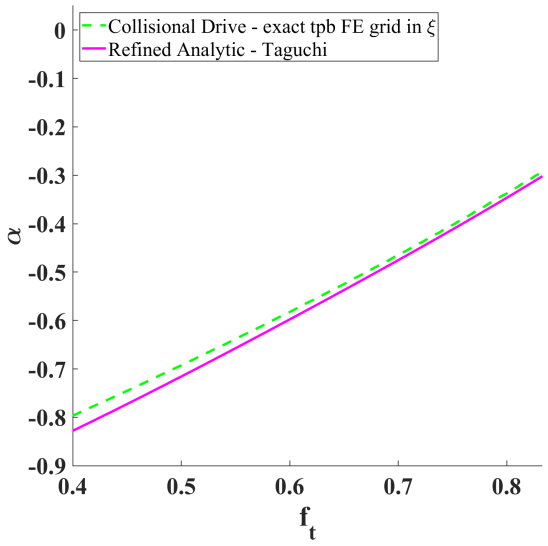

(b) NSTX ($\nu^\star \sim 10^{-4}$).

Figure 4.9: Comparison of α profiles for $\nu^\star \sim 10^{-4}$, with Taguchi's [20] analytic formula. Here an exact tpb FE grid in ξ with GLL polynomials is used, and the profiles agree within 5%.

$D_{\text{ad-hoc}}\nabla^2 g_{T'_{i0}}$ was added to the RHS of Eq. (4.20), with $D_{\text{ad-hoc}}$ a constant diffusivity. These results were verified to be converged in $D_{\text{ad-hoc}}$. They are therefore negligibly affected by the inclusion of the ad-hoc diffusion terms.

For the banana regime collisionality results, the analytics are also seen to differ from the numerics, both for NIMROD and DK4D. This disagreement is partly due to the fact that the results are not completely in the deep banana regime. A $\hat{\nu} \sim 10^{-4}$ translates to $\nu^{\star} \sim 10^{-2}$ for the high aspect ratio case and $\nu^{\star} \sim 10^{-3}$ for the NSTX case. It has been observed that a $\nu^{\star}$ of about 10^{-4} is required to be in the asymptotic regime where the analytics are valid. It is also noted that Taguchi's refined analytic result [20], which goes to a higher Legendre expansion of the non-pitch-angle-scattering part of the collision operator, gives better agreement with these results than the Hirshman/Sigmar analytic formulation. This shows that getting the collision operator right in an analytic formulation is important, even in the banana regime where collisions at the tpb remain important.

For an additional comparison, the steady state α was computed at $\nu^{\star} \sim 10^{-4}$ for both the high aspect ratio and NSTX equilibrium. These results for α (where the exact tpb FE grid in ξ is used) are compared to Taguchi's analytic formulation in Fig. 4.9. Here it is seen that when using the converged results (both in resolution and $\nu^{\star}$) and Taguchi's refined analytic formula, the difference is reduced to less than 5%. This last discrepancy might well be resolved by refining the analytic formulation even further.

4.7 Summary

Several NIMROD continuum kinetic formulations have been successfully verified and benchmarked herein. The results for the poloidal flow coefficient α were compared between the different NIMROD formulations, analytics, and DK4D in various collisionality regimes. Results agree very well between the approaches in the higher collisionality regime ($\hat{\nu} \sim 1$). In the banana collisionality regime ($\hat{\nu} \sim 10^{-4}$) the results differ. However, it was noted that the Legendre results are not converged in the banana regime, a familiar problem in banana regime drift kinetics. A C^0 finite element numerical grid with cell boundaries that follow the exact trapped-passing boundary was shown to allow numerical convergence in the banana regime. It is also seen that going to a refined analytic formulation for α – namely, using the Taguchi formula – further reduces the discrepancy between NIMROD's numerical results and analytics to less than 5%.

The agreement of the results in the higher collisionality regime also indicate that NIMROD's general implementation of the collision operator, which allows for several basis sets in 2D velocity space, most notably the exact FE tpb grids, is accurate and efficient. Further verification of the collision operator implementation may be found in Ref. 46.

5 A NUMERICAL STABILITY ANALYSIS OF THE CEL CLOSURE APPROACH ALGORITHM IN NIMROD

Here, a von Neumann linear stability analysis of the full coupled fluid-kinetic system is performed to help elucidate methods that make the time advance of the full system (Eqs. (3.15)-(3.21)) numerically stable. The linear analysis is performed in the same vein as Section 3.1 of Ref. [68], but with additions appropriate for an added kinetic equation in the system. Small perturbations to homogeneous (in physical space) and time-independent equilibrium variables is assumed, and all perturbed quantities are Fourier transformed (with k the wavenumber and the wavevector $\mathbf{k} = k\hat{\mathbf{k}}$). It is also assumed, for simplicity, that all perturbations vary in the Cartesian $\hat{\mathbf{y}}$ direction (i.e., $\hat{\mathbf{k}} = \hat{\mathbf{y}}$), and that the background magnetic field is in the y-z plane (i.e., $\mathbf{B}_0 = B_0(cs\hat{\mathbf{y}} + sn\hat{\mathbf{z}})$). The time centerings given in Sec. 3.1.2 are assumed, with some exceptions (as specified below). The equilibrium flow ($\mathbf{u}_0$) in the $\hat{\mathbf{k}}$ direction is set to $1.82 \times 10^{-4}\ v_A$, where v_A is the Alfvén velocity ($v_A = B_0/\sqrt{\mu_0 m_i n_{i0}}$). All ad-hoc diffusion parameters are set to zero ($D_u = D_n = D_{T_i} = D_{f_{i1}} = 0$) so as to find, if possible, numerical stability criteria that do not rely on ad-hoc diffusion parameters. $\kappa_{e,\parallel}$ is set to zero to avoid relying on that parameter to achieve numerical stability. The simplifying assumption is made that $\kappa_{e,\perp} = 0$, and that the resistivity, η, is a constant. Finally it is assumed that the equilibrium f_{i1} is zero, which is equivalent to specifying that the equilibrium background distribution function is a Maxwellian.

With these assumptions, and letting some centering parameters now become arbitrary, Eqs. (3.15)-(3.21) become:

$$m_i n_{i0}\left(\frac{\Delta u_{1kx}}{\Delta t} + \frac{1}{2}\mathbf{u}_0 \cdot \hat{\mathbf{k}} ik \Delta u_{1kx}\right) - \Delta t C_0(-k^2)\left(\frac{B_0^2}{\mu_0}(cs)^2 \Delta u_{1kx}\right) = -m_i n_{i0}\mathbf{u}_0 \cdot \hat{\mathbf{k}} ik u_{1kx}^j + \frac{B_0}{\mu_0} ik(cs) B_{1kx}^{j+1/2}\,, \tag{5.1}$$

$$m_i n_{i0}\left(\frac{\Delta u_{1ky}}{\Delta t}+\frac{1}{2}\mathbf{u}_0\cdot\hat{\mathbf{k}}ik\Delta u_{1ky}\right)-\Delta t C_0(-k^2)\left(\frac{B_0^2}{\mu_0}\left(-(cs)(sn)\Delta u_{1kz}+(sn)^2\Delta u_{1ky}\right)\right.$$
$$\left.+\frac{5}{3}\left(n_{i0}T_{i0}+n_{e0}T_{e0}\right)\Delta u_{1ky}\right)=-m_i n_{i0}\mathbf{u}_0\cdot\hat{\mathbf{k}}iku^j_{1ky}-\frac{B_0}{\mu_0}ik(sn)B^{j+1/2}_{1kz}$$
$$-ik\left(n_{i0}T^{j+1/2}_{i1k}+T_{i0}n^{j+1/2}_{i1k}+n_{e0}T^{j+1/2}_{e1k}+T_{e0}n^{j+1/2}_{e1k}\right)+\frac{1}{3}ik\pi_{i\|}((f^*_{i1})_{1k},T_{i0})$$
$$-(cs)^2ik\pi_{i\|}((f^*_{i1})_{1k},T_{i0})\,, \tag{5.2}$$

$$m_i n_{i0}\left(\frac{\Delta u_{1kz}}{\Delta t}+\frac{1}{2}\mathbf{u}_0\cdot\hat{\mathbf{k}}ik\Delta u_{1kz}\right)-\Delta t C_0(-k^2)\left(\frac{B_0^2}{\mu_0}\left((cs)^2\Delta u_{1kz}-(cs)(sn)\Delta u_{1ky}\right)\right)$$
$$=-m_i n_{i0}\mathbf{u}_0\cdot\hat{\mathbf{k}}iku^j_{1kz}+\frac{B_0}{\mu_0}ik(cs)B^{j+1/2}_{1kz}-(cs)(sn)ik\pi_{i\|}((f^*_{i1})_{1k},T_{i0})\,, \tag{5.3}$$

$$\frac{\Delta n_{e1k}}{\Delta t}+\frac{1}{2}(\mathbf{u}_0\cdot\hat{\mathbf{k}})ik\Delta n_{e1k}=-(\mathbf{u}_0\cdot\hat{\mathbf{k}})ikn^{j+1/2}_{e1k}-n_{e0}iku^{j+1}_{1ky}\,, \tag{5.4}$$

$$\frac{3}{2}n_{i0}\left(\frac{\Delta T_{i1k}}{\Delta t}+\frac{1}{2}(\mathbf{u}_0\cdot\hat{\mathbf{k}})ik\Delta T_{i1k}\right)=-\frac{3}{2}n_{i0}(\mathbf{u}_0\cdot\hat{\mathbf{k}})ikT^{j+1/2}_{i1k}-n_{i0}T_{i0}iku^{j+1}_{1ky}$$
$$-ik(cs)q_{i\|}((f^{**}_{i1})_{1k},T_{i0})\,, \tag{5.5}$$

$$\frac{3}{2}n_{e0}\left(\frac{\Delta T_{e1k}}{\Delta t}+\frac{1}{2}(\mathbf{u}_0\cdot\hat{\mathbf{k}})ik\Delta T_{e1k}\right)=-\frac{3}{2}n_{e0}(\mathbf{u}_0\cdot\hat{\mathbf{k}})ikT^{j+1/2}_{e1k}-n_{e0}T_{e0}iku^{j+1}_{1ky}\,, \tag{5.6}$$

$$\frac{\Delta B_{1kx}}{\Delta t}+\frac{1}{2}(\mathbf{u}_0\cdot\hat{\mathbf{k}})ik\Delta B_{1kx}+\frac{\eta}{\mu_0}k^2\Delta B_{1kx}=B_0ik(cs)u_{1kx}^{j+1}-(\mathbf{u}_0\cdot\hat{\mathbf{k}})ikB_{1kx}^{j+1/2}$$
$$-\frac{\eta}{\mu_0}k^2B_{1kx}^{j+1/2}\,, \tag{5.7}$$

$$\frac{\Delta B_{1ky}}{\Delta t}+\frac{1}{2}(\mathbf{u}_0\cdot\hat{\mathbf{k}})ik\Delta B_{1ky}+\frac{\eta}{\mu_0}k^2\Delta B_{1ky}=-(\mathbf{u}_0\cdot\hat{\mathbf{k}})ikB_{1ky}^{j+1/2}-\frac{\eta}{\mu_0}k^2B_{1ky}^{j+1/2}\,, \tag{5.8}$$

$$\frac{\Delta B_{1kz}}{\Delta t}+\frac{1}{2}(\mathbf{u}_0\cdot\hat{\mathbf{k}})ik\Delta B_{1kz}+\frac{\eta}{\mu_0}k^2\Delta B_{1kz}=-B_0ik(sn)u_{1ky}^{j+1}+B_0ik(cs)u_{1kz}^{j+1}$$
$$-(\mathbf{u}_0\cdot\hat{\mathbf{k}})ikB_{1kz}^{j+1/2}-\frac{\eta}{\mu_0}k^2B_{1kz}^{j+1/2}\,, \tag{5.9}$$

$$\begin{aligned}\frac{\Delta(f_{i1})_{1k}}{\Delta t}&+\theta_f ik(cs)\xi sv_{Ti0}(\Delta f_{i1})_{1k}-\theta_{C_{ii}}C_{ii}((\Delta f_{i1})_{1k},f_{Mi0})-\theta_{C_{ii}}C_{ii}(f_{Mi0},(\Delta f_{i1})_{1k})\\
&-\left\{\theta_f\frac{\xi sv_{Ti0}}{n_{i0}T_{i0}}\left[\frac{2}{3}ik(cs)\pi_{i\|}((\Delta f_{i1})_{1k},T_{i0})\right]\right.\\
&\left.+\theta_{q_{i\|}}\frac{2}{3n_{i0}T_{i0}}\left(s^2-\frac{3}{2}\right)ik(cs)q_{i\|}((\Delta f_{i1})_{1k},T_{i0})\right\}f_{Mi0}\\
&=C_{ii}((f_{i1}^{j+1/2})_{1k},f_{Mi0})+C_{ii}(f_{Mi0},(f_{i1}^{j+1/2})_{1k})-ik(cs)\xi sv_{Ti0}(f_{i1}^{j+1/2})_{1k}\\
&+\left\{\frac{\xi sv_{Ti0}}{T_i}ik(cs)T_{i1k}^*\left(\frac{5}{2}-s^2\right)+\frac{\xi sv_{Ti0}ik(cs)}{n_{i0}T_{i0}}\frac{2}{3}\pi_{i\|}((f_{i1}^{j+1/2})_{1k},T_{i0})\right.\\
&+P_2(\xi)\frac{2}{3}s^2\left(iku_{1ky}^*-3ik(cs)((cs)u_{1ky}^*+(sn)u_{1kz}^*)\right)\\
&\left.+\frac{2}{3n_{i0}T_{i0}}\left(s^2-\frac{3}{2}\right)ik(cs)q_{i\|}((f_{i1}^{j+1/2})_{1k},T_{i0})\right\}f_{Mi0}\,,\end{aligned} \tag{5.10}$$

where subscripts of 0 or 1 indicate an equilibrium quantity or perturbed quantity respectively, $\theta_{C_{ii}}$ is the time centering of the collision operator terms in the kinetic equation, θ_f is the centering of all

other terms in the kinetic equation except the heat flux drive term, and the quantities with $*$ or $**$ superscripts have arbitrary time centering as follows:

$$(f_{i1}^{*})_{1k} = (f_{i1}^{j+1/2})_{1k} + \theta_{fu}(\Delta f_{i1})_{1k} \ , \tag{5.11}$$

$$(f_{i1}^{**})_{1k} = (f_{i1}^{j+1/2})_{1k} + \theta_{ft}(\Delta f_{i1})_{1k} \ , \tag{5.12}$$

$$T_{i1k}^{*} = T_{i1k}^{j+1/2} + \theta_{t}(\Delta T_{i1k}) \ , \tag{5.13}$$

$$\mathbf{u}_{1k}^{*} = \mathbf{u}_{1k}^{j} + \theta_{u}(\Delta \mathbf{u}_{1k}) \ , \tag{5.14}$$

where θ_{fu} is the centering of $(f_{i1})_{1k}$ in the flow equation, θ_{ft} is the centering of $(f_{i1})_{1k}$ in the ion temperature equation, θ_t is the centering of the T_{i1k} in the kinetic equation, and θ_u is the centering of $\mathbf{u}_{1k}$ in the kinetic equation. The moment quantities in Eqs. (5.1)-(5.10) are

$$q_{i\|}((\_\_\_), T_{i0}) = \pi m_i v_{Ti0}^{6} \int_0^{\infty} \mathrm{d}s s^5 \int_{-1}^{1} \mathrm{d}\xi \xi (\_\_\_) \ , \tag{5.15}$$

and

$$\pi_{i\|}((\_\_\_), T_{i0}) = 2\pi m_i v_{Ti0}^{5} \int_0^{\infty} \mathrm{d}s s^4 \int_{-1}^{1} \mathrm{d}\xi P_2(\xi) (\_\_\_) \ , \tag{5.16}$$

where $(\_\_\_)$ is a stand in for either $(f_{i1}^{j+1/2})_{1k}$ or $(\Delta f_{i1})_{1k}$. All centering parameters are arranged in a vector for convenience (where the previously-defined centering of the heat flux drive term in the kinetic equation ($\theta_{q_{i\|}}$) is also included):

$$\boldsymbol{\theta} = \begin{bmatrix} \theta_{C_{ii}} & \theta_{q_{i\|}} & \theta_f & \theta_{fu} & \theta_{ft} & \theta_t & \theta_u \end{bmatrix} \ . \tag{5.17}$$

Other centerings have also been investigated, such as independently centering each term in the

CEL kinetic equation, as well as allowing arbitrary fluid centerings that vary from the standard NIMROD fluid centerings. However, the centering parameters in Eq. (5.17) end up being the most pertinent to the results of the stability analysis herein. See Appendix A for Eqs. (5.1)-(5.10) in more general form, with additional arbitrary centerings allowed, and with the equilibrium f_{i1} allowed to be non-zero.

Before proceeding with the linear analysis, all quantities in Eqs. (5.1)-(5.10) are first normalized by relevant parameters. The magnetic field is normalized by B_0, all number densities are normalized by n_{i0}, and all temperatures are normalized by T_{i0}. The velocity is normalized by the Alfvén velocity, all lengths by the ion skin depth ($d_i = c/\sqrt{n_i Z_{\text{eff}}^2 e^2/\epsilon_0 m_i}$, with c the speed of light), time by the ion inverse cyclotron frequency ($\Omega_i^{-1} = 1/(Z_{\text{eff}} e B_0/m_i)$), and the kinetic distribution function by the zeroth-order Maxwellian at its maximum (i.e., $n_{i0}/v_{Ti0}^3 \pi^{3/2}$). After normalization, each equation is also scaled to be unit-less.

The velocity space dependence of Eq. (5.10) is handled by utilizing the Galerkin approach for the ξ dependence and the collocation approach for the s dependence (as described in Sec. 3.1). 8 collocation points are used in s, and polynomial basis functions of degree 9 are used in three finite element cells in pitch angle. Because the background is uniform, the exact trapped-passing grid in ξ is not utilized in this analysis (i.e., the cell boundaries are uniform in pitch angle). Eq. (5.10) transforms into a system of equations, each defined with a vector of kinetic distribution function coefficients, $(\mathbf{f}_{i1})_{1k}$. λ is defined as the eigenvalues of the time step matrix, where the time step matrix evolves all perturbed quantities in time, i.e.,

$$\begin{pmatrix} u_{1kx}^{j+1} \\ u_{1ky}^{j+1} \\ u_{1kz}^{j+1} \\ B_{1kx}^{j+3/2} \\ B_{1ky}^{j+3/2} \\ B_{1kz}^{j+3/2} \\ T_{i1k}^{j+3/2} \\ T_{e1k}^{j+3/2} \\ n_{e1k}^{j+3/2} \\ (\mathbf{f}_{i1}^{j+3/2})_{1k} \end{pmatrix} = \mathbf{A}(k) \begin{pmatrix} u_{1kx}^{j} \\ u_{1ky}^{j} \\ u_{1kz}^{j} \\ B_{1kx}^{j+1/2} \\ B_{1ky}^{j+1/2} \\ B_{1kz}^{j+1/2} \\ T_{i1k}^{j+1/2} \\ T_{e1k}^{j+1/2} \\ n_{e1k}^{j+1/2} \\ (\mathbf{f}_{i1}^{j+1/2})_{1k} \end{pmatrix}, \tag{5.18}$$

with $\mathbf{A}(k)$ the time step matrix. The time step matrix is found by combining Eqs. (5.1)-(5.10). Finally $\lambda = e^{-i\omega\Delta t}$ is specified for convenience. The goal will be to pick a set of centering $\theta's$ such that $\forall\ k$, $\text{Im}(\omega) \leq 0$. This condition allows for some artificial numerical damping of the linear modes. Later, it will be shown how this condition can be made more restrictive to also remove the

artificial damping from the system.

5.1 Restricting fluid moments of f_{i1}

Analytically, the fluid moments of f_{i1} remain at 0 if they start at 0, (as was shown in Sec. 2.2), but they can become numerically non-zero over time with finite resolution in velocity space. Numerical stability ends up being impossible to achieve without a method to first constrain these fluid moments. Previous efforts in other, more-simplified CEL implementations have focused on subtracting off appropriate fluid projections of f_{i1} at every time step in order to prevent growth of the fluid moments of f_{i1} [54, 55]. One could include the effects of this method in a von Neumann linear stability analysis by incorporating an auxiliary kinetic distribution function variable $f_{i1,\mathrm{pred}}$ into the linear system, representing f_{i1} after the kinetic equation advance but before projecting off the fluid moments. However, incorporating $f_{i1,\mathrm{pred}}$ into the linear system would approximately quadruple the size of the time-step matrix. Instead, the method used herein to keep the fluid moments of f_{i1} small involves adding additional terms to the RHS of Eq. (2.7). Specifically the non-time-derivative terms from Eqs. (2.10)-(2.12) are added to the RHS side of Eq. (2.7), multiplied by appropriate velocity space weightings:

$$
\begin{aligned}
&\left\{\frac{1}{n_i}\left(\frac{1}{m_i}\mathbf{b}\cdot\nabla(f_{i1})_{(n_i m_i u_{i\parallel})} - \frac{1}{m_i}(f_{i1})_{(n_i m_i u_{i\parallel})}\mathbf{b}\cdot\nabla\ln B\right.\right.\\
&\qquad\left.\left. - \left(C_{ii}\left(f_{i1}, f_{Mi}\right) + C_{ii}\left(f_{Mi}, f_{i1}\right)\right)_{(n_i)} + D\nabla^2(f_{i1})_{(n_i)}\right)\left(\frac{5}{2} - s^2\right)\right.\\
&+\frac{\xi s v_{Ti}}{n_i T_i}\left(\frac{2}{3}\mathbf{b}\cdot\nabla(f_{i1})_{((3/2)n_i T_i)} - \left(T_i(f_{i1})_{(n_i)}\right)\mathbf{b}\cdot\nabla\ln n_i\right.\\
&\qquad\left. - \left(C_{ii}\left(f_{i1}, f_{Mi}\right) + C_{ii}\left(f_{Mi}, f_{i1}\right)\right)_{(n_i m_i u_{i\parallel})} + D\nabla^2(f_{i1})_{(n_i m_i u_{i\parallel})}\right)\left(\frac{7}{2} - s^2\right)\\
&+\frac{2}{3n_i T_i}\left(s^2 - \frac{3}{2}\right)\left(-\frac{T_i}{m_i}(f_{i1})_{(n_i m_i u_{i\parallel})}\mathbf{b}\cdot\nabla\ln n_i - \left(C_{ii}\left(f_{i1}, f_{Mi}\right) + C_{ii}\left(f_{Mi}, f_{i1}\right)\right)_{((3/2)n_i T_i)}\right.\\
&\qquad\left.\left. + D\nabla^2(f_{i1})_{((3/2)n_i T_i)}\right)\right\} f_{Mi}\,,
\end{aligned}
\tag{5.19}
$$

where diffusion of the fluid moments of f_{i1} is also allowed through inclusion of the diffusive terms (D being the diffusivity). The velocity weightings (which are easily obtained by noting the orthogonality relations for both the generalized Laguerre polynomials and the Legendre polynomials) ensure that

the added terms only affect the fluid moment equations (Eqs. (2.10)-(2.12)), and not directly the evolution of $q_{i\parallel}$ or $\pi_{i\parallel}$ dictated by the kinetic equation (i.e., the $q_{i\parallel}$ and $\pi_{i\parallel}$ moments of the extra terms are zero)[1]. The effect of these added terms is to cancel terms on the LHS of Eqs. (2.10)-(2.12), so that each fluid moment evolution equation is simply a diffusion equation. This method will be referred to as the suppression of fluid moments (SFM) method.

Including these additional terms in the linear analysis will modify Eq. (5.10). The new diffusive terms are centered backward in time, the moments of the collision operator with $\theta_{C_{ii}}$, and all other terms with θ_f. For Eq. (5.10) with the added terms, see Appendix B.

Higher velocity space resolution does not alleviate the need for SFM. Using the centerings deduced below ($\boldsymbol{\theta}_1$ in Section 5.2), it can be seen in Fig. 5.1 that significantly increasing the velocity space resolution (without SFM) only has a nominal effect on the maximum growth rate, whereas utilizing SFM drops the growth rates to 0 within numerical precision. This underscores the importance of SFM to a numerically-stable time advance.

5.2 Results of stability analysis

To find a $\boldsymbol{\theta}$ that gives $\mathrm{Im}(\omega) \leq 0$ (to within numerical precision), both trial and error, as well as Matlab's fmincon algorithm is used. $C_0 = 0.3$ is used in this analysis, which is just above the stability threshold for the fluid part of the system (see Ref. [68]). $cs = 1$ and $sn = 0$ are also used, as this ends up being the most restrictive in terms of stability criteria. To avoid a potentially overly-restrictive CFL condition due to the advective term in the kinetic equation, or other potential time step restrictions due to the collision operator terms, $\theta_f = \theta_{C_{ii}} = 1.0$ is used. Additionally, since the kinetic equation is evolved last, a solution is sought with $\theta_{fu} = 0.0$ to avoid necessitating a simultaneous solve of both the kinetic and flow evolution equations. $\theta_u = 1.0$ is also used to be consistent with how the other fluid equations are centered with respect to each other in NIMROD. To use only a minimum amount of artificial diffusion of the fluid moments of f_{i1} in the linear analysis, a solution with $D/(d_i^2\Omega_i) \ll 1$ is also sought.

With the above criteria, a complicated dependence of the various centering parameters on each other emerges, offering many different methods to achieve $\mathrm{Im}(\omega) \leq 0$. Importantly, all methods rely on SFM, without which stability is impossible to achieve. The centering parameters related to the coupling of the ion temperature equation and kinetic equation seem to be particularly important for achieving numerical stability–namely, θ_{ft}, θ_t, and $\theta_{q_{i\parallel}}$. The dependence of the growth rate on these

[1]The $(7/2 - s^2)$ weighting – which is included to analytically keep the heat flux moment of that term zero – is probably ultimately not needed if the fluid moments of f_{i1} are kept sufficiently small (which is the goal herein anyways). In addition, the time evolution equations for $q_{i\parallel}$ and $\pi_{i\parallel}$ involve other moments of f_{i1} which may themselves be directly affected by the inclusion of the extra terms. However, an analytical effort to prevent the extra terms from affecting $q_{i\parallel}$ and $\pi_{i\parallel}$ either directly or indirectly ignores the fact that the fluid moments of f_{i1} are zero analytically. Therefore, such an analytical effort is probably superfluous.

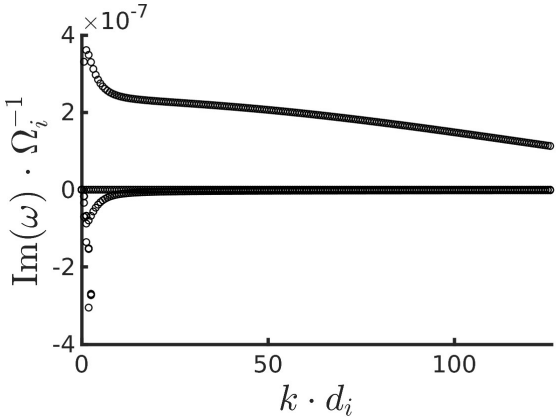

(a) Normalized Re(ω) vs. normalized k for 8 speed collocation points, 28 deg. of freedom in ξ, no SFM, and zoomed in to emphasize the growth rates that are positive.

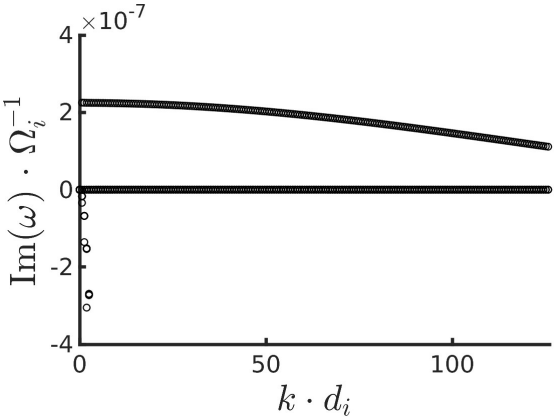

(b) Normalized Re(ω) vs. normalized k for 16 speed collocation points, 28 deg. of freedom in ξ, no SFM, and zoomed in to emphasize the growth rates that are positive.

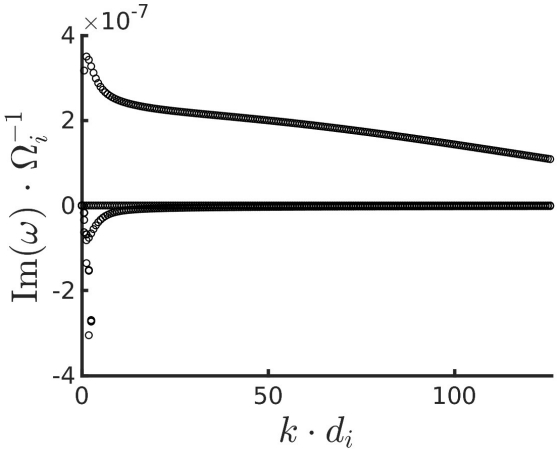

(c) Normalized Re(ω) vs. normalized k for 8 speed collocation points, 55 deg. of freedom in ξ, no SFM, and zoomed in to emphasize the growth rates that are positive.

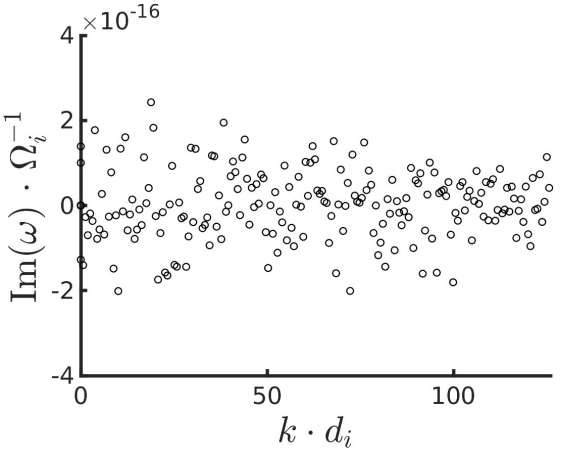

(d) Normalized Re(ω) vs. normalized k for 8 speed collocation points, 28 deg. of freedom in ξ, with SFM, and zoomed in to emphasize the growth rates that are positive.

Figure 5.1: Normalized Re(ω) vs. normalized k for different velocity space resolutions, with and without SFM, with $\boldsymbol{\theta}_1$ centerings, $\Delta t = 10^{-7}$ s, and zoomed in to emphasize the growth rates that are positive. The top two plots (a) and (b) and the bottom left plot (c) are without SFM, and the bottom right plot (d) is with SFM. Significantly changing the velocity space resolution only has a slight effect on the maximum growth rates, whereas they drop to 0 within numerical precision with SFM.

three centering parameters is illustrated in Tables C.1-C.3, where each entry shows the maximum growth rate found over $kd_i \in [0, 40\pi]$. In these tables, a small amount of diffusion of the fluid moments of f_{i1} ($D/(d_i^2\Omega_i) \approx 10^{-13}$) is used.

From Tables C.1-C.3 it is clear that one set of centering parameters that gives $\mathrm{Im}(\omega) \leq 0$ to within numerical precision, and allows a staggered advance of the ion temperature and kinetic

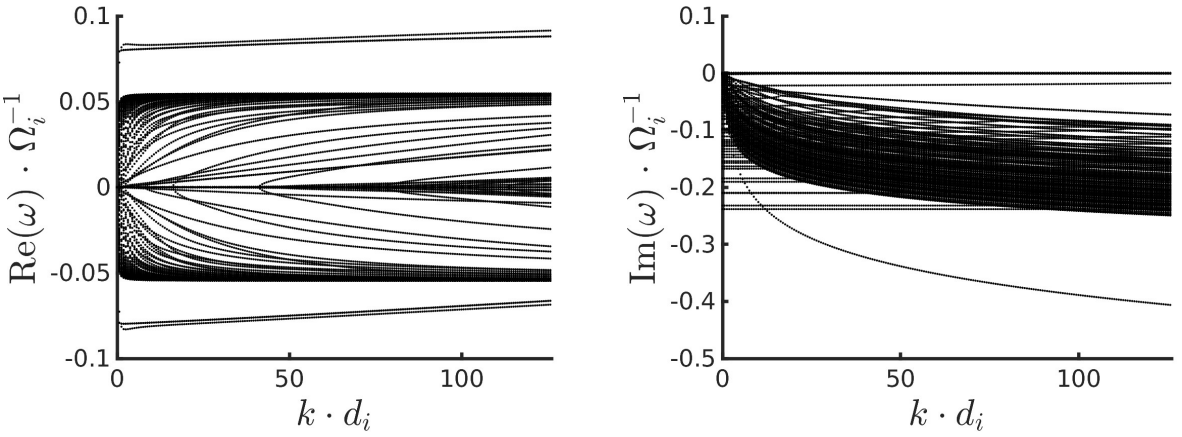

(a) Normalized $\mathrm{Re}(\omega)$ vs. normalized k (b) Normalized $\mathrm{Im}(\omega)$ vs. normalized k

Figure 5.2: Normalized $\mathrm{Re}(\omega)$ vs. normalized k on the left (a) and normalized $\mathrm{Im}(\omega)$ vs. normalized k on the right (b) for $\boldsymbol{\theta}_1$, with $\Delta t = 10^{-7}$ s. The maximum normalized growth rate on (b) is $3.4{\times}10^{-16}$.

equations (i.e., $\theta_{ft} = 0$), is

$$\begin{aligned}\boldsymbol{\theta}_1 &= \begin{bmatrix}\theta_{C_{ii}} & \theta_{q_{i\parallel}} & \theta_f & \theta_{fu} & \theta_{ft} & \theta_t & \theta_u\end{bmatrix} \\ &= \begin{bmatrix}1.0 & 0.0 & 1.0 & 0.0 & 0.0 & 1.0 & 1.0\end{bmatrix} . \end{aligned} \tag{5.20}$$

Interestingly, this has the heat flux term in the kinetic equation centered at the beginning of the time step ($\theta_{q_{i\parallel}} = 0.0$). Also of note is that $\theta_t = 1.0$, which differs from how some of the other fluid equations are centered with respect to each other in NIMROD's leapfrog scheme, (instead of stepping f_{i1} over a time-step-averaged T_i, f_{i1} is stepped using the T_i at the end of its time step). One can also see from Tables C.1-C.3 that allowing θ_t to differ from 0.5 is the only way to achieve a numerically stable non-simultaneous ($\theta_{ft} = 0.0$) advance, which is why it was allowed to vary in this analysis. See Fig. 5.2 for a plot of the frequencies and growth rates associated with this set of centering parameters. The condition $\mathrm{Im}(\omega) \leq 0$ is also found to persist for all time steps using $\boldsymbol{\theta}_1$, which shows that these centering parameters do not impose any CFL or other time step constraints on the system.

To see if this set of centering parameters gives any artificial numerical damping, all sources of explicit damping are removed from the system, and it is seen if any damping ($\mathrm{Im}(\omega) < 0$) remains in the linear modes.[2] To remove the explicit sources of damping, the ion-ion collision operator is

[2]Damping of physically relevant quantities can still occur with no sources of explicit damping [72]. However, in the eigenvector/eigenvalue analysis used herein, this damping shows up as a decorrelation of the eigenvectors due to differing real frequencies, and not as having an associated imaginary part of the frequency (see Appendix D). Future work will compare linear Landau damping results in NIMROD to results from this analysis.

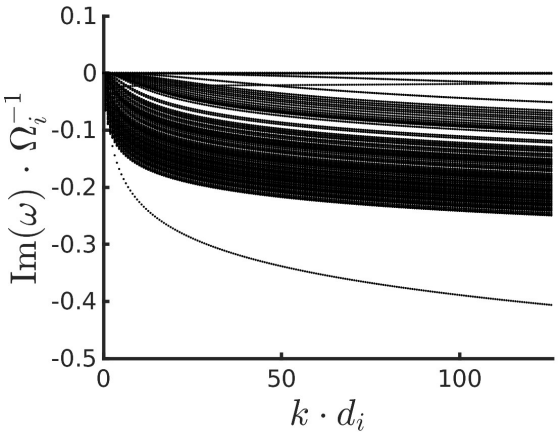

Figure 5.3: Normalized $\mathrm{Im}(\omega)$ vs. normalized k for $\boldsymbol{\theta}_1$, $\Delta t = 10^{-7}$ s, but with no sources of explicit damping included. One can still see significant numerical damping with this set of centering parameters.

removed from the kinetic equation, and η and D are both set to zero. From Fig. 5.3 we can see that there is still a significant amount of artificial damping with this set of centering parameters. In the next subsection, it is shown how the above centering parameters can be modified to also remove the artificial damping.

5.3 Removing the artificial numerical damping from the linear modes

Setting all centering parameters not related to the flow to $\theta = 0.5$ allowed both artificial growth and damping to be eliminated for the fluid-only part of the system (see Ref. [68]), so this method is also pursued when considering the full fluid-kinetic system. A suitable set of centering parameters, which removed both artificial growth and damping, is readily found to be:

$$\begin{aligned}\boldsymbol{\theta}_2 &= \begin{bmatrix}\theta_{q_{i\parallel}} & \theta_f & \theta_{fu} & \theta_{ft} & \theta_t & \theta_u\end{bmatrix} \\ &= \begin{bmatrix}0.5 & 0.5 & 0.0 & 0.5 & 0.5 & 1.0\end{bmatrix}, \end{aligned} \tag{5.21}$$

where SFM is also used here. Like the above subsection, this set of centering parameters brings the artificial growth and damping rates to within numerical precision. $\boldsymbol{\theta}_2$ also applies over all time step sizes. This indicates that, as with $\boldsymbol{\theta}_1$, there is not a CFL constraint that applies to this set of centering parameters. This implies that a fully implicit method is not required for numerical stability.

When considering computations with the collision operator, centering the collision operator

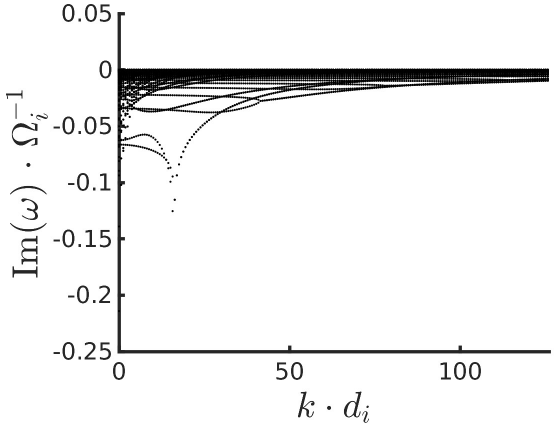

(a) Normalized Im(ω) vs. normalized k with $\theta_{C_{ii}} = 0.5$.

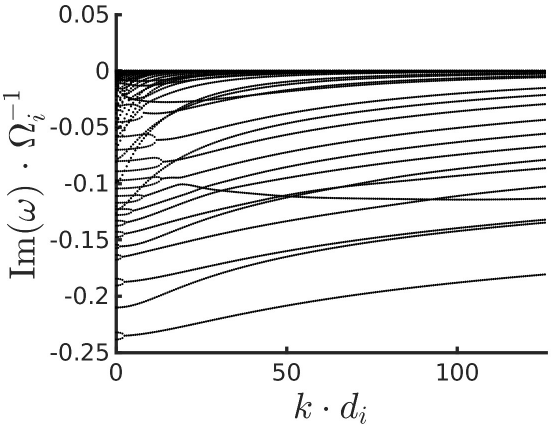

(b) Normalized Im(ω) vs. normalized k with $\theta_{C_{ii}} = 1.0$.

Figure 5.5: Comparison of normalized growth rates when centering the collision operator with $\theta_{C_{ii}} = 1.0$ vs. centering it with $\theta_{C_{ii}} = 0.5$ (with $\boldsymbol{\theta}_2$ used for the other centerings). On the left (a) is with $\theta_{C_{ii}} = 0.5$, and on the right (b) is with $\theta_{C_{ii}} = 1.0$. In both plots $\Delta t = 10^{-7}$ s.

with $\theta_{C_{ii}} = 0.5$ introduces either none, or the least amount of artificial damping in the conditions considered here. See Fig. 5.5 for a comparison of centering the collision operator with $\theta_{C_{ii}} = 1.0$, vs. centering it with $\theta_{C_{ii}} = 0.5$ (with $\boldsymbol{\theta}_2$ used for the other centerings). As is seen in Fig. 5.5, significantly more damping occurs when it is centered with $\theta_{C_{ii}} = 1.0$.

One significant aspect of $\boldsymbol{\theta}_2$ is that it involves a simultaneous advance of both the ion temperature and kinetic equations ($\theta_{ft} = 0.5$). There does not seem to be a way around a simultaneous advance if one wants to remove the artificial damping from the linear modes.

It is also noted that $C_0 = 0.3$ ended up being important in preventing the need for a simultaneous flow and kinetic equation advance. The standard fluid value of $C_0 = 0.25$, with the $\boldsymbol{\theta}_2$ centerings, gives significant artificial growth and damping of the linear modes, as can be seen in Fig. 5.6. The artificial growth and damping associated with $C_0 = 0.25$ can be removed if $\boldsymbol{\theta}_2$ is modified so all centering parameters are 0.5, however, this would imply that the flow equation is also part of the simultaneous advance. To use $\boldsymbol{\theta}_2$, an empirically determined rough estimate for the minimum value for C_0 needed is $C_0 \gtrsim 0.28563$.

5.4 Summary

It has been shown that for a coupled fluid-kinetic CEL closure approach, centering the heat flux at the beginning of the time step and the ion temperature at the end of the time step in the kinetic equation allows for a numerically-stable time advance of the coupled system. It has also been shown

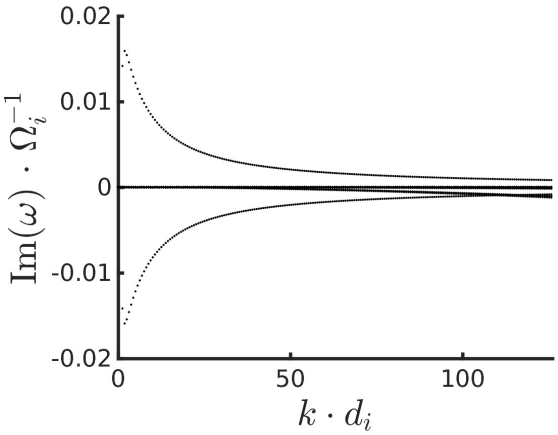

Figure 5.6: Normalized $\mathrm{Im}(\omega)$ vs. normalized k for $C_0 = 0.25$, using the $\boldsymbol{\theta}_2$ centerings, with no sources of explicit damping, and with $\Delta t = 10^{-7}$ s. Significant artificial growth and damping is seen.

that the centerings associated with the coupling between the ion temperature and kinetic equations are of paramount importance for stability. In addition, it has been shown that it is possible to eliminate both the numerical damping and the numerical growth from the linear modes. Numerical stability relies on a method to constrain the fluid moments of f_{i1}. The SFM strategy implemented herein is to add terms from the evolution equations for the fluid moments of f_{i1} to the RHS of the kinetic equation, in such a way as to cancel sources of numerical growth of those moments in the kinetic equation. This analysis shows that linearly stable algorithms are possible with SFM.

6 AN AXISYMMETRIC BENCHMARK OF THE FULL CEL CLOSURE APPROACH ALGORITHM IN NIMROD

A relevant application for the coupled fluid-kinetic system is that of the nonlinear damping of the poloidal flow in an axisymmetric tokamak. The time evolution of the poloidal flow in such a configuration, as has been previously stated, is crucially dependent on the ion viscous stress tensor $\mathbf{\Pi}_i$ [73, 19], and $\mathbf{\Pi}_i$ will reach steady-state on the timescale set by the dissipative term in the kinetic equation (i.e., the collision operator). It is noted that the axisymmetric computations in this chapter include significantly more physics/geometric considerations than previous, more-simplified, numerical implementations of the CEL approach (such as in Refs. [53, 54, 55]). A DIII-D[1] equilibrium is used herein, which is a kinetic reconstruction of DIII-D ITER Baseline Scenario (IBS) discharge 174446 at 3390 ms [57, 49]. Deuterium is assumed for the ions, and $Z_{\text{eff}} = 3$ is used to give results roughly consistent with having impurity species. In Fig. 6.1, the $|\mathbf{B}|$ contours, a few representative flux surfaces, and equilibrium values of the pressure, ion temperature, safety factor, and $\nu^\star$ (where a formula for $\nu^\star$ is used that is valid for arbitrary geometry [74]) are plotted as a function of flux surface label for this equilibrium. Although $\nu^\star \sim O(1)$ over most of the domain for this equilibrium, it still provides a good test case for our kinetic formulation as kinetic effects remain important even for moderately collisional equilibria (i.e., when not in the asymptotic collisional regime).

For a test problem, the initial flow is set to 0 and no implicit sources are assumed except a small implied loop voltage in Ohm's law (Eq. (3.5)). The computational domain extends out to the last closed flux surface (LCFS), and a perfectly conducting wall at the LCFS is assumed. The fluid variables, magnetic field, and kinetic distortion are then allowed to evolve fully non-linearly according to Algorithm 1 until the flow is in steady state. Perpendicular particle drifts (located as drives on the RHS of the kinetic equation) initially drive the flow away from zero. The steady-state condition $\nabla \cdot \mathbf{u} = 0$ then implies that parallel flow must be generated to compensate for $\nabla \cdot \mathbf{u}_\perp \neq 0$ from the drifts. The flow eventually damps to a steady-state value through particle collisions. A small amount of ad-hoc diffusion is used in all equations to stabilize non-linear numerical instabilities. The profiles for $D_u = D_n = D_{T_i} = D_{f_{i1}} = D_{\text{ad-hoc}}$ are shown in Fig. 6.2, and are flat at 1 m^2/s over most of the domain, but rise sharply near the edge of the computational domain which helps with numerical stability when using homogeneous boundary conditions. To avoid a simultaneous ion temperature and kinetic equation advance, the $\boldsymbol{\theta}_1$ centerings from Ch. 5 are used for the results herein[2]. In addition, SFM is used, but D in Eq. (5.19) is set to 0 as it has been found to have

[1] DIII-D is an experimental tokamak located in San Diego, CA, USA.

[2] See Ref. [75] for a verification of a simultaneous temperature and kinetic equation advance implemented in NIMROD.

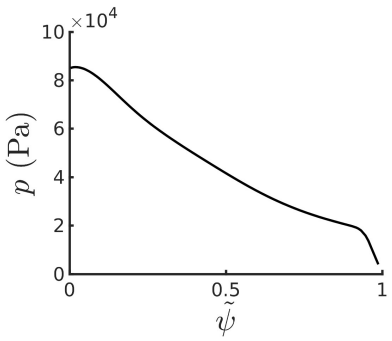

(a) Total pressure vs. normalized poloidal magnetic flux ($\tilde{\psi}$).

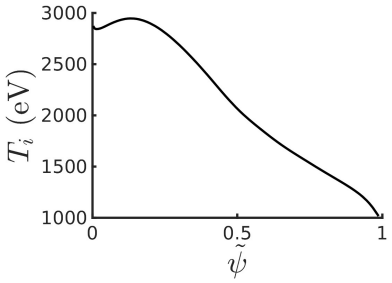

(b) Ion Temperature vs. normalized poloidal magnetic flux ($\tilde{\psi}$).

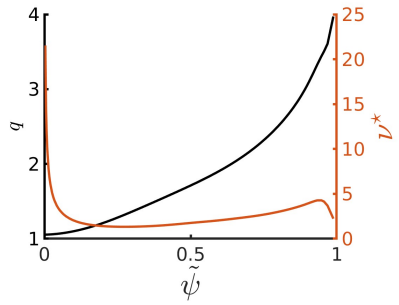

(c) Safety factor (q) and collisionality ($\nu^\star$) vs. normalized poloidal magnetic flux ($\tilde{\psi}$).

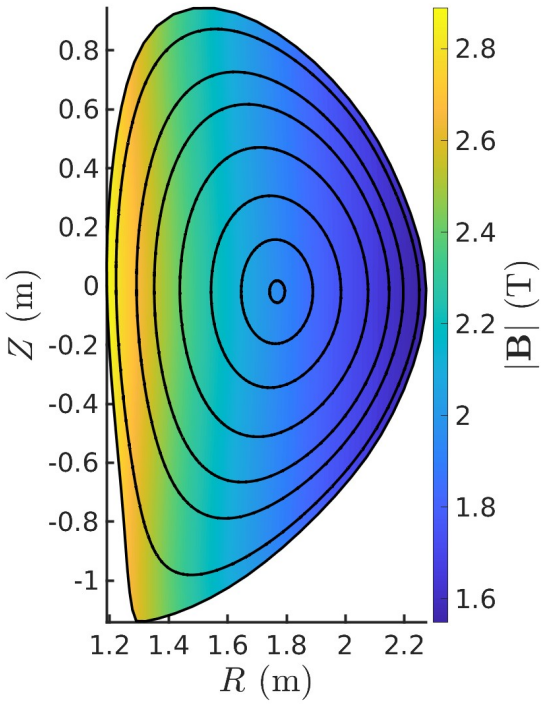

(d) $|\mathbf{B}|$ contours, with a few representative flux surfaces.

Figure 6.1: Equilibrium profiles for DIII-D IBS discharge 174446 at 3390 ms.

little added effect when running the CEL approach in NIMROD fully non-linearly (in effect, all the needed diffusion is obtained by including an ad-hoc diffusion coefficient in the kinetic equation of 1 m^2/s).

For physical space, an approximately flux-aligned finite element mesh in the poloidal plane is used, with polynomial basis functions of degree 3 in each cell. Because the grid is packed near the X-point, it deviates from being flux-aligned along the ray that extends out from the magnetic axis to the X-point. In velocity space, 16 collocation points in s and polynomial basis functions of degree 9 are used in each of three cells in pitch angle. See Figs. 6.3-6.4 for the numerical grids used in both

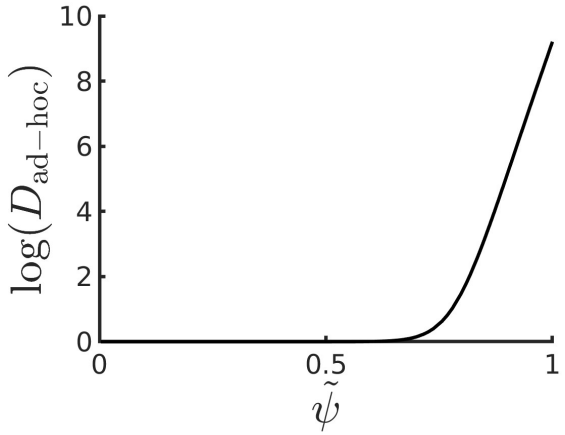

Figure 6.2: $\log(D_{\text{ad-hoc}})$ vs. normalized poloidal flux ($\tilde{\psi}$). A sharp rising of the artificial diffusion near the edge of the domain helps with numerical stability when using homogeneous boundary conditions.

physical space and velocity space. The exact trapped-passing grid in ξ is not used herein as it has been found to give little benefit for $\nu^\star \gtrsim 1$ cases.

Evidence of numerical convergence is seen in Figs. 6.5-6.6, where $\pi_{i\|}$ and $q_{i\|}$ are compared between a lower and higher resolution run. The max percent difference (relative to the maximum of the absolute value of the corresponding lower resolution plot) in these figures is about 6% over most of the physical domain. There are localized areas near the edge of the physical domain (where diffusion shaping is high) where the percent difference approaches 17%; however, it has been verified that this difference is due solely to increasing the physical space resolution. Further increasing the physical space resolution to polynomial basis functions of degree 4 only results in a max change of $< 5\%$ in these edge areas.

It is also noted here the definition of "poloidal" that we use. Because $\nabla\phi \times \nabla\psi$ denotes the magnetic field component in the R-Z plane (see Sec. 1.2.4), the poloidal direction is defined herein to be anti-parallel to this component; specifically, the poloidal component of any vector is defined to be the dot product of that vector with $-(\nabla\phi \times \nabla\psi)/|\nabla\phi \times \nabla\psi|$, and a subscript θ is used to represent that component. The off-flux surface component of any vector is defined to be the dot product of that vector with $-\nabla\psi/|\nabla\psi|$, and a subscript ψ is used to represent that component.

6.1 Numerical Results and Discussion

The SFM method introduced in Sec. 5.1 is crucial in allowing the poloidal flow to evolve to steady state without numerical instabilities. See Fig. 6.7 for a comparison of the time evolution of the poloidal flow (u_θ), toroidal flow (u_ϕ), and parallel viscosity with SFM vs. without SFM, where these quantities are evaluated at a set of synthetic probe locations in the poloidal plane. The locations

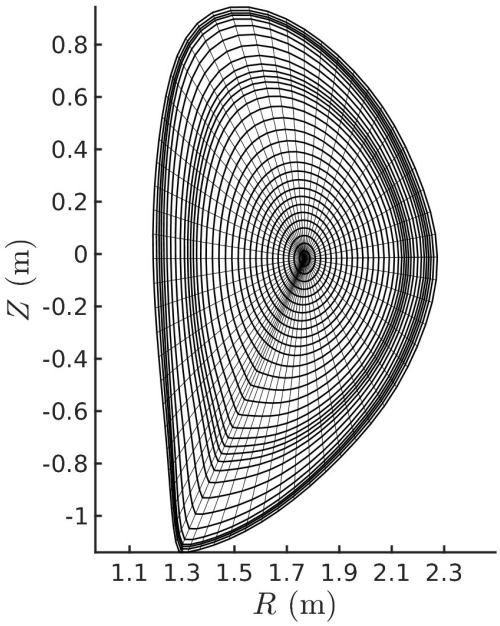

Figure 6.3: Numerical grid in the poloidal plane, with polynomial basis functions of degree 3 used in each cell. It is approximately flux-aligned, but X-point packing causes the grid to become non-flux-aligned along the ray from the magnetic axis to the X-point.

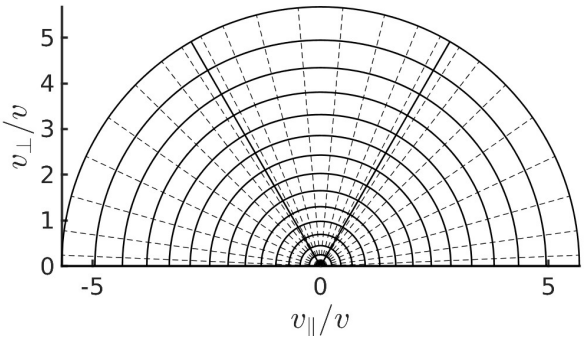

Figure 6.4: Numerical grid in velocity space, showing the three finite element cells in pitch angle and 16 collocation points in s that are used. Each finite element cell uses polynomial basis functions of degree 9 (with node locations plotted with the dotted lines).

of the synthetic probes used for our time evolution plots herein are given in Fig. 6.8, where the probe locations are overlaid on a contour plot of the steady-state u_θ/B_θ. The colors for the probe locations on this plot correspond to the colors on all plots that evaluate quantities at the synthetic probe locations. As seen in Fig. 6.7, the simulation crashes before the poloidal flow reaches steady state without SFM, whereas with SFM, the poloidal flow is able to attain steady state. In Fig. 6.9 it is seen that SFM is able to successfully keep the fluid moments of f_{i1} small, whereas without SFM, the fluid moments of f_{i1} grow as large as the perturbed fluid variables, ultimately crashing the simulation. In Fig. 6.10, a contour plot of the steady-state f_{i1} at $(R, Z) \approx (2.05\text{ m}, 0.00\text{ m})$ shows a strong $P_1(\xi)$ dependence, indicating the need for a large $q_{i\parallel}$ response to balance the Braginskii diamagnetic cross heat flux in the steady state. The time evolution of additional quantities of interest evaluated at the synthetic probe locations are given in Fig. E.1.

In this test run, no difference was observed between using $\theta_{q_{i\parallel}} = 0.0$ vs. $\theta_{q_{i\parallel}} = 1.0$ – both ran out stably to identical answers. Other non-linear runs in NIMROD, however, have required getting the heat flux centering right (namely, using $\theta_{q_{i\parallel}} = 0.0$) to avoid a numerical instability.

It is also seen in Fig. 6.7 that the poloidal flow reaches steady-state on the time-scale of the

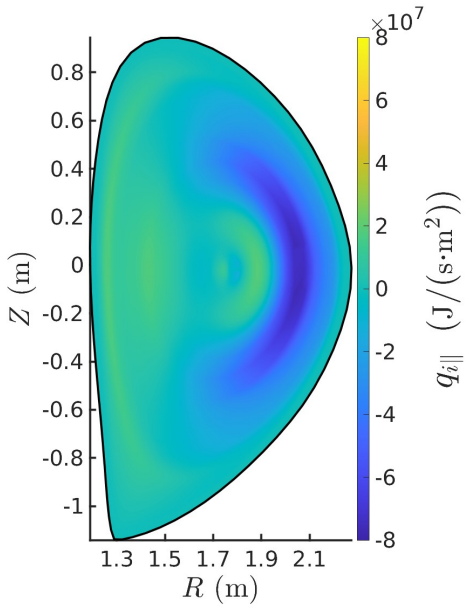

(a) CEL $q_{i\parallel}$ closure in the steady state.

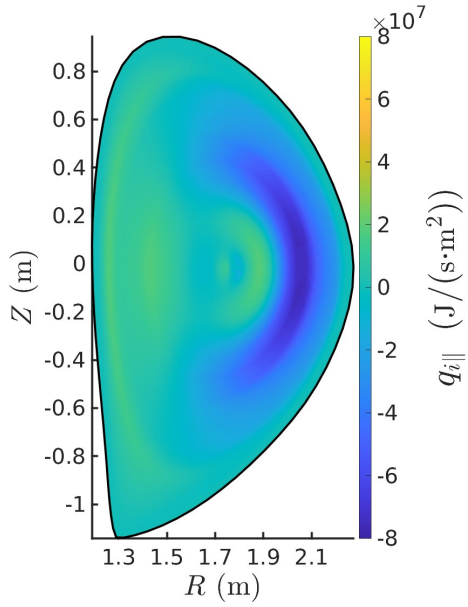

(b) CEL $q_{i\parallel}$ closure in the steady state, from a lower resolution run.

Figure 6.5: Comparison of the steady-state kinetic $q_{i\parallel}$ (16 collocation points in s, polynomial basis functions of degree 9 in logical pitch angle, polynomial basis functions of degree 3 in the poloidal plane) on the left (a) with the steady-state kinetic $q_{i\parallel}$ from a lower resolution run (8 collocation points in s, polynomial basis functions of degree 7 in logical pitch angle, polynomial basis functions of degree 2 in the poloidal plane) on the right (b). The max percent difference (relative to the max of the absolute value of the lower resolution plot) between (a) and (b) is about 2%.

ion-ion collision time, ν_{ii}^{-1}, which is $\approx 6 \times 10^{-5}$ s on axis for this equilibrium. This is in agreement with prior predictions that have used various assumptions [24, 25]. Locally the toroidal flow evolves on the same time scale as the poloidal flow; however, the flux surface average of the toroidal flow $\langle Ru_\phi \rangle$ evolves on a longer time scale consistent with the predictions of neoclassical transport theory [76]. These observations break down in the edge region with large artificial diffusion. In Fig. 6.11, it can be seen that $\langle Ru_\phi \rangle$ remains small throughout the time evolution away from the edge, which is in accordance with these observations.

The off-flux-surface flow u_ψ is less than 1% of $\mathbf{u}$ in the steady state (see Appendix E), which is also in accordance with standard neoclassical theory [18, 19]. It is noted that the computational model used herein includes more physics than standard neoclassical theory, including wave equilibration; however, the neoclassical result in the steady state is still recovered.

As stated previously, a fixed-background δf approach is not well-suited for cases involving large departures of the fluid variables from equilibrium; however, for this axisymmetric application with no initial flow based on an experimentally relevant equilibrium, the perturbed fluid variables remain small compared to their equilibrium values throughout the time evolution (where "small"

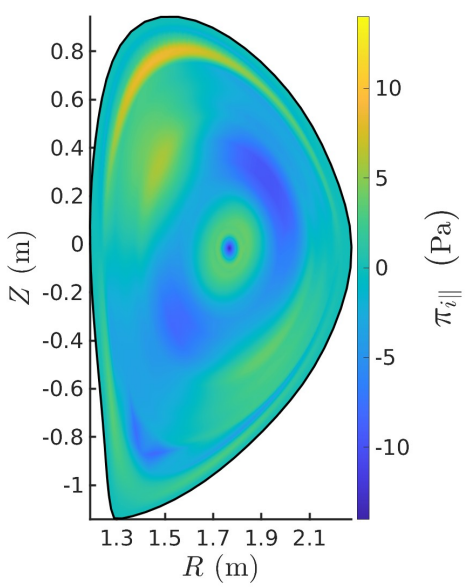

(a) CEL $\pi_{i\|}$ closure in the steady state.

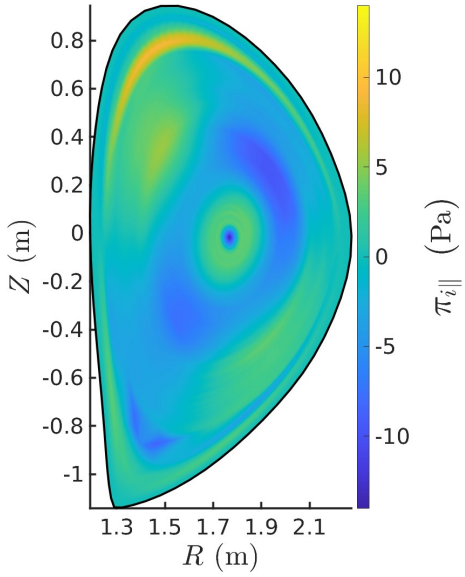

(b) CEL $\pi_{i\|}$ closure in the steady state, from a lower resolution run.

Figure 6.6: Comparison of the steady-state kinetic $\pi_{i\|}$ (16 collocation points in s, polynomial basis functions of degree 9 in logical pitch angle, polynomial basis functions of degree 3 in the poloidal plane) on the left (a) with the steady-state kinetic $\pi_{i\|}$ from a lower resolution run (8 collocation points in s, polynomial basis functions of degree 7 in logical pitch angle, polynomial basis functions of degree 2 in the poloidal plane) on the right (b). The max percent difference (relative to the max of the absolute value of the lower resolution plot) between (a) and (b) is about 6% over most of the physical domain. There are localized areas near the edge of the physical domain (where diffusion shaping is high) where the percent difference approaches 17%; however, it has been verified that this difference is due solely to increasing the physical space resolution. Further increasing the physical space resolution to polynomial basis functions of degree 4 only results in a max change of $< 5\%$ in these edge areas.

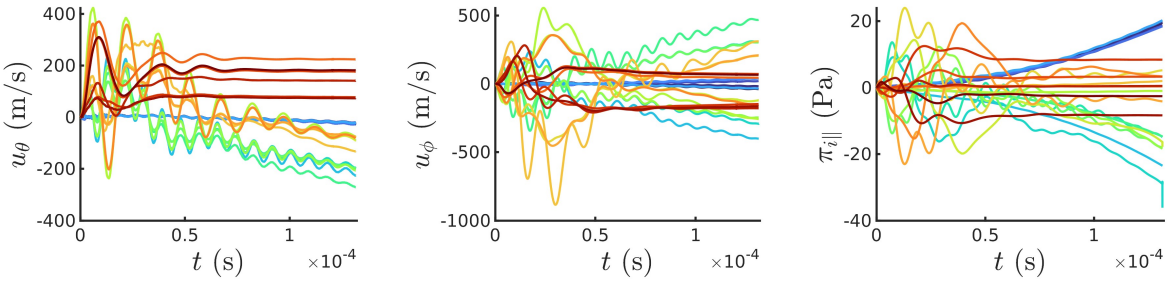

(a) Time evolution of poloidal flow, toroidal flow, and parallel viscosity at a representative set of synthetic probe locations in the poloidal plane, without SFM.

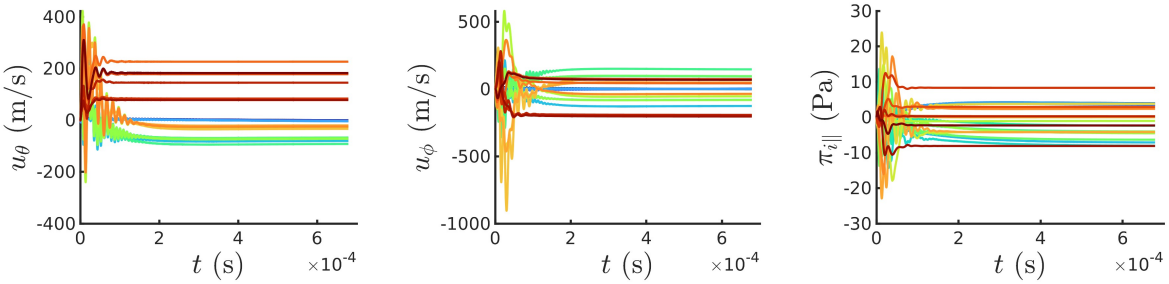

(b) Time evolution of poloidal flow, toroidal flow, and parallel viscosity at a representative set of synthetic probe locations in the poloidal plane, with SFM.

Figure 6.7: Comparison of the time evolution of the poloidal flow, toroidal flow, and parallel viscosity at a representative set of synthetic probe locations in the poloidal plane (see Fig. 6.8) without SFM (a), and with SFM (b). The simulation crashes before reaching steady state in (a), but is able to reach steady state in (b).

for the flow is defined as small relative to v_{Ti}). Because of this, the CEL result for the steady-state poloidal flow is benchmarked with that obtained using a previously benchmarked, fixed-background δf implementation in NIMROD. Specifically, what was termed the "δf approach" in Ch. 4 is used. An initially zero fixed-background f_{i1} is evolved to steady state using the fixed-background δf kinetic equation and the methods of Sec. 4.3.2 are used to calculate the poloidal flow from the steady-state fixed-background f_{i1}. Fig. 6.12 compares the results for the steady-state poloidal flow between the two approaches, with decreasing on-axis values for the artificial diffusion used in the fixed-background δf approach. The results of the two approaches are seen to converge to each other as the artificial diffusion used in the fixed-background δf approach is decreased, with the exception of close to the edge where the diffusion shaping is large. In order to decrease diffusion at the core in the fixed-background δf approach, the diffusion at the edge had to be increased to maintain numerical stability. It is surmised that at least some of the discrepancy can also be attributed to differing effects of diffusion shaping between the two approaches – in the CEL approach, the shaping is used in all the fluid equations as well as the kinetic equation, whereas in the fixed-background δf approach it is used only in the kinetic equation. Fig. 6.12 seems to indicate that diffusion has a

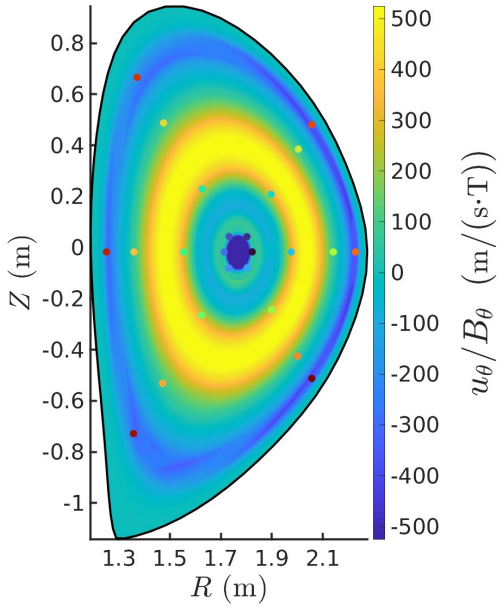

Figure 6.8: Synthetic probe locations in the poloidal plane, overlaid on the steady-state u_θ/B_θ. The colors for the probes on this plot correspond to the colors on all plots that evaluate quantities at the synthetic probe locations.

larger effect in the fixed-background δf approach than in the CEL approach. Also, the fact that the fixed-background δf approach seems to be nearly converged in $D_{\text{ad-hoc}}$ away from the edge, and agrees well with the CEL approach, suggests that the CEL approach is also converged in artificial diffusion there.

6.2 Summary

A successful benchmarking of the full CEL approach in NIMROD has been performed when running fully nonlinearly in axisymmetric geometry. Observing both the poloidal and toroidal flow dynamics as well as the steady-state poloidal flow assisted in verifying the correctness of the numerical implementation. The time dynamics of both the toroidal and poloidal flows agree with analytical predictions. SFM was found to be essential in enabling a numerically stable evolution to steady state. That the fluid variables remain close to equilibrium over the flow evolution also facilitated a comparison with a previously benchmarked, fixed-background δf calculation of the steady-state poloidal flow. The steady-state poloidal flow from the CEL approach agrees well with the fixed-background δf result.

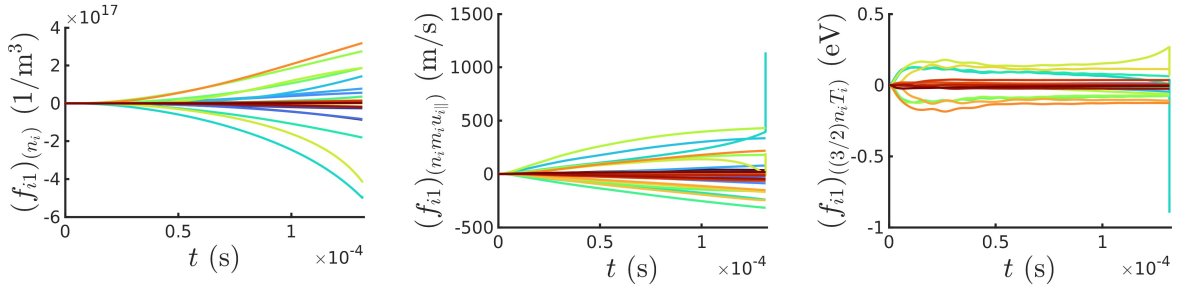

(a) Time evolution of the fluid moments of f_{i1} at a representative set of synthetic probe locations in the poloidal plane, without SFM.

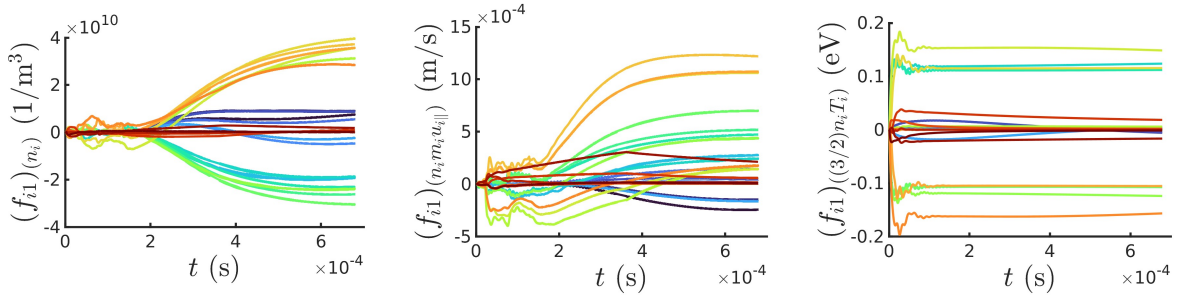

(b) Time evolution of the fluid moments of f_{i1} at a representative set of synthetic probe locations in the poloidal plane, with SFM.

Figure 6.9: Comparison of the time evolution of the fluid moments of f_{i1} at a representative set of synthetic probe locations in the poloidal plane (see Fig. 6.8) without SFM (a), and with SFM (b). The moments become of the same order as the perturbed fluid variables in (a) and crash the simulation, whereas in (b) the simulation reaches steady state, and the fluid moments of f_{i1} remain small compared to the corresponding perturbed fluid variables (see Figs. 6.7 and E.1).

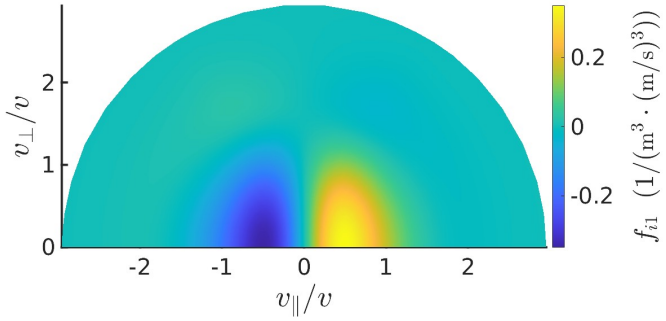

Figure 6.10: Structure of the steady-state f_{i1} (at $(R, Z) \approx (2.05\text{ m}, 0.00\text{ m})$) shows a strong $P_1(\xi)$ dependence, indicating the need for a large $q_{i\|}$ response to balance the Braginskii diamagnetic cross heat flux in the steady state.

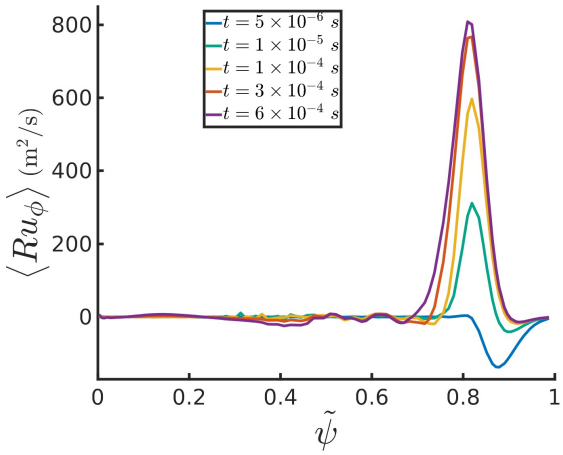

Figure 6.11: $\langle Ru_\phi \rangle$ vs. normalized poloidal flux ($\tilde{\psi}$), at a few representative times. One can see that away from the edge, $\langle Ru_\phi \rangle$ remains small throughout the time evolution.

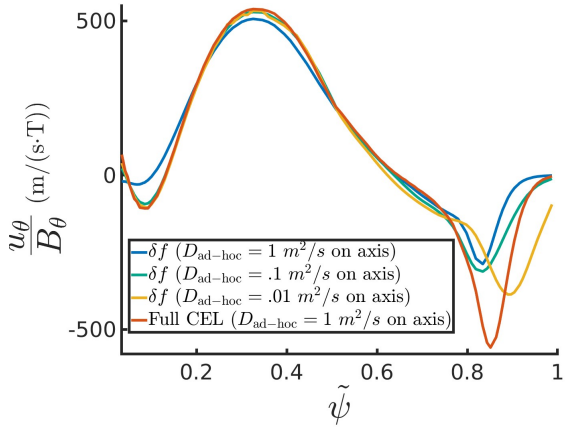

Figure 6.12: Steady-state u_θ / B_θ on the outboard midplane vs. normalized poloidal flux ($\tilde{\psi}$), compared between the fixed-background δf approach (with decreasing on-axis values for the ad-hoc diffusion coefficient) and the CEL approach. The horizontal axis is not continued to $\tilde{\psi} = 0$ where $B_\theta = 0$.

7 METHODOLOGY FOR APPLYING THE CEL CLOSURE APPROACH ALGORITHM TO GENERAL NON-AXISYMMETRIC PROBLEMS OF INTEREST IN NIMROD

Herein is discussed the methodology for applying the CEL closure approach algorithm to general non-axisymmetric problems of interest in NIMROD. Because the CEL approach is already programmed in NIMROD's framework (including the ability to extend to multiple Fourier modes in the toroidal direction by changing an input parameter), specializing to non-axisymmetric geometry is relatively straightforward. Investigation as to whether the formulation remains numerically stable in non-axisymmetric geometry is ongoing.

7.1 Implied sources in the CEL kinetic equation

Real experiments have momentum, particle, and energy sources which are not accounted for in Eqs. 3.1-3.6. Neutral beams, EM wave sources (such as RF heating sources), and interaction with impurity species can all provide additional sources of momentum, particles, and energy in the fluid equations. NIMROD often deals with these source terms in an implicit fashion by omitting (or explicitly subtracting off for some complicated terms) the initial equilibrium part from each term in the fluid equations at every time step. This assumes that the source terms are time-independent. Here, it is shown that having no implied source terms in the CEL kinetic equation (i.e., not omitting, or subtracting off, the initial equilibrium parts from any term in the kinetic equation) is consistent with all the implied sources in the fluid equations.

The implied source terms in the number density, flow, and ion temperature equations are here defined as $S_{n_e,\mathrm{eq}}$, $\mathbf{S}_{\mathbf{u},\mathrm{eq}}$, and $S_{T_i,\mathrm{eq}}$, respectively. An important distinction is made between the source terms in the fluid equations and appropriate fluid moments of a source term in the full ensemble-averaged kinetic equation (Eq. (2.3)), S_{kin}. The fluid moments of S_{kin} are defined as $(S_{\mathrm{kin}})_{n_i}$, $(S_{\mathrm{kin}})_{(n_i m_i \mathbf{u})}$, and $(S_{\mathrm{kin}})_{((3/2)n_i T_i)}$, where the subscript indicates the moment taken. The $(\_\_)_{(n_i)}$ and $(\_\_)_{((3/2)n_i T_i)}$ moments were defined in Eqs. (2.13) and (2.15), respectively. The $(\_\_)_{(n_i m_i \mathbf{u})}$ moment is defined as

$$(\_\_)_{(n_i m_i \mathbf{u})} = m_i \int \mathrm{d}^3 v \mathbf{v} (\_\_) \,, \tag{7.1}$$

where $\mathbf{v}$ is defined in the macroscopic flow reference frame. It can be shown that the following are true:

$$S_{n_e,\mathrm{eq}} = Z_{\mathrm{eff}}(S_{\mathrm{kin}})_{n_i} \ , \tag{7.2}$$

$$\mathbf{S}_{\mathbf{u},\mathrm{eq}} = (S_{\mathrm{kin}})_{(n_i m_i \mathbf{u})} \ , \tag{7.3}$$

and

$$S_{T_i,\mathrm{eq}} = (S_{\mathrm{kin}})_{((3/2)n_i T_i)} - \frac{3}{2} T_i (S_{\mathrm{kin}})_{n_i} \ . \tag{7.4}$$

The source term in the kinetic equation can be defined in a way to ensure consistency with all implied source terms in the fluid equations. One way to define S_{kin} to achieve this consistency is:

$$\begin{aligned} S_{\mathrm{kin}} =& \frac{1}{v_{Ti}^3 \pi^{3/2}} e^{-s^2} \left(\frac{S_{n_e,\mathrm{eq}}}{Z_{\mathrm{eff}}} + \frac{1}{T_i} \left(\mathbf{v} \cdot \mathbf{S}_{\mathbf{u},\mathrm{eq}} \right) + \frac{2}{3T_i} \left(s^2 - \frac{3}{2} \right) S_{T_i,\mathrm{eq}} \right) \\ =& \frac{1}{v_{Ti}^3 \pi^{3/2}} e^{-s^2} \left(\left(\frac{5}{2} - s^2 \right) (S_{\mathrm{kin}})_{n_i} + \frac{1}{T_i} \left(\mathbf{v} \cdot (S_{\mathrm{kin}})_{(n_i m_i \mathbf{u})} \right) + \frac{2}{3T_i} \left(s^2 - \frac{3}{2} \right) (S_{\mathrm{kin}})_{((3/2)n_i T_i)} \right) \ . \end{aligned} \tag{7.5}$$

This form for S_{kin} assures that the correct implied source terms appear in the number density, flow, and ion temperature equations after appropriate fluid moments are taken. This definition also allows $(S_{\mathrm{kin}})_{((3/2)n_i T_i)}$ to be negative or positive, which is a freedom that would not be allowed if S_{kin} was instead defined to be a Maxwellian evaluated with the appropriate fluid moment source terms (as a Maxwellian parameterized by a negative temperature is undefined).

S_{kin} is the source term that will appear in the full ensemble-averaged kinetic equation (Eq. (2.3)). To see the form that will potentially appear in the CEL δf kinetic equation, the steps in Ref. [61] are followed, but with the added source term now included. An important needed assumption is that all of the implied fluid source terms are $O(\delta)$, which holds away from the edge of the domain where diffusion shaping may be large. Under this assumption, it is then seen that only the gyro-average of S_{kin} is needed in the CEL kinetic equation. Including the gyro-average of S_{kin} in the CEL kinetic equation, and including all the implied source terms from the fluid equations, gives:

$$\frac{\partial f_{i1}}{\partial t}+\xi s v_{Ti}\mathbf{b}\cdot\nabla f_{i1}-\frac{1-\xi^2}{2\xi}\left[\xi s v_{Ti}\left(\mathbf{b}\cdot\nabla\ln B-\frac{\mathbf{b}\cdot\nabla\ln n_i}{s^2}\right)\right]\frac{\partial f_{i1}}{\partial\xi}$$
$$+\left[\frac{\xi v_{Ti}}{2}\left(\mathbf{b}\cdot\nabla\ln n_i-s^2\mathbf{b}\cdot\nabla\ln T_i\right)-\frac{s}{2}\frac{\partial\ln T_i}{\partial t}\right]\frac{\partial f_{i1}}{\partial s}-C_{ii}\left(f_{i1},f_{Mi}\right)-C_{ii}\left(f_{Mi},f_{i1}\right)=$$
$$\langle S_{\rm kin}\rangle_{\rm gyro}+\left\{\frac{\xi s v_{Ti}}{T_i}\left(\frac{5}{2}-s^2\right)\mathbf{b}\cdot\nabla T_i-\frac{S_{n_e,\rm eq}}{Z_{\rm eff}n_i}+\frac{\xi s v_{Ti}}{n_iT_i}\left[\frac{2}{3}\mathbf{b}\cdot\nabla\pi_{i\parallel}-\pi_{i\parallel}\mathbf{b}\cdot\nabla\ln B-\left(\mathbf{b}\cdot\mathbf{S}_{\mathbf{u},\rm eq}\right)\right]\right.$$
$$+P_2(\xi)\frac{2}{3}s^2\left(\nabla\cdot\mathbf{u}_i-3\mathbf{b}\cdot\left[\mathbf{b}\cdot\nabla\mathbf{u}_i\right]\right)$$
$$+\frac{2}{3n_iT_i}\left(s^2-\frac{3}{2}\right)\left(\nabla\cdot\left(q_{i\parallel}\mathbf{b}\right)-S_{T_i,\rm eq}\right)+\left[-\frac{2}{3}s^2P_2\left(\xi\right)\left(\left(s^2-\frac{5}{2}\right)\left(2\boldsymbol{\kappa}-\nabla\ln B\right)+\nabla\ln n_i\right)-\right.$$
$$\left.\left.\frac{4}{3}\left(\frac{1}{2}s^4-\frac{5}{2}s^2+\frac{15}{8}\right)\left(\boldsymbol{\kappa}+\nabla\ln B\right)\right]\cdot\left(\frac{\nabla T_i\times\mathbf{b}}{Z_{\rm eff}eB}\right)\right\}f_{Mi}+\nabla\cdot D_{f_{i1}}\nabla f_{i1}\,, \tag{7.6}$$

where

$$\langle S_{\rm kin}\rangle_{\rm gyro}=\frac{1}{v_{Ti}^3\pi^{3/2}}e^{-s^2}\left(\frac{S_{n_e,\rm eq}}{Z_{\rm eff}}+\frac{\xi s v_{Ti}}{T_i}\left(\mathbf{b}\cdot\mathbf{S}_{\mathbf{u},\rm eq}\right)+\frac{2}{3T_i}\left(s^2-\frac{3}{2}\right)S_{T_i,\rm eq}\right)\,. \tag{7.7}$$

From Eqs. 7.6 and 7.7, one can see that the implied source terms from the fluid equations exactly cancel the gyro-averaged source term in the CEL kinetic equation. So including no implied source terms in the CEL kinetic equation is consistent with the implied sources in the fluid equations.

Although including no source terms in the kinetic equation is consistent with the implied source terms in the fluid equations, certain physical phenomena (such as RF wave heating [23] and beam heating) may still require a source term in the CEL kinetic equation. Moments of this source term appearing on the RHS of the kinetic equation may not exactly cancel the source term itself. The problem of what source term might need to be included for modeling real physical phenomena is left to future work. It is noted that an experimental measurement of the initial equilibrium non-Maxwellian would allow sources to be treated in an implicit fashion in exactly the same manner as in NIMROD's fluid equations.

7.2 Methodology for obtaining the equilibrium f_{i1} for use in NIMROD calculations

If implicit sources are assumed in the fluid equations, the initial equilibrium values of all quantities in the fluid equations (including kinetic equilibrium quantities – such as the equilibrium $q_{i\|}$ or $\pi_{i\|}$) are needed. Therefore, the initial equilibrium f_{i1} is needed when implicit sources are assumed in the fluid equations.

As was seen in Ch. 6, the equilibrium f_{i1} is, generally speaking, non-zero. One reason this is true is that a non-zero parallel heat flux is needed to balance the Braginskii diamagnetic cross heat flux in the steady state. The simplest way to obtain the initial equilibrium f_{i1}, short of experimental measurement, is to evolve the CEL kinetic equation (with no implied sources, and possibly, an explicit, time-independent source term) to steady state while holding the fluid variables and magnetic field fixed. Once the equilibrium f_{i1} is obtained, the equilibrium $q_{i\|}$ and $\pi_{i\|}$ are computed. With all initial kinetic equilibrium quantities now obtained, and with initial fluid equilibrium quantities specified through other means, such as experimental measurement, the equilibrium is then perturbed at $t = 0$ (this perturbation can be gradual, such as a gradual increase in a time-evolving RMP beginning at $t = 0$). The fluid and magnetic field equations (with implied sources) are then evolved self-consistently with the kinetic equation (with no implied sources, and possibly, an explicit, time-independent source term) using Algorithm 1.

This procedure did not need to be followed for the results in previous chapters, because no implied sources were assumed in the fluid equations therein, hence no need to keep track of initial kinetic equilibrium quantities – such as the equilibrium $q_{i\|}$ or $\pi_{i\|}$ – to omit or subtract them at every time step.

7.3 Importance of grid packing when applying a 3D rotating RMP to the plasma

At sufficiently low resistivity, numerical stability when applying a time-evolving, rotating RMP to the plasma (via a time-evolving boundary condition applied to the magnetic field, in the same vein as Ref. [49]) requires a sufficiently packed grid at the edge of the physical domain. This was found to be essential both for fluid-only runs and when including the kinetics. A sample numerical grid that sufficiently resolved this numerical instability for $\eta_0/\mu_0 = 8.99 \times 10^{-3}$ m^2/s is shown in Fig. 7.1.

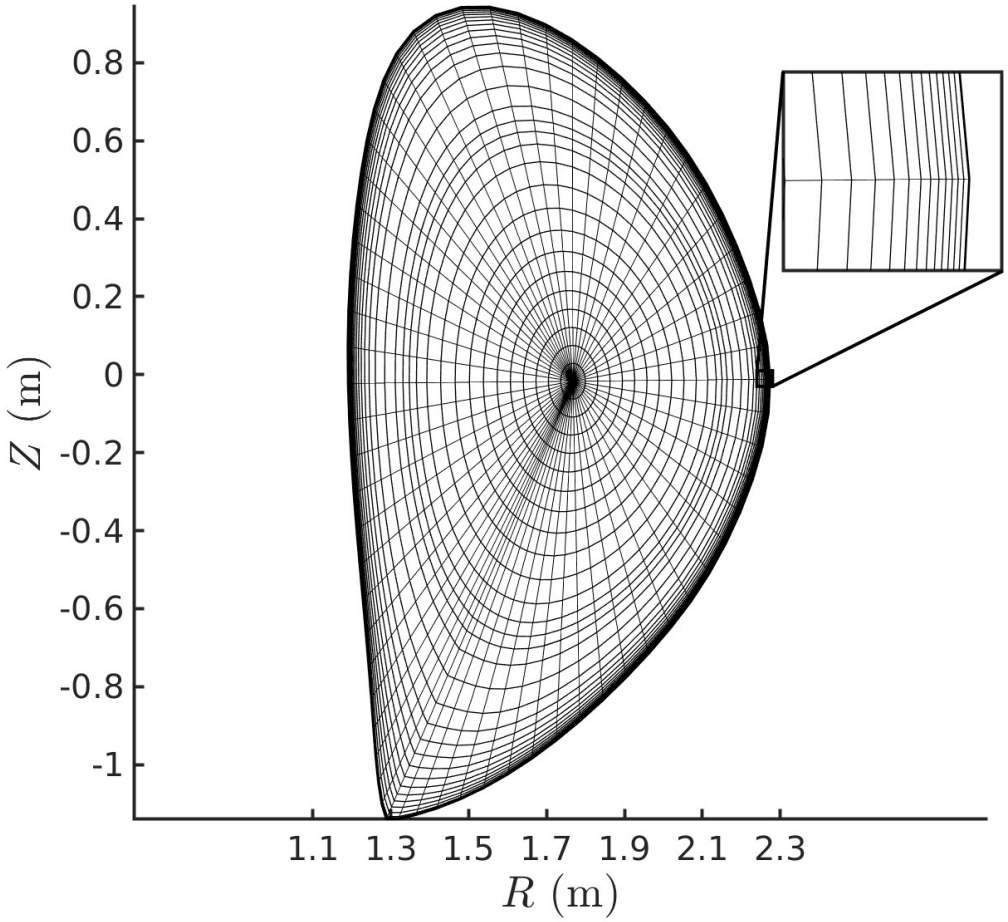

Figure 7.1: A sample numerical grid in the poloidal plane that resolved an instability associated with a time-evolving boundary condition applied to the magnetic field, which instability manifested only at sufficiently low plasma resistivity. Polynomial basis functions of degree 3 are used in each cell.

8 SUMMARY AND OUTLOOK

8.1 Summary

Herein, a numerical method for solving a Chapman-Enskog-like (CEL) continuum kinetic model for plasmas was formulated, analyzed, and applied in the plasma fluid code NIMROD. Observing the steady-state flow and flow dynamics across different tokamak configurations allowed a benchmarking of the numerical formulation. Numerical results agree well with prediction and give confidence as to the correctness of the numerical implementation.

First, the kinetic aspects of the CEL approach were benchmarked. Results for the poloidal flow coefficient α were compared between the different NIMROD kinetic formulations, analytics, and DK4D in various collisionality regimes. An exact trapped-passing grid was found to be essential for convergence when in the banana collisionality regime. It was also seen that the standard neoclassical formula for the poloidal flow coefficient in the banana regime (Eq. (4.6)) can be further refined to give better agreement with NIMROD's computational results. In particular, using Taguchi's refined analytic formula for α (Eq. (4.7)) reduced the discrepancy between NIMROD's numerical results and analytics to less than 5%.

A von Neumann stability analysis of the linearized fluid-kinetic system was also performed. It was found that centering the heat flux at the beginning of the time step and the ion temperature at the end of the time step in the kinetic equation allows for a numerically-stable time advance of the coupled system. In addition, it was shown that it is possible to eliminate both the numerical damping and the numerical growth from the linear modes. It was also found that it is not possible to achieve numerical stability if there are no constraints on the fluid moments of f_{i1}. The strategy implemented herein involved adding terms from the evolution equations for the fluid moments of f_{i1} to the RHS of the kinetic equation, in such a way as to cancel sources of numerical growth of those moments in the kinetic equation. This analysis showed that linearly stable algorithms are possible with this method.

Finally, an axisymmetric benchmark of the full CEL approach was performed. The fluid and kinetic equations were evolved fully non-linearly and self-consistently according to Algorithm 1 until the flow was in steady state. The flow dynamics and steady-state flow were then compared with prediction. The time dynamics of both the toroidal and poloidal flows were found to agree with analytical predictions. That the fluid variables remained close to equilibrium over the flow evolution also facilitated a comparison with a previously benchmarked, fixed-background δf calculation of the steady-state poloidal flow. The steady-state poloidal flow from the CEL approach was found to agree well with the fixed-background δf result. Suppression of the fluid moments of f_{i1} was seen to be essential in enabling a numerically stable evolution to steady-state.

The methodology for applying the CEL closure approach algorithm to general non-axisymmetric

problems of interest in NIMROD was also discussed. Because the CEL approach is already programmed in NIMROD's framework, specializing to non-axisymmetric geometry is relatively straightforward. Investigation as to whether the formulation remains numerically stable in non-axisymmetric geometry is ongoing. Having no implied source terms in the CEL kinetic equation was shown to be consistent with having implied source terms in the fluid equations. The problem of what explicit source term might need to be included in the kinetic equation for modeling real physical phenomena is left to future work.

8.2 Outlook

The results presented herein related to the CEL closure approach in NIMROD are positive. The most immediate pressing needs are for numerical stability considerations to be addressed when extending to non-axisymmetric geometry. Of particular concern is the possibility of aliasing instabilities, which may occur due to the ion temperature being raised to non-integer powers in the kinetic equation. The numerical stability of the model when including the electron kinetic equation (which is implemented) also needs to be addressed.

Two physical problems of immediate particular interest are that of forced magnetic reconnection in realistic tokamak geometries, and NTM dynamics in tokamaks (see Secs. 1.5.2 and 1.5.3). Both problems have been previously addressed in NIMROD using simplified models. In Ref. [48], the problem of forced magnetic reconnection was addressed by applying a time-dependent magnetic boundary condition to a sheared slab magnetic configuration in NIMROD, utilizing a heuristic closure for the ion viscous stress tensor. In Ref. [49], NTM dynamics were modeled in NIMROD by applying a rotating, time-evolving RMP to an equilibrium based on a kinetic reconstruction of DIII-D ITER Baseline Scenario (IBS) discharge 174446 at 3390 ms. Heuristic closures for both the electron and ion viscous stress tensors and the electron collisional friction force were also used. It is anticipated that interesting new insights will be obtained by simulating both of these physical phenomena in NIMROD using the CEL closure approach method outlined herein.

A EQS. (5.1)-(5.10) IN MORE GENERAL FORM

Here, Eqs. (5.1)-(5.10) are modified to include additional arbitrary centerings. The equilibrium f_{i1} is also allowed to be non-zero.

$$m_i n_{i0}\left(\frac{\Delta u_{1kx}}{\Delta t}+\theta_{u1}\mathbf{u}_0\cdot\hat{\mathbf{k}}ik\Delta u_{1kx}\right)-\Delta t C_0(-k^2)\left(\frac{B_0^2}{\mu_0}(cs)^2\Delta u_{1kx}\right)=-m_i n_{i0}\mathbf{u}_0\cdot\hat{\mathbf{k}}iku^j_{1kx}$$
$$+\frac{B_0}{\mu_0}ik(cs)B^{j+1/2}_{1kx}+\frac{\pi_{i\|0}}{B_0}ik(cs)(-B^{j+1/2}_{1kx})\,, \tag{A.1}$$

$$m_i n_{i0}\left(\frac{\Delta u_{1ky}}{\Delta t}+\theta_{u1}\mathbf{u}_0\cdot\hat{\mathbf{k}}ik\Delta u_{1ky}\right)-\Delta t C_0(-k^2)\left(\frac{B_0^2}{\mu_0}\left(-(cs)(sn)\Delta u_{1kz}+(sn)^2\Delta u_{1ky}\right)\right.$$
$$\left.+\frac{5}{3}\left(n_{i0}T_{i0}+n_{e0}T_{e0}\right)\Delta u_{1ky}\right)=-m_i n_{i0}\mathbf{u}_0\cdot\hat{\mathbf{k}}iku^j_{1ky}-\frac{B_0}{\mu_0}ik(sn)B^{j+1/2}_{1kz}$$
$$-ik\left(n_{i0}T^{j+1/2}_{i1k}+T_{i0}n^{j+1/2}_{i1k}+n_{e0}T^{j+1/2}_{e1k}+T_{e0}n^{j+1/2}_{e1k}\right)+\frac{1}{3}ik\pi_{i\|}((f^*_{i1})_{1k},T_{i0})$$
$$-(cs)^2ik\pi_{i\|}((f^*_{i1})_{1k},T_{i0})+\frac{5}{2}\frac{\pi_{i\|0}}{T_{i0}}\left(-(cs)^2ikT^{j+1/2}_{i1k}\right)$$
$$+\frac{\pi_{i\|0}}{B_0}ik(cs)((sn)((cs)B^{j+1/2}_{1kz}-(sn)B^{j+1/2}_{1ky}))$$
$$+\frac{\pi_{i\|0}}{B_0}ik(cs)((cs)((cs)B^{j+1/2}_{1ky}+(sn)B^{j+1/2}_{1kz}))\,, \tag{A.2}$$

$$m_i n_{i0}\left(\frac{\Delta u_{1kz}}{\Delta t}+\theta_{u1}\mathbf{u}_0\cdot\hat{\mathbf{k}}ik\Delta u_{1kz}\right)-\Delta tC_0(-k^2)\left(\frac{B_0^2}{\mu_0}\left((cs)^2\Delta u_{1kz}-(cs)(sn)\Delta u_{1ky}\right)\right)$$
$$=-m_i n_{i0}\mathbf{u}_0\cdot\hat{\mathbf{k}}iku_{1kz}^{j}+\frac{B_0}{\mu_0}ik(cs)B_{1kz}^{j+1/2}-(cs)(sn)ik\pi_{i\|}((f_{i1}^{*})_{1k},T_{i0})$$
$$+\frac{5}{2}\frac{\pi_{i\|0}}{T_{i0}}\left(-(cs)(sn)ikT_{i1k}^{j+1/2}\right)+\frac{\pi_{i\|0}}{B_0}ik(cs)(-(cs)((cs)B_{1kz}^{j+1/2}-(sn)B_{1ky}^{j+1/2}))$$
$$+\frac{\pi_{i\|0}}{B_0}ik(cs)((sn)((cs)B_{1ky}^{j+1/2}+(sn)B_{1kz}^{j+1/2}))\,, \tag{A.3}$$

$$\frac{\Delta n_{e1k}}{\Delta t}+\theta_{n1}(\mathbf{u}_0\cdot\hat{\mathbf{k}})ik\Delta n_{e1k}=-(\mathbf{u}_0\cdot\hat{\mathbf{k}})ikn_{e1k}^{j+1/2}-n_{e0}iku_{1ky}^{j+1}\,, \tag{A.4}$$

$$\frac{3}{2}n_{i0}\left(\frac{\Delta T_{i1k}}{\Delta t}+\theta_{T_i1}(\mathbf{u}_0\cdot\hat{\mathbf{k}})ik\Delta T_{i1k}\right)+(\theta_{T_i2})3\frac{q_{i\|0}}{T_{i0}}ik(cs)\Delta T_{i1k}=-\frac{3}{2}n_{i0}(\mathbf{u}_0\cdot\hat{\mathbf{k}})ikT_{i1k}^{j+1/2}$$
$$-n_{i0}T_{i0}iku_{1ky}^{j+1}-ik(cs)q_{i\|}((f_{i1}^{**})_{1k},T_{i0})+\frac{q_{i\|0}}{B_0}ik(cs)((cs)B_{1ky}^{j+1/2}+(sn)B_{1kz}^{j+1/2})$$
$$-3\frac{q_{i\|0}}{T_{i0}}ik(cs)T_{i1k}^{j+1/2}\,, \tag{A.5}$$

$$\frac{3}{2}n_{e0}\left(\frac{\Delta T_{e1k}}{\Delta t}+\theta_{T_e1}(\mathbf{u}_0\cdot\hat{\mathbf{k}})ik\Delta T_{e1k}\right)=-\frac{3}{2}n_{e0}(\mathbf{u}_0\cdot\hat{\mathbf{k}})ikT_{e1k}^{j+1/2}-n_{e0}T_{i0}iku_{1ky}^{j+1}\,, \tag{A.6}$$

$$\frac{\Delta B_{1kx}}{\Delta t}+\theta_{B1}(\mathbf{u}_0\cdot\hat{\mathbf{k}})ik\Delta B_{1kx}+\theta_{B2}\frac{\eta}{\mu_0}k^2\Delta B_{1kx}=B_0ik(cs)u_{1kx}^{j+1}-(\mathbf{u}_0\cdot\hat{\mathbf{k}})ikB_{1kx}^{j+1/2}$$
$$-\frac{\eta}{\mu_0}k^2B_{1kx}^{j+1/2}\,, \tag{A.7}$$

$$\frac{\Delta B_{1ky}}{\Delta t} + \theta_{B1}(\mathbf{u}_0 \cdot \hat{\mathbf{k}})ik\Delta B_{1ky} + \theta_{B2}\frac{\eta}{\mu_0}k^2\Delta B_{1ky} = -(\mathbf{u}_0 \cdot \hat{\mathbf{k}})ikB_{1ky}^{j+1/2} - \frac{\eta}{\mu_0}k^2 B_{1ky}^{j+1/2}\,, \tag{A.8}$$

$$\begin{aligned}\frac{\Delta B_{1kz}}{\Delta t} + \theta_{B1}(\mathbf{u}_0 \cdot \hat{\mathbf{k}})ik\Delta B_{1kz} + \theta_{B2}\frac{\eta}{\mu_0}k^2\Delta B_{1kz} &= -B_0 ik(sn)u_{1ky}^{j+1} + B_0 ik(cs)u_{1kz}^{j+1} \\ &- (\mathbf{u}_0 \cdot \hat{\mathbf{k}})ikB_{1kz}^{j+1/2} - \frac{\eta}{\mu_0}k^2 B_{1kz}^{j+1/2}\,,\end{aligned} \tag{A.9}$$

$$
\begin{aligned}
&\frac{\Delta(f_{i1})_{1k}}{\Delta t} + \theta_{f1} ik(cs)\xi s v_{Ti0}(\Delta f_{i1})_{1k} - \theta_{C_{ii}1} C_{ii}((\Delta f_{i1})_{1k}, f_{Mi0}) - \theta_{C_{ii}2} C_{ii}(f_{Mi0}, (\Delta f_{i1})_{1k}) \\
&\quad - \left\{ \theta_{f2} \frac{\xi s v_{Ti0}}{n_{i0} T_{i0}} \left[\frac{2}{3} ik(cs) \pi_{i\|}((\Delta f_{i1})_{1k}, T_{i0}) \right] \right. \\
&\quad \left. + \theta_{q_{i\|}} \frac{2}{3 n_{i0} T_{i0}} \left(s^2 - \frac{3}{2} \right) ik(cs) q_{i\|}((\Delta f_{i1})_{1k}, T_{i0}) \right\} f_{Mi0} \\
&= - \left\{ -\frac{(1-\xi^2)}{2\xi} \left[\xi s v_{Ti0} ik(cs) \left(\frac{(cs) B^*_{1ky} + (sn) B^*_{1kx}}{B_0} - \frac{n^*_{i1k}}{n_{i0} s^2} \right) \right] \frac{\partial (f_{i1})_0}{\partial \xi} \right. \\
&\quad \left. + \left[\frac{\xi v_{Ti0} ik(cs)}{2} \left(\frac{n^*_{i1k}}{n_{i0}} - \frac{s^2 T^*_{i1k}}{T_{i0}} \right) - \frac{s}{2 T_{i0}} \frac{\Delta T_{i1k}}{\Delta t} \right] \frac{\partial (f_{i1})_0}{\partial s} \right\} + C_{ii}((f^{j+1/2}_{i1})_{1k}, f_{Mi0}) \\
&\quad + C_{ii}(f_{Mi0}, (f^{j+1/2}_{i1})_{1k}) - ik(cs) \xi s v_{Ti0} (f^{j+1/2}_{i1})_{1k} + \left\{ \frac{\xi s v_{Ti0}}{T_i} ik(cs) T^*_{i1k} \left(\frac{5}{2} - s^2 \right) \right. \\
&\quad \left. + \frac{\xi s v_{Ti0} ik(cs)}{n_{i0} T_{i0}} \left[\frac{2}{3} \pi_{i\|}((f^{j+1/2}_{i1})_{1k}, T_{i0}) + \frac{5}{3} \frac{\pi_{i\|0}}{T_{i0}} T^*_{i1k} - \pi_{i\|0} \frac{(cs) B^*_{1ky} + (sn) B^*_{1kx}}{B_0} \right] \right. \\
&\quad + P_2(\xi) \frac{2}{3} s^2 \left(iku^*_{1ky} - 3ik(cs)((cs) u^*_{1ky} + (sn) u^*_{1kz}) \right) \\
&\quad + \frac{2}{3 n_{i0} T_{i0}} \left(s^2 - \frac{3}{2} \right) ik(cs) \left[q_{i\|}((f^{j+1/2}_{i1})_{1k}, T_{i0}) + \frac{3 q_{i\|0}}{T_{i0}} T^*_{i1k} \right. \\
&\quad \left. \left. - q_{i\|0} \frac{(cs) B^*_{1ky} + (sn) B^*_{1kx}}{B_0} \right] \right\} f_{Mi0} \, ,
\end{aligned}
\tag{A.10}
$$

where subscripts of 0 or 1 indicate an equilibrium quantity or perturbed quantity respectively, θ_{u1} is the time centering of the advective term in the flow equation, θ_{n1} is the time centering of the advective term in the number density equation, $\theta_{T_i 1}$ is the time centering of the advective term in the ion temperature equation, $\theta_{T_i 2}$ is the time centering of the ion temperature contribution to the heat flux term in the ion temperature equation, $\theta_{T_e 1}$ is the time centering of the advective term in the electron temperature equation, θ_{B1} is the time centering of the advective term in the magnetic field equation, θ_{B2} is the time centering of the resistive term in the magnetic field equation, $\theta_{C_{ii}1}$ is the time centering of the test particle part of the collision operator in the kinetic equation, $\theta_{C_{ii}2}$ is the time centering of the field particle part of the collision operator in the kinetic equation, θ_{f1} is the

time centering the advective term in the kinetic equation, θ_{f2} is the time centering the $\pi_{i\|}$ drive term in the kinetic equation, and quantities with $*$ or $**$ superscripts have arbitrary time centering as follows:

$$(f_{i1}^{*})_{1k} = (f_{i1}^{j+1/2})_{1k} + \theta_{fu}(\Delta f_{i1})_{1k} \ , \tag{A.11}$$

$$(f_{i1}^{**})_{1k} = (f_{i1}^{j+1/2})_{1k} + \theta_{ft}(\Delta f_{i1})_{1k} \ , \tag{A.12}$$

$$T_{i1k}^{*} = T_{i1k}^{j+1/2} + \theta_{t}(\Delta T_{i1k}) \ , \tag{A.13}$$

$$\mathbf{u}_{1k}^{*} = \mathbf{u}_{1k}^{j} + \theta_{u}(\Delta \mathbf{u}_{1k}) \ , \tag{A.14}$$

$$\mathbf{B}_{1k}^{*} = \mathbf{B}_{1k}^{j} + \theta_{B}(\Delta \mathbf{B}_{1k}) \ , \tag{A.15}$$

$$n_{i1k}^{*} = n_{i1k}^{j} + \theta_{n}(\Delta n_{i1k}) \ , \tag{A.16}$$

where θ_{fu} is the centering of $(f_{i1})_{1k}$ in the flow equation, θ_{ft} is the centering of $(f_{i1})_{1k}$ in the ion temperature equation, θ_t is the centering of the T_{i1k} in the kinetic equation, θ_u is the centering of $\mathbf{u}_{1k}$ in the kinetic equation, θ_B is the centering of $\mathbf{B}_{1k}$ in the kinetic equation, and θ_n is the centering of n_{i1k} in the kinetic equation. All centering parameters are arranged in a vector for convenience (where the centering of the heat flux drive term in the kinetic equation ($\theta_{q_{i\|}}$) is also included):

$$\boldsymbol{\theta}_{\text{full}} = \Big[\theta_{u1} \quad \theta_{n1} \quad \theta_{T_i1} \quad \theta_{T_i2} \quad \theta_{T_e1} \quad \theta_{B1} \quad \theta_{B2} \quad \theta_{C_{ii}1} \quad \theta_{C_{ii}2} \quad \theta_{q_{i\|}} \quad \theta_{f1} \quad \theta_{f2} \quad \theta_{fu} \quad \theta_{ft} \quad \theta_t \quad \theta_u \quad \theta_B \quad \theta_n\Big] \ . \tag{A.17}$$

B EQ. (5.10) WITH THE ADDITIONAL TERMS FROM FLUID MOMENT EQS.

When the terms from Eq. (5.19) are included in the linear analysis, Eq. (5.10) becomes:

$$
\begin{aligned}
&\frac{(\Delta f_{i1})_{1k}}{\Delta t} + \theta_f ik(cs)\xi s v_{Ti0}(\Delta f_{i1})_{1k} - \theta_{C_{ii}} C_{ii}((\Delta f_{i1})_{1k}, f_{Mi0}) - \theta_{C_{ii}} C_{ii}(f_{Mi0}, (\Delta f_{i1})_{1k}) \\
&\quad - \left\{ \theta_f \frac{\xi s v_{Ti0}}{n_{i0} T_{i0}} \left[\frac{2}{3} ik(cs)\pi_{i\parallel}((\Delta f_{i1})_{1k}, T_{i0}) \right] + \theta_{q_{i\parallel}} \frac{2}{3 n_{i0} T_{i0}} \left(s^2 - \frac{3}{2} \right) ik(cs) q_{i\parallel}((\Delta f_{i1})_{1k}, T_{i0}) \right. \\
&\quad + \frac{1}{n_{i0}} \left(\theta_f \frac{1}{m_i} ik(cs)((\Delta f_{i1})_{1k})_{(n_i m_i u_{i\parallel})} - \theta_{C_{ii}} (C_{ii}\,((\Delta f_{i1})_{1k}, f_{Mi0}) + C_{ii}\,(f_{Mi0}, (\Delta f_{i1})_{1k}))_{(n_i)} \right. \\
&\quad \left. - D k^2 ((\Delta f_{i1})_{1k})_{(n_i)} \right) \left(\frac{5}{2} - s^2 \right) + \frac{\xi s v_{Ti0}}{n_{i0} T_{i0}} \left(\theta_f \frac{2}{3} ik(cs)((\Delta f_{i1})_{1k})_{((3/2) n_i T_i)} \right. \\
&\quad \left. - \theta_{C_{ii}} (C_{ii}\,((\Delta f_{i1})_{1k}, f_{Mi0}) + C_{ii}\,(f_{Mi0}, (\Delta f_{i1})_{1k}))_{(n_i m_i u_{i\parallel})} - D k^2 ((\Delta f_{i1})_{1k})_{(n_i m_i u_{i\parallel})} \right) \left(\frac{7}{2} - s^2 \right) \\
&\quad + \frac{2}{3 n_{i0} T_{i0}} \left(s^2 - \frac{3}{2} \right) \left[- \theta_{C_{ii}} (C_{ii}\,((\Delta f_{i1})_{1k}, f_{Mi0}) + C_{ii}\,(f_{Mi0}, (\Delta f_{i1})_{1k}))_{((3/2) n_i T_i)} \right. \\
&\quad \left. \left. - D k^2 ((\Delta f_{i1})_{1k})_{((3/2) n_i T_i)} \right] \right\} f_{Mi0} = \; C_{ii}((f_{i1}^{j+1/2})_{1k}, f_{Mi0}) + C_{ii}(f_{Mi0}, (f_{i1}^{j+1/2})_{1k}) \\
&\quad - ik(cs)\xi s v_{Ti0} (f_{i1}^{j+1/2})_{1k} + \left\{ \frac{\xi s v_{Ti0}}{T_i} ik(cs) T^*_{i1k} \left(\frac{5}{2} - s^2 \right) + \frac{1}{n_{i0}} \left(\frac{1}{m_i} ik(cs) \left((f_{i1}^{j+1/2})_{1k} \right)_{(n_i m_i u_{i\parallel})} \right. \right. \\
&\quad \left. - \left(C_{ii}((f_{i1}^{j+1/2})_{1k}, f_{Mi0}) + C_{ii}(f_{Mi0}, (f_{i1}^{j+1/2})_{1k}) \right)_{(n_i)} - D k^2 \left((f_{i1}^{j+1/2})_{1k} \right)_{(n_i)} \right) \left(\frac{5}{2} - s^2 \right) \\
&\quad + \frac{\xi s v_{Ti0}}{n_{i0} T_{i0}} \left[\frac{2}{3} ik(cs)\pi_{i\parallel}((f_{i1}^{j+1/2})_{1k}, T_{i0}) + \left(\frac{2}{3} ik(cs) \left((f_{i1}^{j+1/2})_{1k} \right)_{((3/2) n_i T_i)} \right. \right. \\
&\quad \left. - \left(C_{ii}((f_{i1}^{j+1/2})_{1k}, f_{Mi0}) + C_{ii}(f_{Mi0}, (f_{i1}^{j+1/2})_{1k}) \right)_{(n_i m_i u_{i\parallel})} \right. \\
&\quad \left. \left. - D k^2 \left((f_{i1}^{j+1/2})_{1k} \right)_{(n_i m_i u_{i\parallel})} \right) \left(\frac{7}{2} - s^2 \right) \right] + P_2(\xi) \frac{2}{3} s^2 \left(iku^*_{1ky} - 3ik(cs)((cs)u^*_{1ky} + (sn)u^*_{1kz}) \right) \\
&\quad + \frac{2}{3 n_{i0} T_{i0}} \left(s^2 - \frac{3}{2} \right) \left[ik(cs) q_{i\parallel}((f_{i1}^{j+1/2})_{1k}, T_{i0}) - \left(C_{ii}((f_{i1}^{j+1/2})_{1k}, f_{Mi0}) \right. \right. \\
&\quad \left. \left. + C_{ii}(f_{Mi0}, (f_{i1}^{j+1/2})_{1k}) \right)_{((3/2) n_i T_i)} - D k^2 \left((f_{i1}^{j+1/2})_{1k} \right)_{((3/2) n_i T_i)} \right] \right\} f_{Mi0} \, . \qquad \text{(B.1)}
\end{aligned}
$$

C TABLES ILLUSTRATING DEPENDENCE OF THE MAXIMUM GROWTH RATES ON θ_{ft}, θ_t, AND $\theta_{q_{i\|}}$

These tables illustrate a complicated dependence of the maximum normalized growth rates on θ_{ft}, θ_t, and $\theta_{q_{i\|}}$, where each table is for a different value of θ_t. Besides the three centering parameters that are varied, it is assumed that $\theta_{fu} = 0.0$ and that $\theta_f = \theta_{C_{ii}} = \theta_u = 1.0$. $C_0 = 0.3$ is also used.

	$\theta_{q_{i\|}}$										
θ_{ft}	0.0	0.1	0.2	0.3	0.4	0.5	0.6	0.7	0.8	0.9	1.0
0.0	3.4E-16	2.8E-16	2.5E-16	2.9E-16	4.2E-16	2.0E-16	1.9E-16	6.4E-03	2.3E-02	5.0E-02	2.4E-01
0.1	3.4E-16	2.2E-16	2.4E-16	4.1E-16	3.1E-16	2.5E-16	3.9E-16	2.7E-16	1.2E-02	3.3E-02	7.6E-02
0.2	2.3E-16	2.8E-16	2.8E-16	3.4E-16	2.3E-16	3.0E-16	2.7E-16	3.1E-16	4.7E-04	1.9E-02	4.8E-02
0.3	2.0E-16	2.0E-16	2.2E-16	2.5E-16	3.2E-16	2.6E-16	3.8E-16	3.2E-16	2.7E-16	6.6E-03	2.9E-02
0.4	2.8E-16	2.5E-16	3.6E-16	1.7E-16	1.9E-16	3.3E-16	2.5E-16	2.4E-16	3.4E-16	2.3E-16	1.4E-02
0.5	2.3E-16	2.4E-16	2.5E-16	3.0E-16	2.1E-16	3.3E-16	2.6E-16	2.6E-16	3.1E-16	3.4E-16	2.1E-16
0.6	3.3E-16	1.9E-16	2.1E-16	3.2E-16	1.8E-16	4.4E-16	2.4E-16	2.7E-16	3.3E-16	3.3E-16	2.8E-16
0.7	2.9E-16	2.3E-16	2.2E-16	2.2E-16	3.0E-16	2.6E-16	2.9E-16	3.8E-16	2.1E-16	2.2E-16	1.9E-16
0.8	2.7E-16	3.3E-16	2.7E-16	2.0E-16	2.2E-16	3.2E-16	2.9E-16	2.1E-16	2.5E-16	2.6E-16	1.8E-16
0.9	2.3E-16	2.1E-16	2.1E-16	2.7E-16	2.5E-16	2.5E-16	2.6E-16	3.1E-16	2.7E-16	2.7E-16	1.9E-16
1.0	2.6E-16	2.4E-16	2.3E-16	2.0E-16	3.2E-16	2.1E-16	2.1E-16	3.6E-16	2.3E-16	2.2E-16	2.3E-16

Table C.1: Table of max normalized growth rates found over $kd_i \in [0, 40\pi]$, for $\theta_t = 1.0$. Here, a higher θ_{ft} allows for a higher $\theta_{q_{i\|}}$.

	$\theta_{q_{i\|}}$										
θ_{ft}	0.0	0.1	0.2	0.3	0.4	0.5	0.6	0.7	0.8	0.9	1.0
0.0	4.4E-04	5.0E-04	5.8E-04	6.8E-04	8.4E-04	1.1E-03	1.4E-03	2.2E-03	4.8E-03	1.4E-02	2.2E-01
0.1	3.2E-04	3.7E-04	4.2E-04	4.9E-04	5.9E-04	7.5E-04	1.0E-03	1.5E-03	2.9E-03	9.3E-03	7.6E-02
0.2	2.2E-04	2.5E-04	2.9E-04	3.3E-04	4.0E-04	4.9E-04	6.4E-04	9.4E-04	1.7E-03	5.5E-03	4.8E-02
0.3	1.3E-04	1.4E-04	1.6E-04	1.9E-04	2.2E-04	2.8E-04	3.6E-04	5.0E-04	8.4E-04	2.5E-03	2.9E-02
0.4	4.3E-05	4.9E-05	5.5E-05	6.4E-05	7.6E-05	9.3E-05	1.2E-04	1.6E-04	2.6E-04	6.4E-04	1.3E-02
0.5	2.7E-16	2.7E-16	2.2E-16	2.6E-16	2.9E-16	2.9E-16	2.7E-16	2.7E-16	2.1E-16	2.6E-16	2.2E-16
0.6	2.8E-16	3.7E-16	2.9E-16	2.5E-16	2.9E-16	2.3E-16	2.3E-16	2.2E-16	2.4E-16	2.3E-16	2.1E-16
0.7	2.7E-16	1.9E-16	3.0E-16	3.0E-16	2.8E-16	3.2E-16	2.2E-16	3.2E-16	2.1E-16	2.3E-16	2.1E-16
0.8	1.9E-16	2.4E-16	1.9E-16	3.1E-16	2.8E-16	3.0E-16	2.3E-16	2.2E-16	2.8E-16	3.2E-16	1.9E-16
0.9	4.5E-16	1.9E-16	2.3E-16	2.1E-16	2.8E-16	2.3E-16	2.6E-16	3.2E-16	3.0E-16	2.5E-16	2.2E-16
1.0	2.2E-16	3.1E-16	2.5E-16	2.7E-16	2.3E-16	2.7E-16	3.0E-16	2.0E-16	3.1E-16	1.8E-16	2.2E-16

Table C.2: Table of max normalized growth rates found over $kd_i \in [0, 40\pi]$, for $\theta_t = 0.5$. Here, only $\theta_{ft} \geq 0.5$ matters for stability.

	$\theta_{q_{i\parallel}}$										
θ_{ft}	0.0	0.1	0.2	0.3	0.4	0.5	0.6	0.7	0.8	0.9	1.0
0.0	1.2E-03	1.4E-03	2.2E-03	3.4E-03	4.9E-03	6.9E-03	9.6E-03	1.3E-02	1.9E-02	3.0E-02	1.2E-01
0.1	1.1E-03	1.2E-03	1.4E-03	1.8E-03	3.3E-03	5.2E-03	7.7E-03	1.1E-02	1.7E-02	2.7E-02	1.6E-01
0.2	9.8E-04	1.1E-03	1.2E-03	1.4E-03	1.6E-03	3.2E-03	5.6E-03	9.0E-03	1.4E-02	2.4E-02	1.9E-01
0.3	8.2E-04	9.2E-04	1.0E-03	1.2E-03	1.4E-03	1.7E-03	3.4E-03	6.6E-03	1.1E-02	2.1E-02	2.0E-01
0.4	6.4E-04	7.2E-04	8.3E-04	9.6E-04	1.1E-03	1.4E-03	1.9E-03	3.9E-03	8.3E-03	1.6E-02	2.1E-01
0.5	4.4E-04	5.0E-04	5.8E-04	6.8E-04	8.4E-04	1.1E-03	1.4E-03	2.2E-03	4.8E-03	1.4E-02	2.2E-01
0.6	2.5E-04	2.8E-04	3.3E-04	3.9E-04	4.8E-04	6.2E-04	8.6E-04	1.4E-03	3.2E-03	1.4E-02	2.3E-01
0.7	5.7E-05	6.6E-05	7.7E-05	9.4E-05	1.2E-04	1.6E-04	2.4E-04	4.4E-04	1.2E-03	2.8E-02	2.3E-01
0.8	2.9E-16	2.6E-16	2.8E-16	2.4E-16	3.3E-16	2.9E-16	3.1E-16	2.8E-16	8.0E-04	3.8E-02	2.4E-01
0.9	3.0E-16	2.5E-16	3.6E-16	2.6E-16	2.7E-16	2.1E-16	2.4E-16	2.6E-16	1.6E-02	4.5E-02	2.4E-01
1.0	2.0E-16	2.3E-16	3.7E-16	3.8E-16	2.8E-16	2.7E-16	2.4E-16	6.4E-03	2.3E-02	5.0E-02	2.4E-01

Table C.3: Table of max normalized growth rates found over $kd_i \in [0, 40\pi]$, for $\theta_t = 0.0$. Here, stability is found only for high enough θ_{ft} and low enough $\theta_{q_{i\parallel}}$.

D AN EIGENVECTOR/EIGENVALUE ANALYSIS OF ELECTRON LANDAU DAMPING IN ONE DIMENSION

Here a similar eigenvector/eigenvalue analysis as in Sec. 5 is applied to the problem of electron Landau damping in one dimension [72]. This analysis is performed to show that, when discretizing velocity space, Landau damping shows up as a decorrelation of the eigenvectors due to differing real frequencies. The discretization of velocity space is the main difference between this solution method and the one originally employed by Landau. The same equation is solved as in Landau's original work, namely:

$$\frac{\partial f_{e1}}{\partial t} + v_x \frac{\partial f_{e1}}{\partial x} - \frac{e}{m_e} E_x \frac{\partial f_{e0}}{\partial v_x} = 0 \,, \tag{D.1}$$

and

$$\frac{\partial E_x}{\partial x} = \frac{-e \int \mathrm{d}v_x f_{e1}}{\epsilon_0} \,, \tag{D.2}$$

where v_x is the one-dimensional particle velocity, E_x is the one-dimensional electric field, m_e is the electron mass, f_{e0} is the equilibrium electron distribution function, and f_{e1} is the perturbed electron distribution function.

It is assumed that f_{e0} is a one-dimensional Maxwellian for this analysis, i.e., $f_{e0} = \frac{n_{e0}}{\sqrt{\pi} v_{T_e 0}} e^{-v_x^2/v_{T_e 0}^2}$ (with $v_{T_e 0} = \sqrt{2T_{e0}/m_e}$). The equations are Fourier transformed (with $\mathbf{k} = k\hat{\mathbf{x}}$), and a collocation approach [44] is applied with regards to the normalized radial speed coordinate $v_x/v_{T_e 0}$. In this analysis, 200 collocation points in $v_x/v_{T_e 0}$ are used. f_{e1} is normalized by the electron Maxwellian at its maximum (i.e., $n_{e0}/\sqrt{\pi} v_{Te0}$) and the kinetic equation is scaled by the same quantity. Time is normalized by the electron plasma frequency ($\omega_{pe} = \sqrt{n_{e0} e^2/\epsilon_0 m_e}$) and length by the electron Debye length ($\lambda_{De} = v_{T_e 0}/(\sqrt{2}\omega_{pe})$). A small time step of $(\Delta t)\omega_{pe} \approx 5.5 \times 10^{-3}$ is used to obtain the frequencies, and a time centering of 0.5 is used for all non-time-derivative terms in Eqs. (D.1)-(D.2).

It can be seen in Fig. D.1 that there is negligible imaginary part of the frequency associated with this set of eigenmodes. However, as will be shown, damping of the perturbed number density ($\int \mathrm{d}v_x f_{e1,k}$) still occurs.

For a simple test case, it is assumed that $f_{e1,k\approx.5/\lambda_{De}} = 0.1 f_{e0}$ at $t = 0$. This initial condition is projected onto the set of eigenvectors for $(k\lambda_{De}) \approx .5$, and then each eigenvector is evolved in time using the corresponding (real) frequency. The sum of the coefficients times the time-evolved

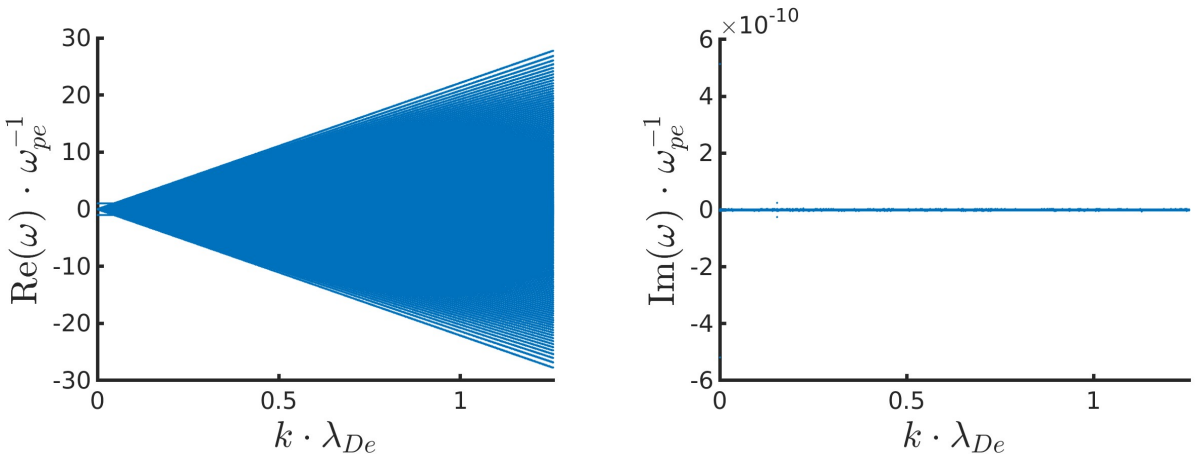

(a) Normalized $\mathrm{Re}(\omega)$ vs. normalized k

(b) Normalized $\mathrm{Im}(\omega)$ vs. normalized k

Figure D.1: Normalized $\mathrm{Re}(\omega)$ vs. normalized k on the left (a) and normalized $\mathrm{Im}(\omega)$ vs. normalized k on the right (b) is shown for the one-dimensional Landau damping problem. 200 collocation points in v_x/v_{T_e0} are used, and $(\Delta t)\omega_{pe} \approx 5.5 \times 10^{-3}$.

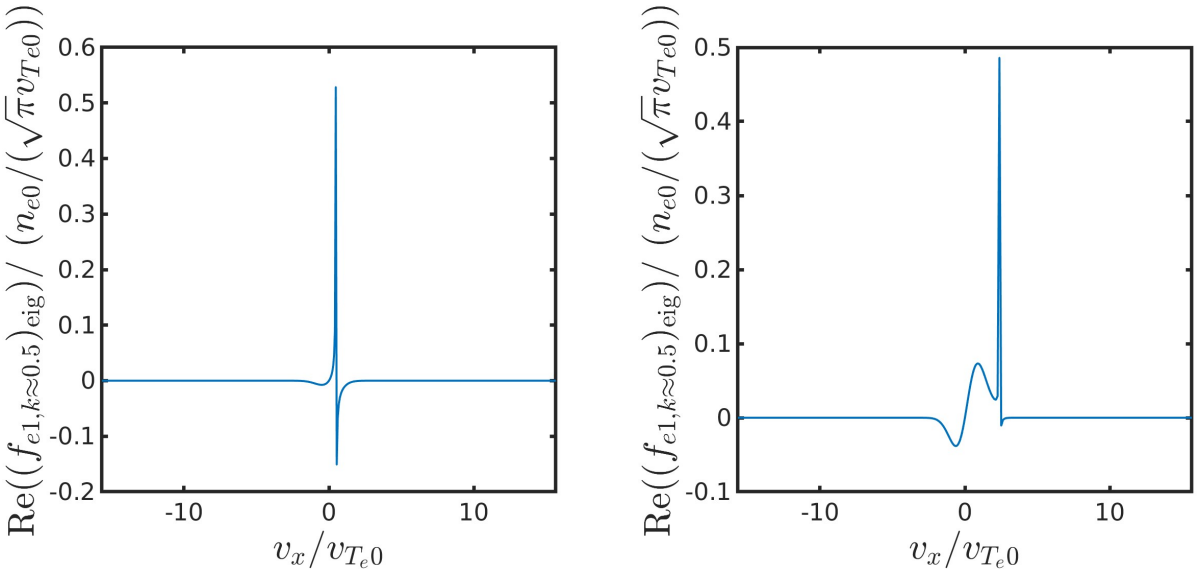

Figure D.2: The real parts of two typical eigenvectors ($(f_{e1,k\approx.5/\lambda_{De}})_{\mathrm{eig}}$) are shown. The eigenvectors for the one-dimensional Landau damping problem are peaked in a very localized portion of velocity space, and smaller elsewhere.

eigenvectors then gives $f_{e1,k\approx.5/\lambda_{De}}$ at later times. The real parts of two typical eigenvectors ($(f_{e1,k\approx.5/\lambda_{De}})_{\mathrm{eig}}$) are shown in Fig. D.2. The eigenvectors are peaked in a very localized portion of velocity space, and smaller elsewhere. This, combined with fact that each eigenvector has a different real frequency, is then equivalent to the continuous case where the longtime behavior of the distribution function is an oscillation with a velocity-space-dependent frequency of kv_x (see Ref.

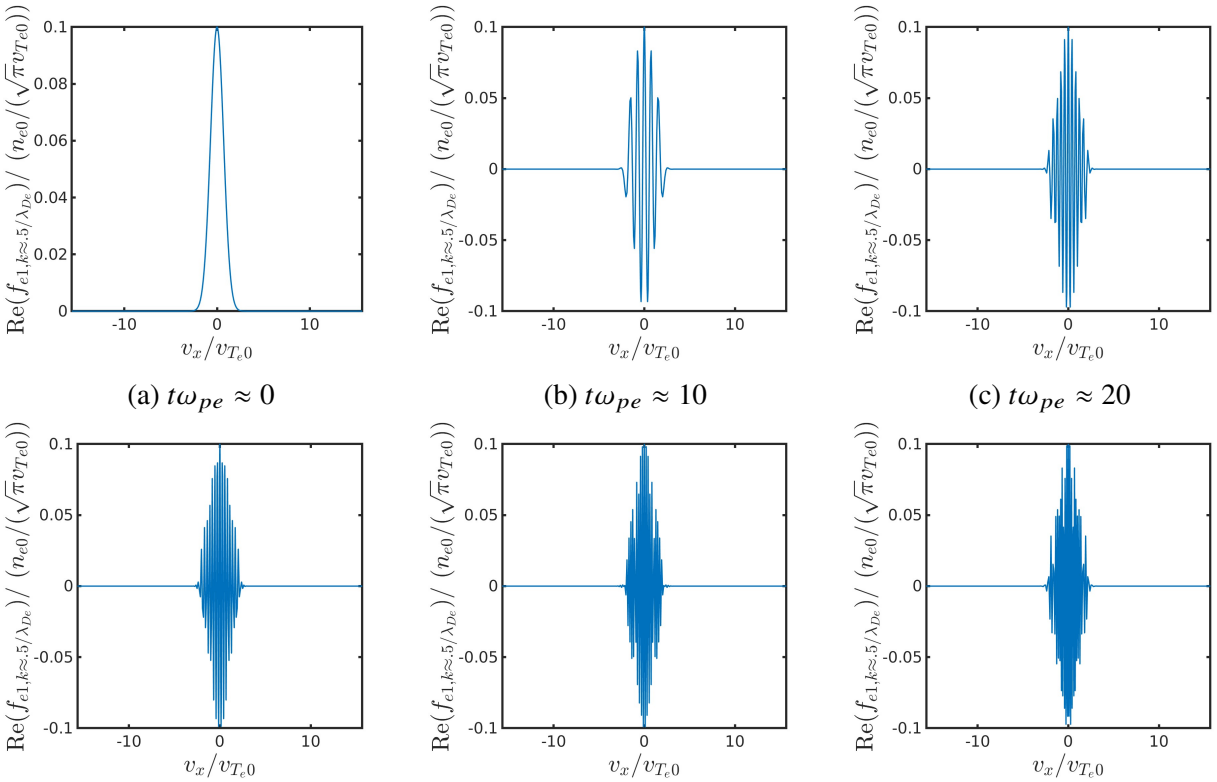

(a) $t\omega_{pe} \approx 0$ (b) $t\omega_{pe} \approx 10$ (c) $t\omega_{pe} \approx 20$

(d) $t\omega_{pe} \approx 30$ (e) $t\omega_{pe} \approx 40$ (f) $t\omega_{pe} \approx 50$

Figure D.3: The real part of $f_{e1,k\approx.5/\lambda_{De}}$, normalized to $n_{e0}/\sqrt{\pi}v_{Te0}$ is shown at successive normalized time points. The granularity of the distribution eventually approaches the limits of the velocity space resolution.

[72]). See Fig. D.3 for plots of $\mathrm{Re}(f_{e1,k\approx.5/\lambda_{De}})$ at successive time points[1]. It is seen that eventually the granularity of the distribution (caused by each part of velocity space being associated with a different frequency) approaches the limits of the velocity space resolution.

The time evolution of $\int \mathrm{d}v_x \mathrm{Re}(f_{e1,k\approx.5/\lambda_{De}})$ is compared against the $k\lambda_{De} \ll 1$ analytic formula [72, 77] in Fig D.4. As can be seen, the perturbed number density damps in time. We are not quite in the $k\lambda_{De} \ll 1$ asymptotic regime, and it is noted that the analytic formula in Refs. [72, 77] involves other significant approximations. Shortly after the granularity of the distribution approaches the limits of the velocity space resolution an echo is seen. This echo can be pushed further and further back in time by increasing the velocity space resolution, and is therefore numeric. Landau damping echos observed in real experiments may be due to particle discreteness effects becoming important after the granularity of the ensemble-averaged distribution function reaches some critical level (i.e., reaching the limit of approximating individual particles by a smooth ensemble-averaged distribution function). This conjecture, however, would need to be tested.

[1] See `https://youtu.be/jnpzmx0vpVY` for an animation of the time evolution of $\mathrm{Re}(f_{e1,k\approx.5/\lambda_{De}})$.

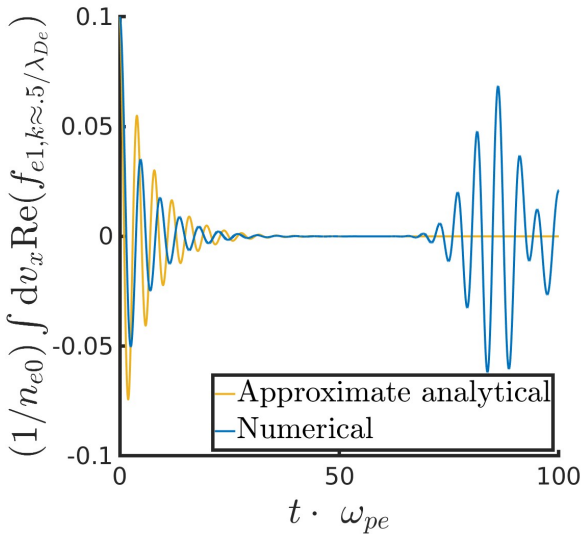

Figure D.4: The time evolution of $\int \mathrm{d}v_x \mathrm{Re}(f_{e1,k\approx.5/\lambda_{De}})$ (normalized to n_{e0}) is compared against the $k\lambda_{De} \ll 1$ analytic formula [72, 77]. We are not quite in the $k\lambda_{De} \ll 1$ asymptotic regime, and it is noted that the analytic formula in Refs. [72, 77] involves other significant approximations. Damping of $\int \mathrm{d}v_x \mathrm{Re}(f_{e1,k\approx.5/\lambda_{De}})$ is seen, as well as a (numerical) echo when the granularity of $f_{e1,k\approx.5/\lambda_{De}}$ approaches the limits of the velocity space resolution.

E TIME EVOLUTION OF ADDITIONAL PERTURBED QUANTITIES OF INTEREST WITH SFM

Here, the time evolution of additional perturbed quantities of interest (with SFM) are shown for the axisymmetric nonlinear test case of Ch. 6. The quantities of interest are plotted at a representative set of synthetic probe locations in the poloidal plane (see Fig. 6.8).

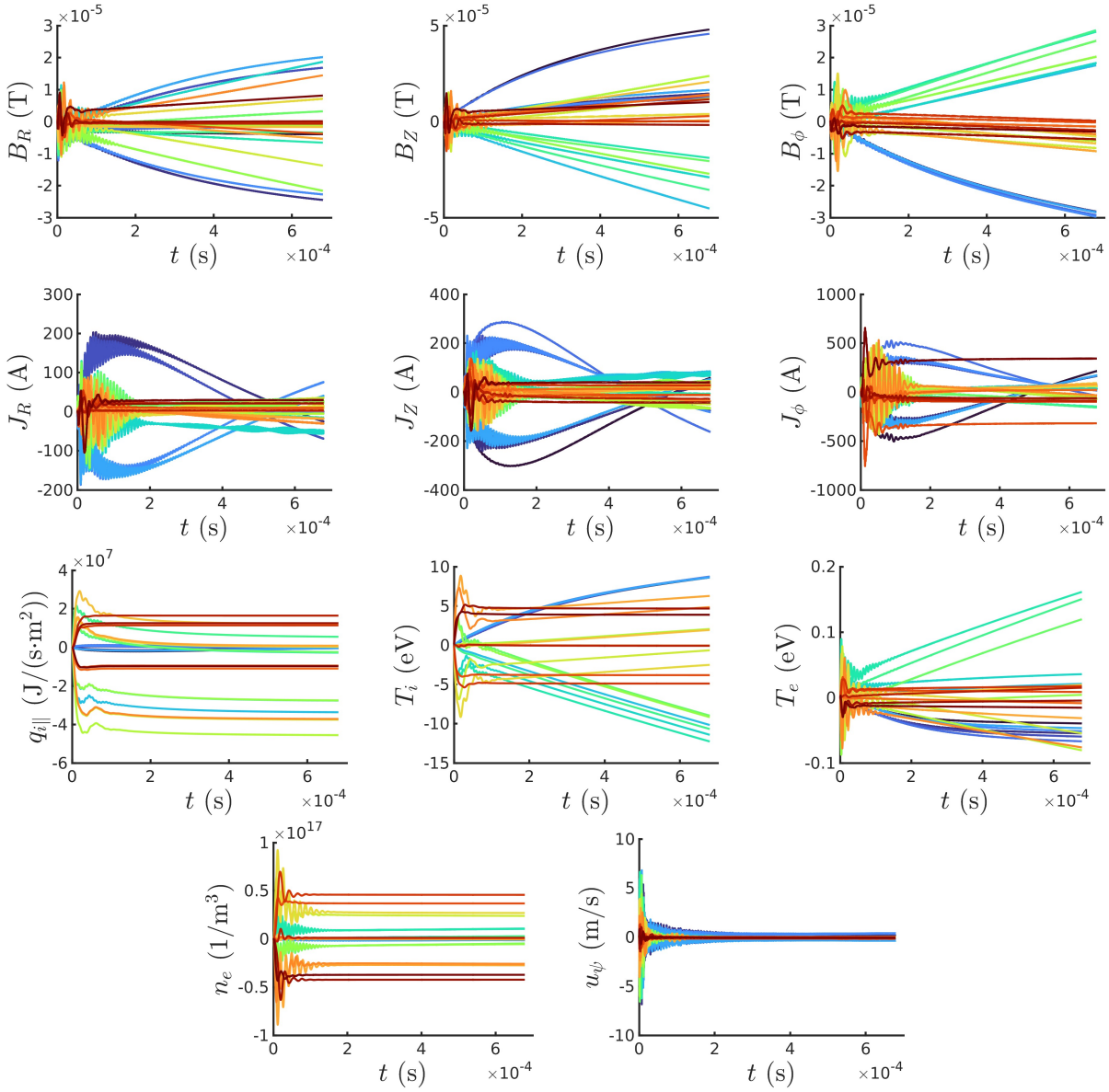

Figure E.1: Time evolution of additional perturbed quantities of interest at a representative set of synthetic probe locations in the poloidal plane (see Fig. 6.8) with SFM.

REFERENCES

[1] Statistical review of world energy, 2023. URL: https://www.energyinst.org/statistical-review.

[2] J. Wesson, Tokamaks; 3rd ed., Oxford Univ. Press, Oxford, 2004.

[3] Q.-J. Hong, A. van de Walle, Prediction of the material with highest known melting point from ab initio molecular dynamics calculations, Phys. Rev. B 92 (2015) 020104.

[4] H. Poincaré, Sur les courbes définies par les équations différentielles (iii), Journal de Mathématiques Pures et Appliquées 1 (1885) 167–244.

[5] R. D. Hazeltine, J. D. Meiss, Plasma Confinement, dover ed., Dover, Mineola, New York, 2003.

[6] The physics of fusion power, URL: https://warwick.ac.uk/fac/sci/physics/research/cfsa/people/pastmembers/peeters/teaching/lnw.pdf, accessed: 02-20-2024.

[7] Tokamak, URL: https://en.wikipedia.org/wiki/Tokamak, accessed: 02-02-2024.

[8] N. J. Fisch, Theory of current drive in plasmas, Rev. Mod. Phys. 59 (1987) 175–234.

[9] Y.-S. Na, Introduction to nuclear fusion, URL: https://ocw.snu.ac.kr/sites/default/files/NOTE/INF-2017-17-Transport1.pdf, accessed: 03-01-2024.

[10] From doughnuts to bananas, URL: https://webcache.googleusercontent.com/search?q=cache:iZBThVYhK7EJ:https://www.euro-fusion.org/de/news/detail/detail/News/from-doughnuts-to-bananas/+&cd=1&hl=en&ct=clnk&gl=us, accessed: 2020-12-02.

[11] A. S. Richardson, NRL Plasma Formulary, Naval Research Laboratory, 2019.

[12] S. I. Braginskii, Transport Processes in a Plasma, Reviews of Plasma Physics 1 (1965) 205.

[13] L. Spitzer, R. Härm, Transport Phenomena in a Completely Ionized Gas, Phys. Rev. 89 (1953) 977–981.

[14] L. Spitzer, Physics of Fully Ionized Gases, 2nd ed., Interscience, 1962.

[15] E. M. Epperlein, M. G. Haines, Plasma transport coefficients in a magnetic field by direct numerical solution of the Fokker–Planck equation, The Physics of Fluids 29 (1986) 1029–1041.

[16] J.-Y. Ji, E. D. Held, Closure and transport theory for high-collisionality electron-ion plasmas, Phys. Plasmas 20 (2013) 042114.

[17] A. A. Galeev, R. Z. Sagdeev, Transport phenomena in a collisionless plasma in a toroidal magnetic system, JETP 26 (1968) 233.

[18] S. P. Hirshman, D. J. Sigmar, Neoclassical transport of impurities in tokamak plasmas, Nuclear Fusion 21 (1981) 1079.

[19] P. Helander, D. J. Sigmar, Collisional Transport in Magnetized Plasmas, Cambridge University Press, New York, 2002.

[20] M. Taguchi, Analytic expression for poloidal flow velocity in the banana regime, Phys. Plasmas 20 (2013) 014505.

[21] K. C. Shaing, D. A. Spong, Extending the collisional fluid equations into the long mean-free-path regime in toroidal plasmas. I. Plasma viscosity, Physics of Fluids B: Plasma Physics 2 (1990) 1190–1194.

[22] J. P. Wang, J. D. Callen, Fluid/kinetic hybrid moment description of plasmas via a Chapman–Enskog-like approach, Physics of Fluids B: Plasma Physics 4 (1992) 1139–1151.

[23] J. J. Ramos, Fluid and drift-kinetic description of a magnetized plasma with low collisionality and slow dynamics orderings. I. Electron theory, Phys. Plasmas 17 (2010) 082502.

[24] R. C. Morris, M. G. Haines, R. J. Hastie, The neoclassical theory of poloidal flow damping in a tokamak, Phys. Plasmas 3 (1996) 4513–4520.

[25] F. L. Hinton, M. N. Rosenbluth, Dynamics of axisymmetric and poloidal flows in tokamaks, Plasma Physics and Controlled Fusion 41 (1999) A653.

[26] G. R. Tynan, I. Cziegler, P. H. Diamond, M. Malkov, A. Hubbard, J. W. Hughes, J. L. Terry, J. H. Irby, Recent progress towards a physics-based understanding of the H-mode transition, Plasma Physics and Controlled Fusion 58 (2016) 044003.

[27] L. Schmitz, The role of turbulence–flow interactions in L- to H-mode transition dynamics: recent progress, Nuclear Fusion 57 (2017) 025003.

[28] A. W. Leonard, Edge-localized-modes in tokamaks), Phys. Plasmas 21 (2014) 090501.

[29] P. Lang, A. Loarte, G. Saibene, L. Baylor, M. Becoulet, M. Cavinato, S. Clement-Lorenzo, E. Daly, T. Evans, M. Fenstermacher, Y. Gribov, L. Horton, C. Lowry, Y. Martin, O. Neubauer, N. Oyama, M. Schaffer, D. Stork, W. Suttrop, P. Thomas, M. Tran, H. Wilson, A. Kavin, O. Schmitz, ELM control strategies and tools: status and potential for ITER, Nuclear Fusion 53 (2013) 043004.

[30] M. Wade, R. Nazikian, J. deGrassie, T. Evans, N. Ferraro, R. Moyer, D. Orlov, R. Buttery, M. Fenstermacher, A. Garofalo, M. Lanctot, G. McKee, T. Osborne, M. Shafer, W. Solomon, P. Snyder, W. Suttrop, A. Wingen, E. Unterberg, L. Zeng, Advances in the physics understanding of ELM suppression using resonant magnetic perturbations in DIII-D, Nuclear Fusion 55 (2015) 023002.

[31] R. Nazikian, Q. Hu, A. Ashourvan, D. Eldon, T. Evans, B. Grierson, N. Logan, D. Orlov, J.-K. Park, C. Paz-Soldan, F. Poli, Q. Yu, Pedestal collapse by resonant magnetic perturbations, Nuclear Fusion 61 (2021) 044001.

[32] Q. M. Hu, R. Nazikian, N. C. Logan, J.-K. Park, C. Paz-Soldan, S. M. Yang, B. A. Grierson, Y. In, Y. M. Jeon, M. Kim, S. K. Kim, D. M. Orlov, G. Y. Park, Q. Yu, Predicting operational windows of ELMs suppression by resonant magnetic perturbations in the DIII-D and KSTAR tokamaks, Phys. Plasmas 28 (2021) 052505.

[33] R. J. La Haye, Neoclassical tearing modes and their control, Phys. Plasmas 13 (2006) 055501.

[34] P.C. de Vries and M.F. Johnson and B. Alper and P. Buratti and T.C. Hender and H.R. Koslowski and V. Riccardo and JET-EFDA Contributors, Survey of disruption causes at JET, Nuclear Fusion 51 (2011) 053018.

[35] What is Iter?, URL: `https://www.iter.org/proj/inafewlines`, accessed: 2024-03-15.

[36] C. Sovinec, A. Glasser, T. Gianakon, D. Barnes, R. Nebel, S. Kruger, S. Plimpton, A. Tarditi, M. Chu, the NIMROD Team, Nonlinear Magnetohydrodynamics with High-order Finite Elements, J. Comp. Phys. 195 (2004) 355.

[37] E. D. Held, J. D. Callen, C. C. Hegna, C. R. Sovinec, Conductive electron heat flow along magnetic field lines, Phys. Plasmas 8 (2001) 1171–1179.

[38] E. D. Held, J. D. Callen, C. C. Hegna, Conductive electron heat flow along an inhomogeneous magnetic field, Phys. Plasmas 10 (2003) 3933–3938.

[39] E. D. Held, Unified form for parallel ion viscous stress in magnetized plasmas, Phys. Plasmas 10 (2003) 4708–4715.

[40] E. D. Held, J. D. Callen, C. C. Hegna, C. R. Sovinec, T. A. Gianakon, S. E. Kruger, Nonlocal closures for plasma fluid simulations, Phys. Plasmas 11 (2004) 2419–2426.

[41] V. A. Izzo, D. G. Whyte, R. S. Granetz, P. B. Parks, E. M. Hollmann, L. L. Lao, J. C. Wesley, Magnetohydrodynamic simulations of massive gas injection into Alcator C-Mod and DIII-D plasmas, Phys. Plasmas 15 (2008) 056109.

[42] C. C. Kim, the NIMROD team, Impact of velocity space distribution on hybrid kinetic-magnetohydrodynamic simulation of the (1,1) mode, Phys. Plasmas 15 (2008) 072507.

[43] J.-Y. Ji, E. D. Held, C. R. Sovinec, Moment approach to deriving parallel heat flow for general collisionality, Phys. Plasmas 16 (2009) 022312.

[44] E. D. Held, S. E. Kruger, J.-Y. Ji, E. A. Belli, B. C. Lyons, Verification of continuum drift kinetic equation solvers in NIMROD, Phys. Plasmas 22 (2015) 032511.

[45] J. R. Jepson, C. C. Hegna, E. D. Held, J. A. Spencer, B. C. Lyons, Benchmarking NIMROD continuum kinetic formulations through the steady-state poloidal flow, Phys. Plasmas 28 (2021) 082503.

[46] J. A. Spencer, B. Adair, E. D. Held, J.-Y. Ji, J. R. Jepson, Accurate numerical, integral methods for computing drift-kinetic Trubnikov-Rosenbluth potentials, J. Comp. Phys. 450 (2022) 110862.

[47] S. Taheri, J. R. King, U. Shumlak, Time-discretization of a plasma-neutral MHD model with a semi-implicit leapfrog algorithm, Computer Physics Communications 274 (2022) 108288.

[48] M. T. Beidler, J. D. Callen, C. C. Hegna, C. R. Sovinec, Mode penetration induced by transient magnetic perturbations, Phys. Plasmas 25 (2018) 082507.

[49] E. C. Howell, J. R. King, S. E. Kruger, J. D. Callen, R. J. La Haye, R. S. Wilcox, Growing neoclassical tearing modes seeded via transient-induced-multimode interactions, Phys. Plasmas 29 (2022). 022507.

[50] S. Chapman, T. G. Cowling, The Mathematical Theory of Non-uniform Gases, Cambridge U. P., Cambridge, England, 1970.

[51] C. Liu, S. C. Jardin, H. Qin, J. Xiao, N. M. Ferraro, J. Breslau, Hybrid simulation of energetic particles interacting with magnetohydrodynamics using a slow manifold algorithm and GPU acceleration, Computer Physics Communications 275 (2022) 108313.

[52] N. Ferraro, S. Jardin, Calculations of two-fluid magnetohydrodynamic axisymmetric steady-states, J. Comp. Phys. 228 (2009) 7742–7770.

[53] M. Bennoune, M. Lemou, L. Mieussens, Uniformly stable numerical schemes for the Boltzmann equation preserving the compressible Navier–Stokes asymptotics, J Comp. Phys. 227 (2008) 3781–3803.

[54] A. Crestetto, N. Crouseilles, M. Lemou, Kinetic/fluid micro-macro numerical schemes for Vlasov-Poisson-BGK equation using particles, Kinetic and Related Models 5 (2012) 787–816.

[55] A. Crestetto, C. Klingenberg, M. Pirner, Kinetic/Fluid Micro-Macro Numerical Scheme for a Two Component Gas Mixture, Multiscale Modeling & Simulation 18 (2020) 970–998.

[56] B. C. Lyons, S. C. Jardin, J. J. Ramos, Steady-state benchmarks of DK4D: A time-dependent, axisymmetric drift-kinetic equation solver, Phys. Plasmas 22 (2015) 056103.

[57] R. L. Haye, C. Chrystal, E. Strait, J. Callen, C. Hegna, E. Howell, M. Okabayashi, R. Wilcox, Disruptive neoclassical tearing mode seeding in DIII-D with implications for ITER, Nuclear Fusion 62 (2022) 056017.

[58] Dense plasma theory, URL: https://lanl.gov/projects/dense-plasma-theory/research/particle-transport/kinetic-theory.php, accessed: 02-19-2024.

[59] T. D. Arber, K. Bennett, C. S. Brady, A. Lawrence-Douglas, M. G. Ramsay, N. J. Sircombe, P. Gillies, R. G. Evans, H. Schmitz, A. R. Bell, C. P. Ridgers, Contemporary particle-in-cell approach to laser-plasma modelling, Plasma Physics and Controlled Fusion 57 (2015) 113001.

[60] J. D. Callen, Plasma Kinetic Theory, 2015.

[61] J. J. Ramos, Finite-Larmor-radius kinetic theory of a magnetized plasma in the macroscopic flow reference frame, Phys. Plasmas 15 (2008) 082106.

[62] J. J. Ramos, Fluid and drift-kinetic description of a magnetized plasma with low collisionality and slow dynamics orderings. II. Ion theory, Phys. Plasmas 18 (2011) 102506.

[63] G. F. Chew, M. L. Goldberger, F. E. Low, S. Chandrasekhar, The Boltzmann equation and the one-fluid hydromagnetic equations in the absence of particle collisions, Proceedings of the Royal Society of London. Series A. Mathematical and Physical Sciences 236 (1956) 112–118.

[64] M. Landreman, D. R. Ernst, New velocity-space discretization for continuum kinetic calculations and Fokker–Planck collisions, J. Comp. Phys. 243 (2013) 130–150.

[65] J. Candy, R. Waltz, An eulerian gyrokinetic-maxwell solver, J. Comp. Phys. 186 (2003) 545 – 581.

[66] M. Barnes, W. Dorland, T. Tatsuno, Resolving velocity space dynamics in continuum gyrokinetics, Phys. Plasmas 17 (2010) 032106.

[67] R. W. Harvey, M. G. McCoy, The CQL3D fokker–planck code, in: Proc. IAEA TCM on Advances in Sim. and Modeling of Thermonuclear Plasmas, Montreal, Canada, 1992, pp. 489–526. Available through USDOC/NTIS No. DE93002962; see also `http://compxco.com/cql3d_manual.pdf`.

[68] C. Sovinec, J. King, Analysis of a mixed semi-implicit/implicit algorithm for low-frequency two-fluid plasma modeling, J. Comp. Phys. 229 (2010) 5803–5819.

[69] R. Morris, PhD Dissertation (1995).

[70] J. DeLucia, S. Jardin, A. Todd, An iterative metric method for solving the inverse tokamak equilibrium problem, J. Comp. Phys. 37 (1980) 183–204.

[71] E. A. Belli, J. Candy, Kinetic calculation of neoclassical transport including self-consistent electron and impurity dynamics, Plasma Physics and Controlled Fusion 50 (2008) 095010.

[72] L. Landau, 61 - ON THE VIBRATIONS OF THE ELECTRONIC PLASMA, in: D. TER HAAR (Ed.), Collected Papers of L.D. Landau, Pergamon, 1965, pp. 445–460.

[73] S. Hirshman, The ambipolarity paradox in toroidal diffusion, revisited, Nuclear Fusion 18 (1978) 917.

[74] J. D. Callen, Viscous Forces Due To Collisional Parallel Stresses For Extended MHD Codes, University of Wisconsin - Madison CPTC Report No. 09-6R (2010).

[75] J. A. Spencer, E. D. Held, J. R. Jepson, to be submitted (2024).

[76] J. D. Callen, A. J. Cole, C. C. Hegna, Toroidal flow and radial particle flux in tokamak plasmas, Phys. Plasmas 16 (2009) 082504.

[77] F. F. Chen, Introduction to plasma physics and controlled fusion; 3rd ed., Springer, 2015.